Design of Functionalized Cellulose Nanocrystals for Personal Care Applications

by

Fatima Awan

A thesis
presented to the University of Waterloo
in fulfillment of the
thesis requirement for the degree of
Master of Applied Science
in
Chemical Engineering

Waterloo, Ontario, Canada 2017

© Fatima Awan 2017

AUTHOR'S DECLARATION

I hereby declare that I am the sole author of this thesis. This is a true copy of the thesis, including any required final revisions, as accepted by my examiners.

I understand that my thesis may be made electronically available to the public.

Abstract

Derived from the depths of rich, green Canadian forests; the discovery of cellulose nanocrystals (CNCs) has pushed the research and industrial community to find strategic alternatives to replace existing non-renewable building blocks. With the commissioning of world's largest CNC demonstration plant in Quebec, Canada, the utilization of cellulose nanocrystals is feasible, and has opened a myriad of applications in recent years, such as energy, sensors, water treatment, biometrics, photonics etc.

This dissertation describes the modification of fundamentally inactive CNCs, and converting them into colloidally-active cosmetic systems. In the first approach, the high surface area, and equatorial -OH groups of CNCs were utilized for the nucleation of polyhydroxylated C_{60} fullerene, as a new antioxidant. The reaction kinetics were quantified and fitted to a pseudo first-order model, and a 2–stage biomolecular reaction mechanism was proposed. This work directly addresses the issue of insolubility that has previously hindered the biological application of the carbon nanocage (C_{60}/C_{70}), and has direct implications for understanding the underlying mechanism of the reaction-kinetics.

At the nanoscale, the surface properties become more dominant than in the bulk-phase due to the relatively higher proportion of atoms at the particle surface. Here, in the second approach a nitrogen-rich porous CNC template enabled the confined growth of semiconductor ZnO, providing a proportionally higher curvature to enhance the active catalytic sites on the metal oxide. The hybrid system was evaluated for in-vitro sun protection factor (SPF) and photocatalytic activity under UV and solar stimulation, and interpreted through the solid-band theory. The reaction kinetics were fit to the Langmuir-Hinshelwood model displaying a 4-fold increase in the photocatalytic activity of the hybrid nanostructure, compared to pure ZnO. Our work suggests that an increase in photocatalysis can be engineered without the introduction of structural defects or tailoring the band gap of ZnO.

To the best of our knowledge, this thesis represents one of the first pioneering studies that reports on the development of optimized personal care systems derived from *f*CNCs. Our studies showed that the translation of this renewable nanomaterial into scalable cosmetic systems is suggestively viable.

Acknowledgements

I would like to express my deep and sincere gratitude to my research supervisor, Professor Michael Tam, for his remarkable guidance, patience and support throughout the course of my graduate research in the Laboratory of Functional Colloids and Sustainable Nanomaterials. I am very grateful to have had the opportunity to mark this exciting and uncharted research area, and be a part of such an incredible journey.

I would also like to acknowledge my committee members Dr. Michael Pope and Dr. Evelyn Yim, for their insightful comments and constructive criticism. Their perceptive feedback helped strengthen the quality of this thesis.

I would like to extend my gratitude to Dr. Juewen Liu for granting me access to his equipment to enable better characterization of my work. Zeta potential analysis, and some of the UV-Vis measurements were performed in his lab using the Malvern Nano ZS Zetasizer DLS System and HP/Agilent UV-Vis Spectrophotometer.

Special thanks to all of my wonderful colleagues who made the time here so enjoyable, and effusively memorable!

To my parents, my heartfelt gratitude and appreciation for their unconditional love, wisdom and strength.

Table of Contents

List of Figures

List of Tables

Chapter 1

Introduction

1.1 Background overview and research motivation

Sustainability is critical for the maintenance of the earth, and together with nanotechnology, it could provide solutions to many of the challenges that we face as a result of globalization. The increasing awareness and discussion on this subject provides impending evidence for finding solutions that are sustainable and innovative, and ones that meet the needs of the present, without compromising the resources of the future. With this single-minded motivation, the objective of this research is two-fold (i) provide solutions to new and upcoming challenges (ii) produce functional nanomaterials that create a platform for advanced technologies promoting sustainability.

The personal care industry is a lucrative field where nanotechnology plays an important role in many of the new innovations. The personal care products (PCP) in Canada alone is a $9.14 billion industry, often described as fast-paced and where product innovation is the key to success (Bowman & Calster 2008). There is an ever-growing demand for products that possess enhanced aesthetic and functional qualities. In the recent decade, there has been a dramatic shift and focus on antiaging technologies, where, skin care products, such as lotion and emollients are necessities, while others are discretionary (Bowman & Calster 2008; Kumar et al. 2006). As a result of these demands, there is growing interest by the industry to implement nanotechnologies within personal care formulations, and an assortment of engineered nanomaterials ranging from C_{60} fullerenes, quantum dots, liposomes, metal oxides, polymers and nanospheres have entered the markets (Earth 2006). But with the introduction of nanomaterials in the market, there is also an on-going debate over the potential risks associated with these compounds, and the key deciding factor is product efficacy. Due to their nano-scale dimensions, some of these materials still pose a limit in terms of transparency and water solubility (Bowman & Calster 2008). For example, current zinc oxide and titanium dioxide commercially used in sunscreens offer broad spectrum UV protection, however, due to the high surface energy, these metal oxides require coatings with inert toxic chemicals that can compromise, both, the aesthetic and functional appeal. Such materials also precipitate out in aqueous solutions as a result of increased agglomeration, and to address these challenges, expensive surfactants and tedious polymeric coatings have been introduced into the process to stabilize the nanoparticles. Thus, stability becomes an important issue since with increased stacking and agglomeration, there are less active surface sites available, which has a negative impact on the performance and the overall efficiency. Much of this phenomena will be specifically discussed in the experimental studies described in this thesis.

New and safe strategies to engineer nano-materials, inspired by nature and appropriately optimized can offer a range of innovative development, and improvement to the existing systems. An inspiration derived from nature itself, a new class of nanomaterials known as cellulose nanocrystals (CNCs) have generated interest in both industry and academia. The 200 x 50 nm crystalline domains derived from pulp fiber possess mechanical strength comparable to Kevlar, aspect ratio and surface area, low weight, surface functional groups, and pronounced stable dispersions in water (Habibi et al. 2010; Peng et al. 2011). Most importantly, this renewable biomass offers physiognomies that compensate and synergize the negative properties that hinder the performance of existing personal care systems.

With Canada leading the world’s largest production scale of these nanocrystalline rods, there is an opportunity to shape the way in which nanotechnology develops in sectors such as waste water treatment, energy, biosensors, food, and even agriculture (Habibi et al. 2010; Peng et al. 2011; Zoppe et al. 2009; Kalia et al. 2011). Most prominent research involving CNC has highlighted its capacity as a reinforcing agent in polymeric matrix, dye adsorbent, emulsion stabilizer at the oil-water interface, viscosity modifier, bio-imaging probe, insulating template for conductive ink and other nascent fields. And because these biocompatible nanorods are new and pervasive, there is significant opportunity for other important discoveries. Opening up the list of potential applications, is the autonomous developmental progression of well-designed CNC in personal care formulations. So far, very limited research has been devoted to this field, suggesting the enormous potentials of this nature-inspired nanocrystal for use as a surface active, and optimally functional element in personal care. As an enabling technology, the synthesized CNC nanocomposites developed and outlined in this thesis are a pragmatic tool to understand the mechanisms at the molecular level, and to demonstrate the capacity of the modified CNCs as antioxidants, UV blockers, and surface-active photocatalytic aqueous compositions.

1.2 Research scope and methodology

The research outlined in this thesis focuses on the development of functional CNCs for cosmetic and personal care applications. The nano-fabricated CNC designs were established with the concept of green nanotechnology, amenable to sustainability and a systematic approach that offers a comprehensive solution to challenges facing the personal care industry. Each of the systems were built with an environmentally consciousness and simple green chemistry, with nature as the source of inspiration. A summary of the methodology, approach and the framework for the experimental design is presented below:

I. *Fabrication of polyhydroxylated C_{60} fullerene on the surface of CNC rods*

Highly active fullerol $C_{60}(OH)_{30}$ nanoparticles were synthesized through an organic-aqueous phase transfer, and subjected to nucleation on the excited surface of pristine CNC. TGA analysis revealed a grafting degree of 20% of fullerols and the antioxidant activity was measured via the DPPH radical assay. At the molecular level, a proposed mechanism on the interaction of the radicals with the CNC-based antioxidant system was described by a two-stage bio-molecular reaction kinetics.

II. *Optimization and growth of semiconductor ZnO on polymerized MFCNC composites*

A nitrogen rich precursor of melamine-formaldehyde resin (MF) was first polymerized and condensed on the surface of CNC. The mesoporous N-rich matrix provided for a chelating template for the confined growth of ZnO NPs. With the high surface energy of

ZnO NPs controlled, a systematic study describing the effect of hydroxide ratio on the Sun Protection Factor (SPF) revealed an optimal ratio of $1[Zn^{2+}]:3[OH^{-}]$ for the highest SPF value. The optimized system was evaluated for the photocatalytic performance that was elucidated through the rationales of solid-band gap theory.

1.3 Thesis outline

This thesis consists of six chapters. Chapter 1 provides an overview of the research, scope and motivation. Chapter 2 summarizes the literature that describes the fundamentals behind the design of the research. Chapter 3 discusses the development of water-soluble C60 system conjugated to the surface of CNC, for antioxidant capacities, along with a detailed characterization of the system. Chapter 4 describes the principles of fabrication of CNC with surface active ZnO nanoparticles, and the system's two-dimensional functionality. Chapter 5 addresses the significance and conclusions of the development of functional CNC in personal care systems, and Chapter 6 highlights the recommendations and future directions for the work presented in this thesis. Following chapter 6 is an alphabetical list of references used throughout the document.

Chapter 2

Literature Review

2.1 First principles of C60 fullerene and its derivatives

First discovered in the veil of cosmic dust in 1985 by Richard Smalley, Harry Kroto and Robert Curl at Rice University and University of Sussex, C_{60} fullerene has since found applications in optoelectronics, antioxidants, fluorescence, and gas permeability (Wang et al. 1999). The inherent features of the geodesic domes of this carbon allotrope offers unique characteristics. Found in rocks dating Precambrian era, the 0.7 ± 0.007nm (Djordjevic & Bogdanovic 2008) C_{60} cage is said to possibly have provided for the early nucleated growth of life on earth. With the exciting breakthrough of this nanomaterial, there is no doubt fullerenes have a landmark of their own in nanotechnology and engineering. However, since its discovery, many of the practical applications have been largely hindered, especially in biochemistry and medicine, due to the rigid hydrophobic core arising from π-π stacking between the covalently bonded carbon double bonds (Deguchi et al. 2001).

The black crystals of C_{60} can easily dissolve in aromatic hydrocarbon solvents, such as toluene and carbon disulfide, revealing a beautiful purple colour as a result of electron delocalization (Djordjevic & Bogdanovic 2008). But the pristine structure of this carbon allotrope proves to be extremely insoluble in water. The relation of the electrokinetic properties of fullerene, and the inherent stability is largely dependent on the valence and concentration of the electrolytes in solution (Chen & Elimelech 2009). With the pioneering work reported in Nature in early 1990s, Atwood et al. attempted to solubilize C60 through complexation in toluene using para-Bu'-calix[8]arene which forms a 'ball and socket' encapsulation around the fullerene molecule in the cavity of the macrocycle (Figure 2.1) (Atwood et al. 1994). The ordered cyclic arrays with phenolic hydroxyl groups are bonded through hydrogen bonds and directed towards the center of the ring. The array structure allows for flexibility and accommodation of the fullerene and facilitates the interaction as a ‘ball and socket’ nanostructure (Atwood et al. 1994).

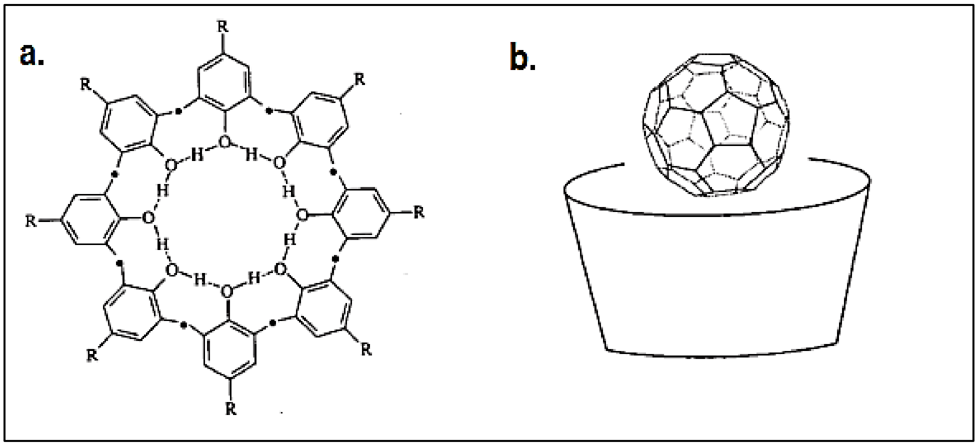

Figure 2.1: a. Molecular structure of *p*-R-calix[8]arene in tolouene solution (R = Bu’). b. ‘Ball and socket’ nanostructure of fullerene inside the cavity of the calixarene (Atwood et al. 1994).

Other techniques involving the development of water-soluble complexes of fullerenes since the macrocycle complexations include covalent functionalization, conjugation of amphiphilic polymers and host guest interactions, namely with cyclodextrins. The fundamental logic of such host-guest systems is the occupation of the fullerene molecule inside the hydrophobic cavity of cyclodextrins; the cyclic oligosaccharides composed of ά(1,4) glucosyl residues (Andersson et al. 1992). The formation of C_{60}-γ-cyclodextrin complex first reported by Yoshida et al. showed an existence of charge transfer between C_{60} and γ-cyclodextrin, with ether oxygen of tetrahydrofuran (THF) and alcoholic oxygen of water (H_2O) being the electron donors, and high electron affinity (2.7 eV) of fullerene to accept these electrons (Deguchi et al. 2001). Another such example is the encapsulation of C_{60} in β-cyclodextrin through the aqueous and organic phase transfer to encapsulate the cohesive C_{60} molecules inside the hydrophobic cavity as shown in Figure 2.2. The β-CD system was also shown to have superior radical scavenging capacity as measured and elucidated by DPPH assay, and resulted in a patent disclosure for the technology (Yao & Tam 2014).

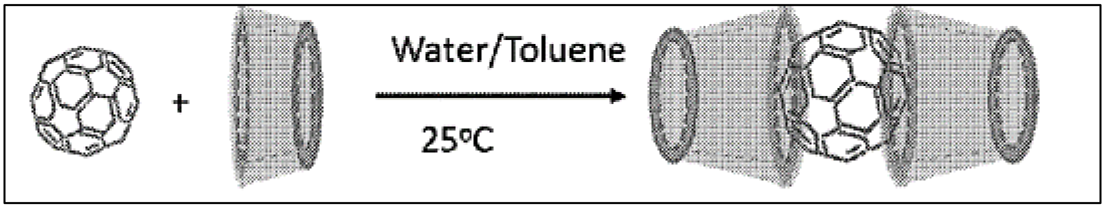

Figure 2.2: Illustration of the mechanism of synthesis of β-CD/C60 complex through aqueous-organic bilayer transfer (Yao & Tam 2014).

A large amount of effort has also been devoted to exploit the development of “polyfullerenes”, with grafting of polymeric chains through photopolymerization, pressure induced polymerization, charge-transfer polymerization mediated by metals, or electron beam-induced polymerization for the construction of fullerene based architectures for application in gas permeability, fluorescence, and superconductivity (Giacalone & Martin 2006). A summary of some of the representation of the architectural structures based on fullerene-polymeric systems is presented in Figure 2.3b. Typical polymerization process involves electrophilic/nucleophilic substitution, or [2+2] cycloaddition reaction pathway between two C-C double bonds of adjacent C_{60} molecules, where a new cyclobutane ring forms to connect the fullerene cages, as shown in Figure 2.3a (Giacalone & Martin 2006; Bosi et al. 2003). Investigations of photopolymerized C_{60} molecules and its electronic and bulk properties showed a dramatic shift in the electronic and non-linear absorption properties compared to pristine fullerene. C_{60} cages grafted with polymer solution resulted in a much weaker fluorescence, scarcely detectable triplet-state absorption, and marginal optical limiting response (Giacalone & Martin 2006). Fabrication of membranes for gas separation, blending and miscibility studies with styrenic polymers showed remarkable effort for the grafting of C_{60} onto saturated ethylene-propylene polymer, poly(2,6-dimethyl-1,4-phen-ylenoxide) (PPO). The synthesis involves partial bromination of methyl groups and substitution of azido groups, where controlling the initial bromine amount could fine-tune the polymer grafting on the C_{60} cage. Gas permeability experiments carried out on the C_{60}-grafted PPO system and pure PPO samples shows that such a conjugated complex could significantly increase the permeability rate, in some cases by up to 80% (Giacalone & Martin 2006).

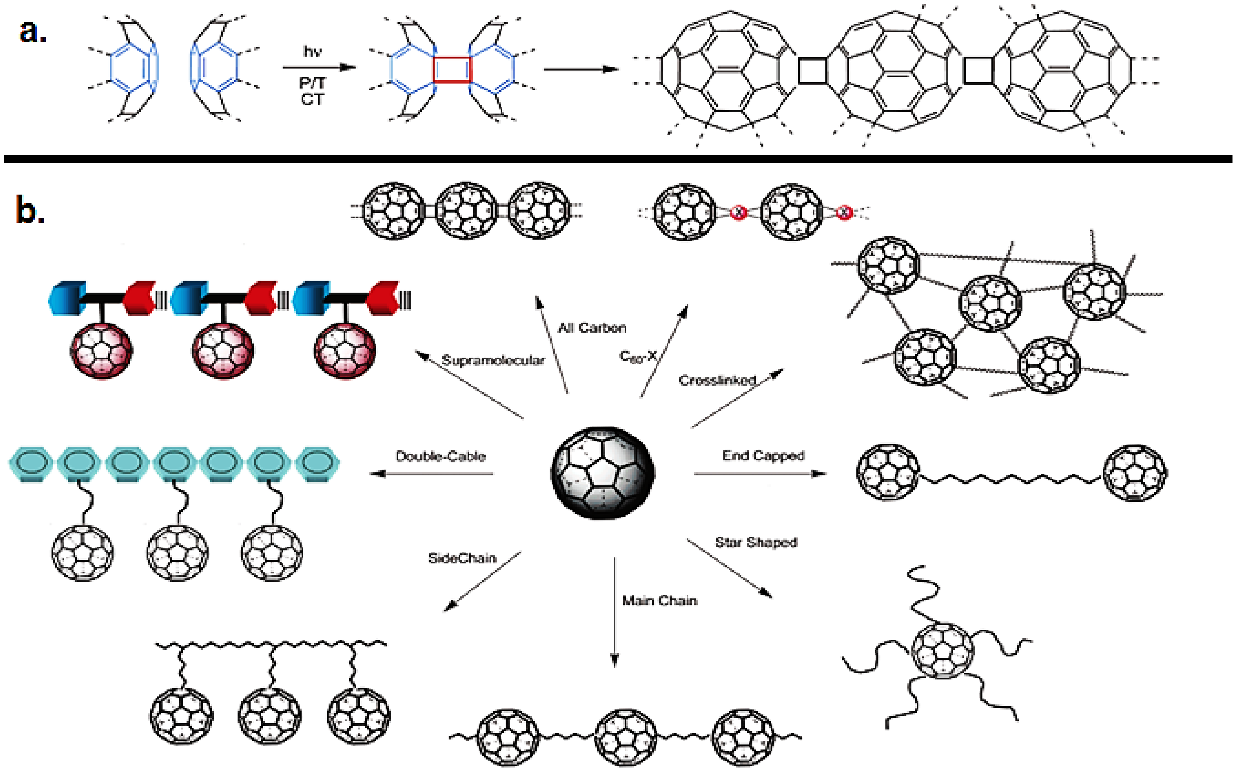

Figure 2.3: a. 2+2 cycloaddition reaction mechanism of C60 fullerene. b. Polymer grafted-fullerene systems comprising various architectural representations (Giacalone & Martin 2006).

Another class of ellipsoidal carbon allotrope, known as carbon nanotube (CNT) has attracted much attention in recent years due to the remarkable conductivity and electronic properties. Bourlinos *et al*. recently reported the decoration of the nanotube walls with water-soluble derivative of C_{60}, known as fullerols. This class of polyhydroxylated fullerenes operate on the principle of surface modification of the cage with –OH groups, making them effectively soluble in water. Much of the discussions on such surface modifications of C_{60} spheres will also be discussed in chapter 3. Here the group reported the oxidation of CNTs and subsequent wet-impregnation of fullerol on the multi-walled tubes and solid-state heating to promote interfacial bonding, as shown in Figure 2.4a (Bourlinos et al. 2012). The well dispersed aqueous solution arising from polyanion fullerol clusters with an average height ranging from 0.8-1.1 nm (Figure 2.4b) attached to the MWNT provide static repulsions in solutions, making them an attractive filler for medical, or nanopharmaceutic applications(Bourlinos et al. 2012).

The summary of the principles of fullerene, their derivative and applications have been presented in this section. Significant efforts have produced polymer based, covalent functionalized, agent coupled or host-guest complex solutions of C60 fullerene for characterized performances in electrical, fluorescence, gas chromatography and presupposed medical endeavors. A combination of the research should provide the basis for the development of enhanced and elementally novel systems.

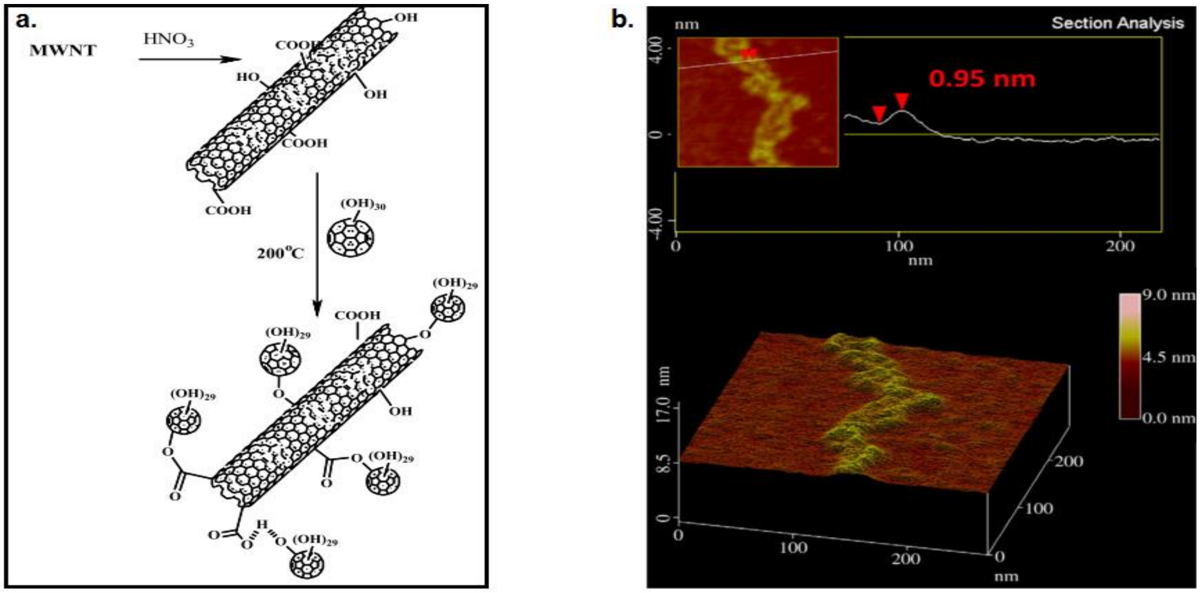

Figure 2.4: a. Schematic representation of the wet-impregnation of oxidized CNT (multi-wall) with fullerol nanoparticles at 200 ˚C. b. AFM images illustrating cross sectional analysis of the CNT-fullerol clusters deposited on Si-wafer (Bourlinos et al. 2012).

2.2 Advances and processing of semiconductor metal oxides

Semiconductors with wide-band-gaps have been studied for many decades due to their unique electronic and optical properties. In recent years, the idea for technological applications was realized and an upsurge of research activity in academia has been witnessed. Some metal oxides, and compounds such as GaN or ZnSe with short wavelength of band-to-band transitions allow the emission in the UV or visible region composed of green, blue spectrum. Fabrication of ZnSe materials with dopants (p-type) have led to the application of short-wavelength light emitting devises for colour display or optical storage (Dietl 2010). For GaN, new refined growth procedures for producing doped materials have resulted in blue-light emitting laser diodes, and the advances in growth techniques for bulk as well as epitaxial material have made the commercial production of high-temperature and high-frequency optoelectronic devices possible. With the favorable mechanical and thermal properties, the discoveries reflect an exciting progress made in the field of semiconductors.

Shifting the focus to metal oxides reveals major players in this field; specifically zinc oxide (ZnO) and titanium dioxide (TiO_2) with potentials as catalyst, piezoelectronic, photoluminescence and other applications (Kołodziejczak-Radzimska & Jesionowski 2014). Their low dimensional nanostructures offer the possibility of further optimization, fabrication, and improving lasing conditions due to quantum confinement effects (Yin et al. 2004). A recent report in 2012 by Etacheri et al. discussed the incorporation and substitution of Zn^{2+} by Mg^{2+} in the wurtzite structure of ZnO lattice. The doping effect shown in Figure 2.5, was synthesized through an oxalate co-precipitation method which was shown to improve the Zn-O bond in Mg-Doped samples. A blue shift in the photoluminescence intensity revealed a band gap widening, suggesting an efficient electron–hole separation. In addition, improved textural properties as a result of calcination at high temperatures increased the crystallinity of the doped crystal leading to enhanced sunlight-driven photocatalytic activities for self-cleaning devices (Etacheri et al. 2012).

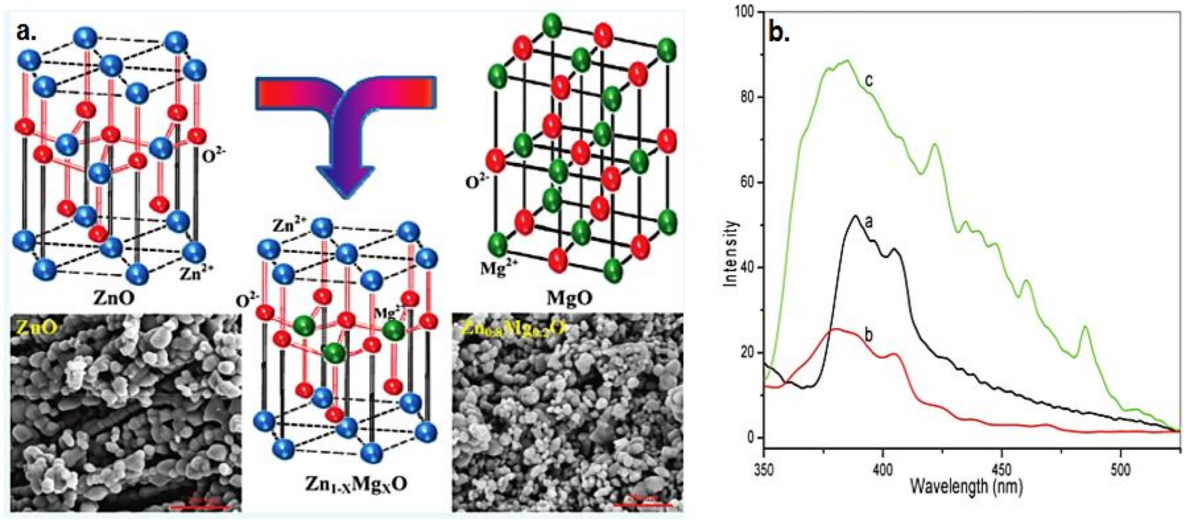

Figure 2.5: a. Configurative model and SEM images of Mg doped ZnO lattice structures and substitution of Zn^{2+} by Mg^{2+}. b. Photoluminescence spectra exhibiting blue shift in ZMO samples; a. ZnO, b. 0.10-MgZnO, c. 0.20-MgZnO calcined at 600 ˚C (Etacheri et al. 2012).

Actual growth and synthesis of metal oxides can occur through a number of ways including, vapor deposition, mechanochemical, chemical, sol-gel and hydrothermal mediated synthesis that enables the production of particles of different size and shapes (Kołodziejczak-

Radzimska & Jesionowski 2014). A summary of some of the synthesis conditions for growing ZnO particles through the wide-used sol-gel method is shown in Table 2.1. Normally a precursor solutions such as zinc acetate dehydrate or zinc chloride are added to a hydrolyzing agent, such as tetramethylammonium hydroxide (TMAH) and washed with organic solvents resulting in an increased solubility of metal oxides in higher hydrocarbon solvents(Becheri et al. 2008; Joo et al. 2011; Kołodziejczak-Radzimska & Jesionowski 2014). High pH bases are usually employed during the synthesis, so that the metal oxides are not contaminated with the cation from the base, which may have an effect on the ohmic conductance of the oxide material. TEM analysis indicated the growth of ZnO particles with sizes of the order of 20–50 nm (Kołodziejczak-Radzimska & Jesionowski 2014).

Table 2.1: Summary of the method of synthesis and conditions applied for the growth of ZnO NPs via sol-gel route (Kołodziejczak-Radzimska & Jesionowski 2014).

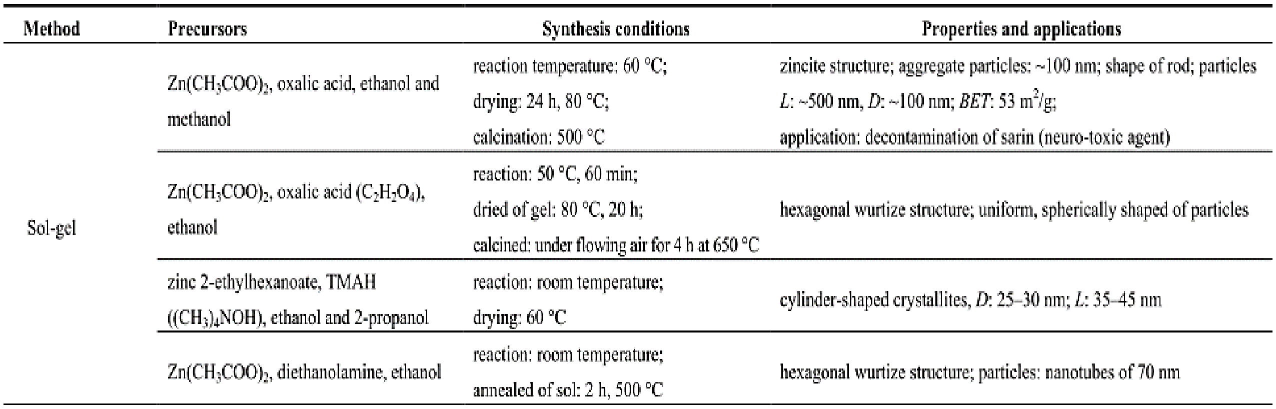

Method	Precursors	Synthesis conditions	Properties and applications
Sol-gel	$Zn(CH_3COO)_2$, oxalic acid, ethanol and methanol	reaction temperature: 60 °C; drying: 24 h, 80 °C; calcination: 500 °C	zincite structure; aggregate particles: ~100 nm; shape of rod; particles *L*: ~500 nm, *D*: ~100 nm; *BET*: 53 m^2/g; application: decontamination of sarin (neuro-toxic agent)
	$Zn(CH_3COO)_2$, oxalic acid ($C_2H_2O_4$), ethanol	reaction: 50 °C, 60 min; dried of gel: 80 °C, 20 h; calcined: under flowing air for 4 h at 650 °C	hexagonal wurtize structure; uniform, spherically shaped of particles
	zinc 2-ethylhexanoate, TMAH ($(CH_3)_4NOH$), ethanol and 2-propanol	reaction: room temperature; drying: 60 °C	cylinder-shaped crystallites, *D*: 25–30 nm; *L*: 35–45 nm
	$Zn(CH_3COO)_2$, diethanolamine, ethanol	reaction: room temperature; annealed of sol: 2 h, 500 °C	hexagonal wurtize structure; particles: nanotubes of 70 nm

For matters of quantification, it is important to characterize the physical, chemical as well as quantitative aspects of the system. An approach to determine the size of nanoparticles i.e. quantum dots can be derived mathematically based on modeling the excited electronic states of semiconductor crystallites (Brus 1984). For sufficiently small particles and metal oxides with electronic properties largely different than the bulk, a sophisticated approach for calculating the size of the particle can be applied through the correlation of absorption data of the colloidal solution and approximation of band-gap (eV) with the effective mass model (Brus 1984) equation (2.1):

$$E_g = E_g^* \left(\frac{h^2\pi^2}{2r^2}\left(\frac{1}{m_e me} + \frac{1}{m_h mh}\right)\right) - \frac{1.8e^2}{4\pi\varepsilon\varepsilon_0 r} \tag{2.1}$$

where, E_g is the band gap of nanoparticles, E_g^* is the bulk band-gap energy, h is Planck's constant, r is the radius of the particle in nm, m_e is the mass of the electron, m_h = mass of hole, e is the elementary charge on the electron, $\mathcal{E}$ is relative permittivity and $\mathcal{E}_0$ is the permittivity of free space. As such based on the optical and photoluminescence (PL) data of metal oxide semiconductors, band-gap (eV) values can be approximated and the size of the particle in nm can be determined (Brus 1984; Goh et al. 2014; Singla et al. 2009)

A class of colloidal semiconductors are quantum dots (QD) with luminescent properties that have received much attention in recent years as QD-conjugates in biological application, biomolecular imaging probes and energy harvesting mechanisms (Hildebrandt et al. 2016) . The original QD material prepared by CdS core-shell (Chen et al. 2016), or core-multishell configurations from binary, tertiary, or alloyed are presented in colloidal form as opposed to epitaxial QDs (Hildebrandt et al. 2016). Though silicon and germanium (group IV) nanocrystals display interesting quantum confinement effects and size-dependent emission properties, they are but difficult to control during synthesis. The ability of these QDs to engage in energy transfer or biosensing forms directly depend on several inter-related material properties including the type/quality of QD used, the photophysical properties, and most important the method employed to stabilize the colloidal QDs in aqueous solution (Hildebrandt et al. 2016). Several approaches summarized in Figure 2.6 show the methods of fabrication to render the QDs biocompatible that improves both the fluorescence and photochemical stability of QDs for practical use. Primary categorization of making hydrophobic semiconductor QDs stable in water include three different approaches: (i) ligand exchange, (ii) encapsulation and (iii) silica coating (Hildebrandt et al. 2016). Through the ligand exchange the original hydrophobic surface ligands on the QD surface are replaced with hydrophilic ligands, where colloidal stability of QDs coated with these ligands relies solely on deprotonation of the functional groups i.e, carboxyl groups. Another example are single thiol ligands modified with poly(ethylene glycol) (PEG) for hydrophilic modification of QDs (Figure 2.6 (ii)). Encapsulation is a method in which extraneous amphiphilic ligands are coated on the QDS via hydrophobic interactions. The hydrophobic chains of the amphiphilic ligands are interdigitated in the hydrophobic region, while the hydrophilic chains surrounded the QD peripheral surface for colloidal stability. Another approach is silica coating chemistry with the same function to render the surface of QD more hydrophilic through the chemical modification with thiol groups (Hildebrandt et al. 2016; Chen et al. 2016).

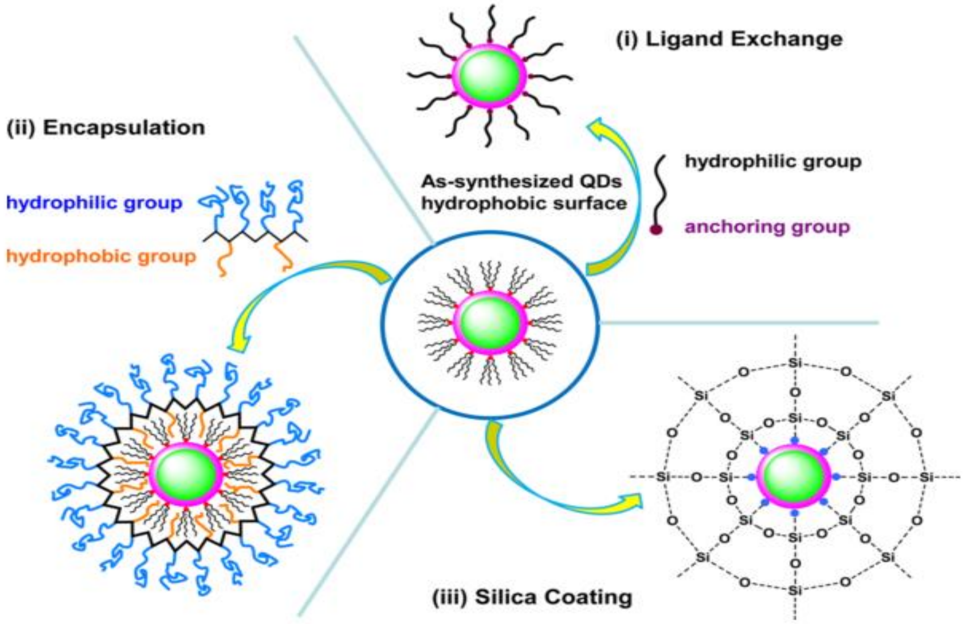

Figure 2.6: Schematic illustration of Quantum Dots (QD) stabilized in aqueous solutions by (i) ligand exchange, (ii) encapsulation, and (iii) silica coating chemistries (Hildebrandt et al. 2016).

Another investigation showed the ultrafast dynamics of charge carriers in type II ZnSe/CdS hetero-structures with barbell like configuration of ZnSe around the CdS nanorods, as illustrated in Figure 2.7a. The barbell structures were fabricated via colloidal routes where first CdS rods were grown via seeded-approach in hexane, followed by introduction of ZnS at the tips of the nanorods (Hewa-Kasakarage et al. 2010)**.** The results indicated an ulta fast transfer of excited electron of ZnSe tips into CdS domains (<0.35 ps). With variation of the e^-/h^+ dynamics, potential photocatalytic applications due to fast separation of carriers along the main axis of ZnSe/CdS barbells was demonstrated (Hewa-Kasakarage et al. 2010). For the control of renewable energy, advanced materials that are electrocatalytic are central in these applications. Li et al. reported on the development of MoS_2 nanoparticles reduced on graphene sheets (RGO) via selective solvothermal synthesis in suspended dimethysulfide (DMF) solution as shown in Figure 2.7b (Li et al. 2011). The resulting MoS_2/RGO hybrid possessed nanoscopic MoS_2 features exposed at the edges of stacked graphene, providing excellent electrical coupling to the underlying graphene sheets and the smallest slope of the Tafel plot ever reported for MoS_2 catalyst (Li et al. 2011). Leaching into this similar area, a study by Xiang et al. showed growth of TiO_2 nanocrystals in the presence of layered MoS_2/graphene hybrid as a high-performance photocatalyst for H_2 evolution of 165.3 μmol h^{-1} (Xiang et al. 2012). The composite was prepared without metal cocatalyst and a two-step hydrothermal process using sodium molybdate, thiourea, and graphene oxide as precursors of the MoS_2/graphene hybrid. A positive synergetic effect between the MoS_2 and graphene cocatalyst serve as an electron collector and a source of active adsorption sites, respectively(Xiang et al. 2012). The charge transfer in TiO_2/MG composites is shown in Figure 2.7c, where the enhanced electron transfer in the hybrid system under irradiation is presumably attributed to the transfer of photoexcited electrons from the conduction band(CB) of TiO_2 to the MoS_2 nanosheets and carbon atoms of graphene(Xiang et al. 2012)**.** A **s**ummary of the above mentioned systems is presented in Figure 2.7.

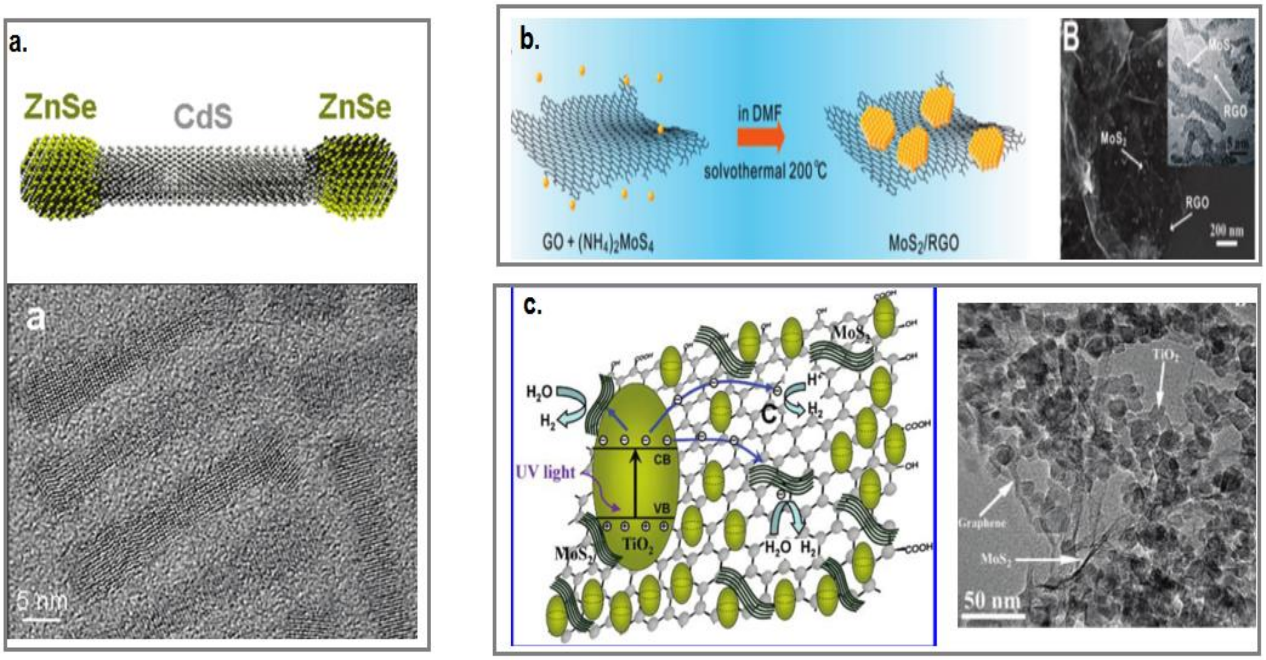

Figure 2.7: Summary of the report of various semiconductor nanosytstems. a. Structural analysis of type II heterostructured ZnSe/CdS nanobarbells (Hewa-Kasakarage et al. 2010). b. Growth of MoS_2 nanoparticles on graphene sheets for electrocatalytic activity in hydrogen evolution reaction (HER) (Li et al. 2011). c. TEM image and schematic illustration of TiO_2/MG composite (Xiang et al. 2012).

In conclusion, an-depth review of the academic progress and advances of semiconductors crystals is presented in this section with contributions from recognized work on different material systems, and the theoretical, experimental and application-oriented aspects of this topic.

2.3 Cellulose nanocrystals (CNCs)

With its existence dating the beginning of the Earth, cellulose is notably the most abundant terrestrial biomass available today. In 1883, Payen discovered this naturally occurring long-chain polymer composed of β-1,4 glucopyranose units in the plant cell wall (Payen 1883). Almost a century later, the birth of microfibrillated cellulose (MFC), the elongated bundles of polymer chains associated with hydrogen bonds, paved the way for the onset of a new nano wonder material, cellulose nanocrystals (CNC). These highly ordered crystalline domains of cellulose confer a very high elastic modulus, of 134 GPa (Tingaut et al. 2012). The simple process of obtaining CNCs involves an acid hydrolysis of the biomass using concentrated sulfuric acid H_2SO_4. The treatment removes the disordered amorphous or para-crystalline regions of cellulose and leaves crystalline regions intact (Tingaut et al. 2012; Peng et al. 2011). The result of this treatment produces rod-shaped cellulose nanofibers 5-20 nm wide and 200-400 nm long, bearing anionic sulfate ester groups on the surface, as shown in Figure 2.8. Actual geometric dimension varies depending on the source of cellulose. Here, the presence of the negatively charged SO_3^- groups maintains the suspended CNCs in polar solvents, such as water, due to electrostatic repulsions and stabilization effect (Habibi et al. 2010; Peng et al. 2011; Tingaut et al. 2012).

At the molecular level, cellulose nanocrystals possess a chain of 6-membered pyranose glucose units linked by hydrogen and –OH group (illustrated in Figure 2.8A). This linkage produces two disaccharide molecules called cellobiose, the repeating unit of cellulose (Kalia et al. 2011). The individual pyranose units are joined by single oxygen atoms through acetal linkages between C-1 of one pyranose ring and the C-4 of the next ring (Kalia et al. 2011). The spatial arrangement or stereochemistry of these acetal linkages is very important. At the periphery of the equatorial position in cellulose, the C-1 oxygen is on the opposite side of C-6 giving the β configuration with all the functional groups in equatorial positions. This configuration creates a linear molecular chain of cellulose making it a strong fiber-forming polymer (Kalia et al. 2011). The –OH groups at the equatorial position protrude laterally and are available for hydrogen bonding. Here the chains are arranged in a highly ordered fashion in the crystalline domains through interchain hydrogen bonding (Figure 2.8B), imparting good strength and rigidity (Kalia et al. 2011).

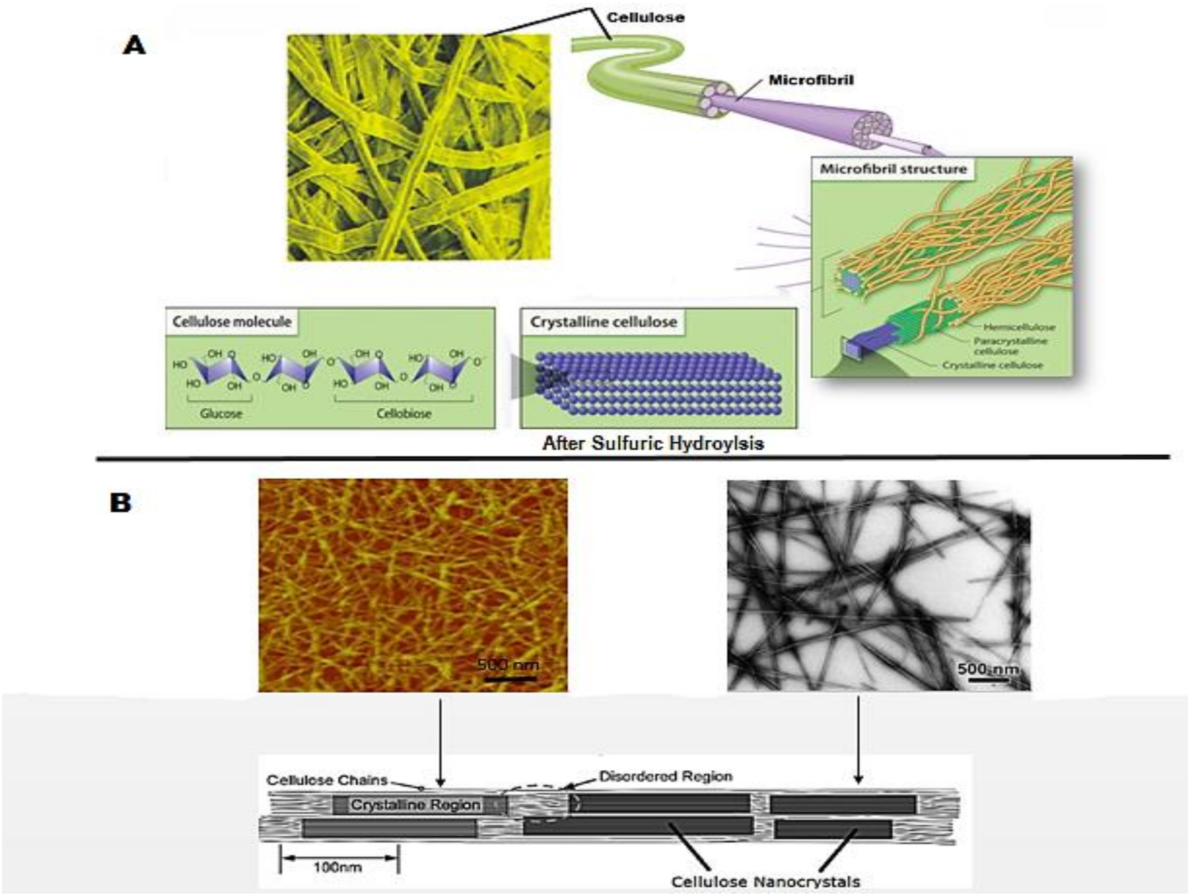

Figure 2.8: A. Process of extraction of CNC from wood pulp and the schematic representation of the multicomponent cellulose fiber and microfibril organization containing shorter organized crystalline phases with cellobiose repeating units (Adopted from Sam Adam-Day 2016; Siqueira et al. 2010). B. AFM and TEM images of CNC; and diagram indicative of the removal of amorphous regions after acid treatment (Peng et al. 2011; Moon et al. 2011).

At the molecular level, cellulose nanocrystals have a chain of 6-membered pyranose glucose units linked by hydrogen and –OH group (illustrated in figure 2.9A). This linkage produces two disaccharide molecules called cellobiose, the repeating unit of cellulose (Kalia et al. 2011). The individual pyranose units are joined by single oxygen atoms through acetal linkages between C-1 of one pyranose ring and the C-4 of the next ring (Kalia et al. 2011). The spatial arrangement or stereochemistries of these acetal linkages is very important. At the periphery of the equatorial position in cellulose, the C-1 oxygen is on the opposite side of C-6 giving the β configuration with all the functional groups in equatorial positions. This configuration creates a linear molecular chain of cellulose making it a strong fiber-forming polymer (Kalia et al. 2011). The –OH groups at the equatorial position protrude laterally and are available for hydrogen bonding. Here the chains are arranged in a highly ordered fashion in the crystalline domains through interchain hydrogen bonding (figure 2.9B), imparting good strength and rigidity (Kalia et al. 2011).

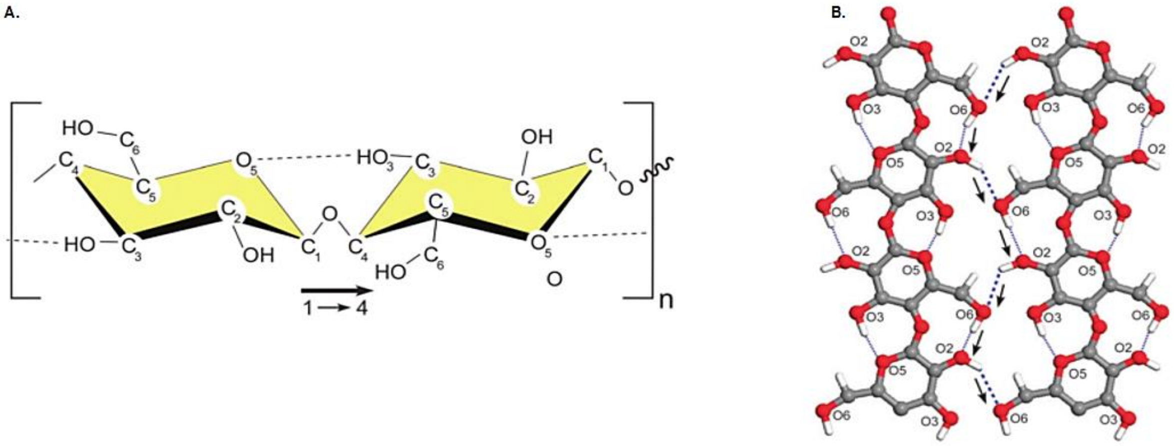

Figure 2.9: A. Repeating cellobiose units of cellulose with β-1,4 linkage at C1 and C4, and intrachain H-bond (represented by dotted line) (Moon et al. 2011). B. Schematic model of

hydrogen bonding network with intramolecular H-bond (thin lines) and intermolecular bonding (dotted lines) where attractive van der Waal forces act as a cohesion force between cellulose chains (Nishiyama et al. 2008).

2.3.1 Surface chemical modification of CNCs

For the design of optimally controlled and chemically modified CNCs, it is important to understand the surface chemistry. Cellulose reactions are predominately controlled by steric factors, and the inherent reactivity for surface modifications is due to the abundant hydroxyl groups; specifically -OH groups at carbon 2, 3, and 6 are the most active sites for chemical modifications and polymer grafting, with the –OH group at position 6 being the most reactive (Habibi et al. 2006; Kalia et al. 2011) (Figure 2.9). Though the cellulosic chains have many hydroxyl groups, it has been reported that the groups most external to the molecule chains are the most efficient in controlling the reaction conditions during functionalization (Habibi et al. 2006; Habibi et al. 2010). Chemical functionalization begins with the introduction of an initiator or monomer that is directed by surface -OH groups as the driving force for reaction conditions. With variation and control over time and temperature, a wide range of polymers have been grafted on the surface of CNC through the “grating to” or “grafting from” approach; a summary of such modifications is presented in Figure 2.10 (Lin, Huang, et al. 2012).

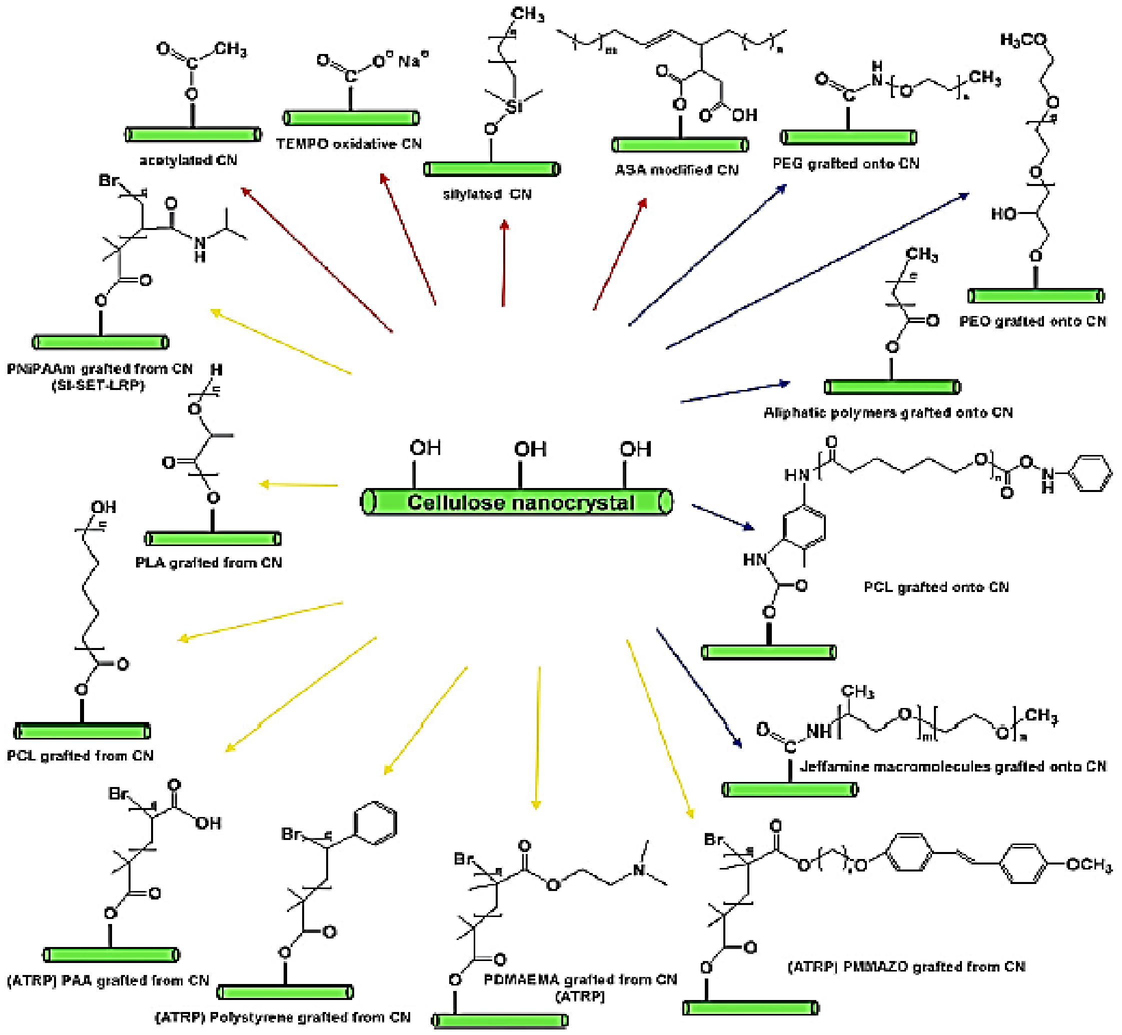

Figure 2.10: Summary of a range of chemically grafted polymers on the surface of CNC through ATRP mechanisms, grafting “to” and grafting “from” approach. (Lin, Huang, et al. 2012).

At the outset, CNCs act as the reinforcing matrix for the growth of polymer chains leading to the formation of macroscopic fibers, thereby, increasing the strength and stiffness of the materials (Peng et al. 2011; Liu et al. 2015; Lin, Huang, et al. 2012). These polymer grafted-CNCs systems found many interesting applications including bio-inspired mechanically adaptive nanomaterials, where the introduction of three-dimensional percolating networks of cellulose nanocrystals in polymeric matrices, such as ethyleneoxide–epichlorohydrin copolymer (EO–EPI), poly(vinyl acetate) (PVAc) and poly-(butylmethacrylate) (PBMA) demonstrate behaviour of biomimetic mechanically adaptive nanomaterials (Zhou et al. 2011). The tensile modulus of the first generation CNC/EO-EPI nanomaterial was shown to increase by two-orders of magnitude in the rubbery dry phase, and upon exposure to water, exhibited a 40-fold reversible reduction in the modulus (Zhou et al. 2011; Bica et al. 2001). Theoretical models predicting this behavior indicated the role of CNCs in controlling the selectivity and reversibility of the mechanically adaptive systems, with the formation and decoupling of a 3D network of individualized rigid nanocrystals. Through the formation of strong hydrogen bonds between the percolating CNCs, there is maximized stress transfer and induction that reinforces the nano- materials (Zhou et al. 2011). In contrast, external stimulus to the system such as changes in temperature or exposure to water, disrupts the association of the percolating rigid networks of CNC and weakens the hydrogen bonding interactions among nanocrystals (Zhou et al. 2011; Bica et al. 2001). The mechanically adaptive behaviour, and role of CNC as reinforcers in polymeric matrix suggests the influence it could have to compatibilize some of the common polymers used in personal care or product packaging, such as polylactic acid (PLA) or polycaprolactone (PCL), where Habibi *et al.* reported on the grafting of the polymer using stannous octoate ($SnOct_2$) to initiate the polymerization on the surface of CNC (Habibi et al. 2008).

The inherent rigidity and high aspect ratio of CNC impart another interesting characteristic together with the chiral nematic behavior where the rods align and self-assemble under certain concentration conditions (Shopsowitz et al. 2010; Kelly et al. 2014). Here the crystal suspensions control the helical twist along the main axis to organize the nanoparticles into a chiral nematic phase. These self-assembled CNCs display iridescent colours under certain wavelengths making them feasible for photonic and optically responsive cosmetic palettes. The structural diagram of the nematic self-assembly and formation of photonic films is shown in Figure 2.11 (Shopsowitz et al. 2010; Kelly et al. 2014).

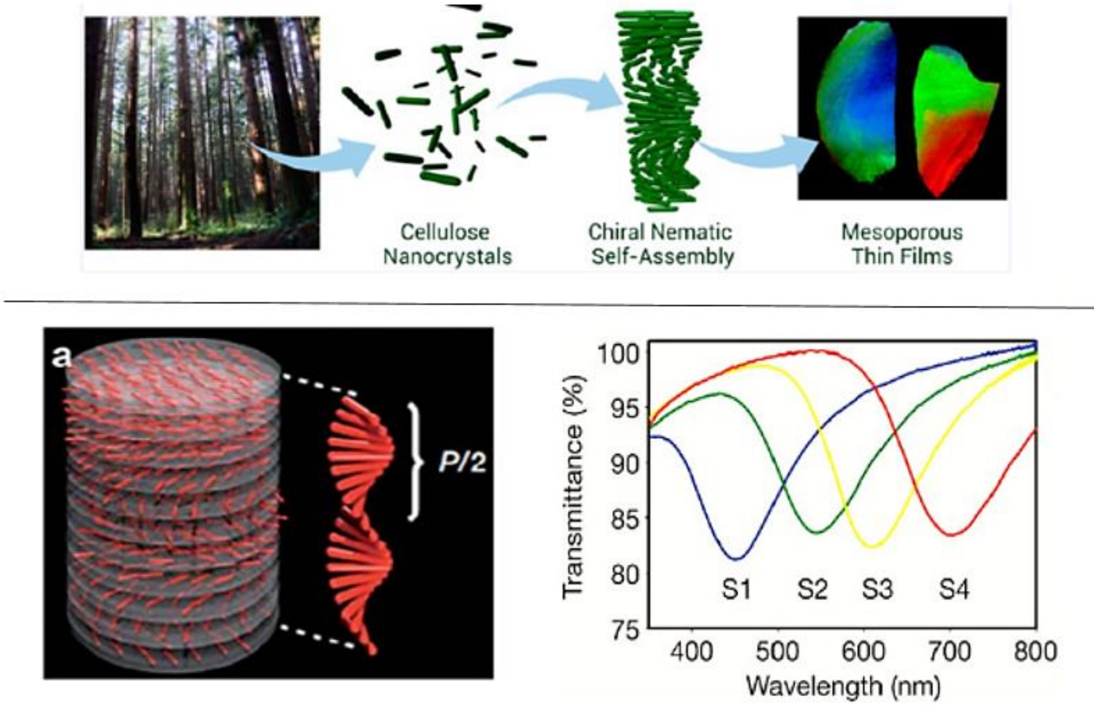

Figure 2.11: Chiral nematic behaviour of self-assembled CNC rigid rods displaying iridescent colours under specific wavelengths (Kelly et al. 2014; Shopsowitz et al, 2010).

As a biobased reinforcing nanofiller, cellulose based materials have generated significant interest for the design of crosslinked beads and sponges, defined as dispersions of air-in-solid matrix for the construction of diverse biomaterials in drug delivery, tissue engineering and personal care products. Systems such as TEMPO-mediated oxidized cellulose nanocrystals (OCN), crosslinked with alginate and divalent calcium ions (Ca^{2+}) crosslinking process have shown enhanced mechanical strength, improved porosity, and water absorption/retention capacity as measured as a function of structural stability as shown in Figure 2.12C, of oxidized CNCs and microfibrillated CNCs.

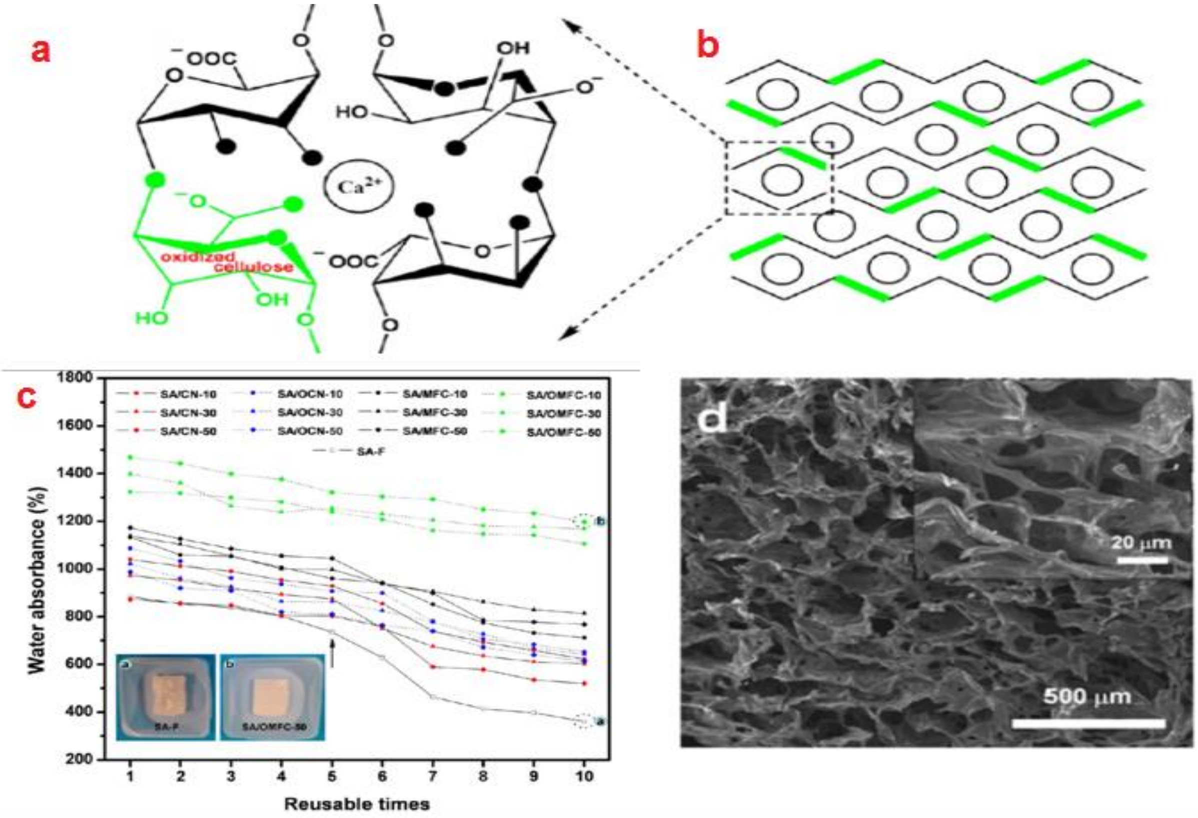

Figure 2.12: a. Molecular structure and b. schematic representation of TEMPO-mediated oxidation egg-box junction zones of cellulose/alginate/calcium system coordinated by Ca^{2+} cavity of guluronate sequences along alginate chains. c. reusable properties of the different alginate/CNC crosslinked sponges. d. SEM images of the cross-section morphology of SA/MFCNC-50 crosslinked sponge (Lin, Bruzzese, et al. 2012).

Here the rigid framework of oxidized cellulose nanocrystals serves as the coupling points for alginate-based sponges, whereas oxidized microfibrillated cellulose enact structural construction and form the semi-interpenetrating polymer network for the sponges (Figure 2.12D), having potential applications as kinetic energy absorbers, and acoustic insulating materials (Lin, Bruzzese, et al. 2012). The structural stability was evaluated from the reuse effects of the sponges, as shown in Figure 2.12C, and configurative compatibility of cellulose and alginate could stabilize the air-and-solid interface (Lin, Bruzzese, et al. 2012). In addition to being a reinforcing mediator, CNC can be readily functionalized to yield chemically crosslinked hydrogel networks from chitosan-CNC (Wang & Roman 2011), surfactant modified CTAB-CNC, or cyclodextrin (CD) grafted CNCs; for therapeutic delivery of encapsulated water soluble hydrophilic or hydrophobic anti-tumorigenic drugs (Jackson et al. 2011).

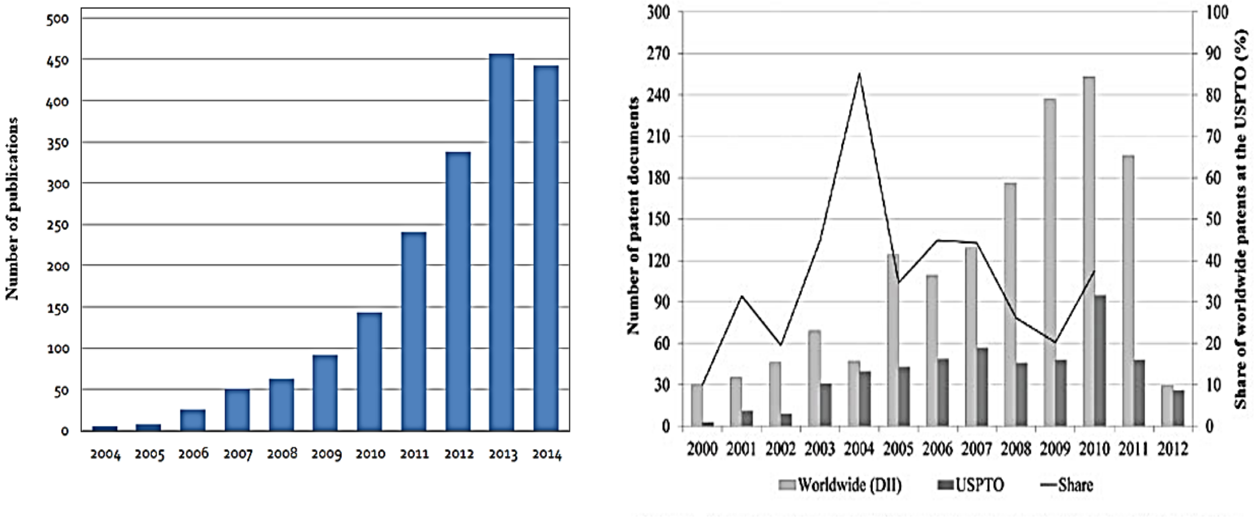

Figure 2.13: Exponential trend of the number of publications, and distribution of patent disclosures reported in relation to nanocellulose technologies in the past decade (source: Lux Research Inc. and USPTO/DII).

A narrow summary of the recent reports on nanocellulose and related materials have been discussed in this section. An exponential trend of CNC related publications and number of patent distributions in North America and worldwide shown in figure suggests the rapid growth of discoveries of this intrinsically dynamic material (Figure 2.13). With the scope of new findings and other applications still being explored, CNC notably has great potential for new discoveries and applications, which form the basis of this thesis research. A detailed design and discussion on the uncharted potential will be documented in the subsequent chapters of this thesis.

Chapter 3

Enhanced radical scavenging activity of polyhydroxylated C60 functionalized cellulose nanocrystals

3.1 Introduction

C_{60} fullerene, which is commonly classified as a “radical sponge”, has remarkable reactivity towards free radicals, making it a very attractive antioxidant. However, the potential use in personal care or biomedical applications is limited due to its inherent hydrophobic character and poor dispersibility in water. Numerous methods have been reported for the production of water-soluble fullerene systems with pioneering research in early 1990s, which included molecular complexation of C60 in host-guest interactions with water soluble macrocylces of cyclodextrins (CD) and calixarenes (Andersson et al. 1992; Atwood et al. 1994; Williams. & Verhoeven 1994). However, steric repulsion between the host-compounds reduces the stability of the dispersion of C_{60} in aqueous solution (Matsubayashi et al. 2008; Kato et al. 2009) Recent research methodologies to address the poor solubility of fullerene is through derivatization or surface modification of C_{60} with polar hydroxyl groups (-OH) (Chiang et al. 1993; Kokubo et al. 2011). These hydroxylated water-soluble fullerenes are commonly known as $C_{60}(OH)_x$, fullerols, where x represents the number of –OH groups attached to the C60 cage (Chiang et al. 1993). Simple method of synthesis, presence of carbon double bonds, high electron affinity, and polarity of the molecule makes this class of fullerenes a suitable candidate for radical-quenching in biological systems (Kokubo et al. 2011; Chiang et al. 1995). As reported previously, fullerols and their derivatives have been examined for antioxidant capacity and measured by DMPO-spin trap/ESR method, and by the beta-carotene and DPPH assay (Kato et al. 2009; Chiang et al. 1995). However, the kinetics and radical scavenging mechanism of these systems is still not properly understood. The chemically modified fullerols have been reported to form well-dispersed supramolecular solutions due to the reduced contact between the hydrophobic cores (Brant et al. 2007). Nevertheless, cluster formation via hydrogen bonds between loosely-associated C_{60} aggregates is still unavoidable and can interfere with free radical accessibility, thereby diminishing its antioxidant performance (Brant et al. 2007). Nucleation of amorphous $C_{60}(OH)_{30}$ clusters onto a suitable template is an approach to maximize the efficiency of radical quenching in an aqueous solution, in addition to gaining a greater understanding of the reaction kinetics.

This chapter contains a report for the first time of a facile and scalable methodology involving the functionalization of polyhydroxylated fullerene ($C_{60}(OH)_{30}$) on the surface of cellulose nanocrystals (CNCs). It entails improved free radical scavenging as a result of enhanced colloidal stability and immobilization of $C_{60}(OH)_{30}$ nanoparticles. The immobilization appears to be due to the covalent interaction between the –OH groups on the CNC and π-conjugation of the fullerol. An analysis of the scavenging rate and kinetics provides insights into the physical mechanism and role of the molecular structure of $C_{60}(OH)_{30}$. Cellulose nanocrystals were the choice of template on the merit of high surface area of the biocompatible and biorenewable rod-like crystal derived from cellulose fiber (via acid hydrolysis). In recent years, CNC has opened up a myriad of applications ranging from water treatment to supercapacitors due to its attractive intrinsic structural and physical properties (Peng et al. 2011; Habibi et al. 2010; Khan et al. 2012). The naturally occurring polysaccharide crystal of 100-200 nm in length and 5-20 nm in diameter has a high aspect ratio, high tensile modulus, nanoscale dimensions and hydrophilicity. It is an ideal substrate for immobilization of $C_{60}(OH)_{30}$ nanoparticles. The abundance of functional hydroxyl groups (-OH) on CNC allows for easy surface functionalization of polyhydroxylated fullerenes, with further colloidal stability imparted by the negatively charged sulfate ester groups ($SO3^-$) present on the CNC rods. A new and novel generation of aqueous based, precise nucleation of $C_{60}(OH)_{30}$ nanoparticles on CNC, which synergistically improves the antioxidant performance in comparison to $C_{60}(OH)_{30}$ clusters is demonstrated. A proposed radical-scavenging mechanism along with detailed characterization of the system using TGA, FTIR, TEM, zeta potential measurements and UV-Vis spectroscopy will be discussed.

3.2 Experimental procedures

3.2.1 Materials

Cellulose nanocrystals with length of 100-200 nm, 5-20 nm in diameter and a specific surface area of 500 m^2 g^{-1} were supplied by Celluforce Inc. All of the analytical grade chemicals including C_{60} fullerene, hydrogen peroxide (H_2O_2) (30 wt% in H_2O), tetra-n-butylammonium hydroxide (TBAH) (40% in H_2O), ammonium persulfate (APS), toluene and stable free radical 1,1-diphenyl-2-picryl hydrazyl (DPPH) were obtained from Sigma-Aldrich.

3.2.2 Methods of preparation

3.2.2.1 Synthesis of $C_{60}(OH)_{30}$-CNC

Polyhydroxylated fullerene $C_{60}(OH)_{30}$ nanoparticles were synthesized following a previously reported method by Kokubo *et al*. Preparation of $C_{60}(OH)_{30}$-CNC was conducted through in-situ chemical synthesis involving a two-step process. In the first step, the -OH groups on CNC (0.2 wt% aqueous solution) were converted to free radicals following a radical coupling reaction with ammonium persulfate (APS) for two hours, at 45 ^oC. The second step involved the addition of 5 ml of previously synthesized $C_{60}(OH)_{30}$ through the drop-wise addition under constant magnetic stirring for a total of 24 hours at 65 ^oC, to allow for as much of the converted $O^·$ radical on CNC to be captured by the electron on the C=C of fullerol to form the $C_{60}(OH)_{30}$-CNC complex. The reaction was purged with N_2 for the entire 24 hour period to minimize the generation of singlet O_2 that might interfere with the excited surface of CNC.

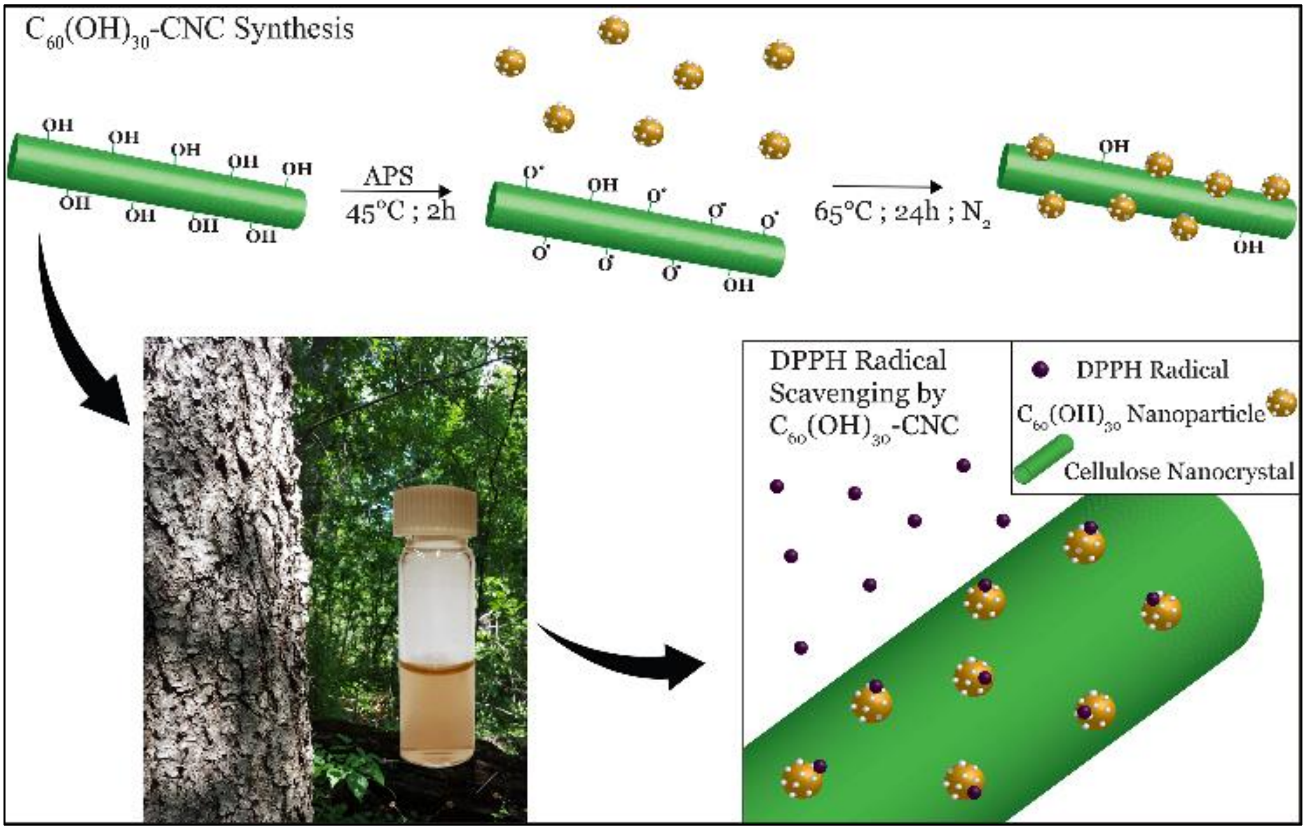

Figure 3.1: Schematic illustrating the conjugation of fullerols onto CNC.

3.2.2.2 Measurements of DPPH radical scavenging activity

All of the antioxidant tests were done using UV-vis spectroscopy. 1,1-diphenyl-picryl-hydrazyl (DPPH) was chosen as the stable free radical that displays a peak absorbance at 517nm due to its odd electron. The scavenging properties and kinetics were monitored by measuring the reduction in the absorbance at 517 nm as a function of time. A solution of DPPH in ethanol (1.3×10^{-4} M) was prepared and its UV-vis spectrum was recorded. Afterwards, 1.5 ml of this DPPH solution (1.3×10^{-4} M) was mixed with 1.5 ml of $C_{60}(OH)_{30}$-CNC antioxidant complex in a quartz cuvette, and its absorption spectra was recorded over various time intervals, with the solution under continuous stirring. A similar procedure was used for the measurements with $C_{60}(OH)_{30}$ only. Blank experiments of DPPH in ethanol and ethanol-water mixture were also performed. No reduction in the absorbance was evident after several hours confirming that there was no effect between solvent and the free radicals. Since DPPH can degrade under light, all of the reacted solutions were protected from visible light using aluminum foil wrapped around the cuvettes.

3.3 Physical and chemical characterizations

Radical scavenging reactions were monitored using an ultraviolet-visible (UV-Vis) spectrophotometer (Cary Bio 100). Transmission electron microscopic (TEM) characterization was performed using a Philips CM10 electron microscope. The samples were prepared by depositing one drop of aqueous solution (0.001 wt %) onto a carbon coated copper mesh-grid and air-dried for several hours at room temperature. Thermogravimetric analysis (TGA) was performed using TGA Q600 of TA Instruments (New Castle, Delaware). All of the experiments were conducted at a heating speed of 10 ^{o}C/min under a constant nitrogen flow rate of 10 mL min^{-1}, from 25 to 690 ^{o}C. Fourier Transform Infrared Spectra (FTIR) spectra were recorded using a PerkinElmer 1720 FTIR spectrophotometer on dried samples mixed with KBr to form pellets, which was set at a resolution of 4 cm^{-1} and analyzed using OPUS software. The zeta-potentials of the solutions were made as a function of pH from 4.0-8.0. This range was tested to check the stability of the system especially under acidic conditions using a Zetasizer Malvern Nano ZS90.

3.3.1 Thermogravimetric analysis and quantification of surface hydroxyl groups on C60

The thermogram data was analyzed to determine the amounts of $C_{60}(OH)_{30}$ conjugated to the CNC surface. Based on weight losses determined from the three TGA curves (illustrated in Figure 3.2), the residual amounts at 690 ^{o}C of $C_{60}(OH)_{30}$, $C_{60}(OH)_{30}$-CNC and CNC was 45%, 26% and 21%, respectively. The content of the $C_{60}(OH)_{30}$ on cellulose nanocrystals was determined to be 20.8% based on equation (3.1).

$$\begin{aligned} W_{cnc} + W_{Fullerol} &= 1 \\ W_{cnc} + 0.45 W_{Fullerol} &= 0.26 \end{aligned} \tag{3.1}$$

where W_{cnc} is weight percentage of CNC at 690 ^{o}C, and $W_{Fullerol}$ is the weight percentage of fullerol at 690 ^{o}C. The data was further analyzed to quantify the number of hydroxyl groups conjugated to the fullerene cage after polyhydroxylation using a well-developed method published by (Goswami et al. 2004). This approach is based on the assumption that the weight loss observed in the $C_{60}(OH)_{30}$ profile between 150 °C and 580 °C is due to the sublimation of the –OH group from the fullerene cage, which = 22.06%, and the weight loss after 580 °C is due to structural degradation of C_{60}, calculated to be 30.54%. We can then estimate the -OH groups on each fullerene molecule (x) from Eq. (3). As such, the estimated amount of -OH adhered to each polyhydroxylated C_{60} cage from equation (3.2) was determined to be 30.

$$\mathrm{x} = \frac{(C60)mol\ wt.}{(C60)mass}\ x\ \frac{(OH)x\ mass}{(OH)mol\ wt.} \tag{3.2}$$

$$= \frac{720.64}{30.54}\ x\ \frac{22.06}{17.01} = 30\ \pm 1$$

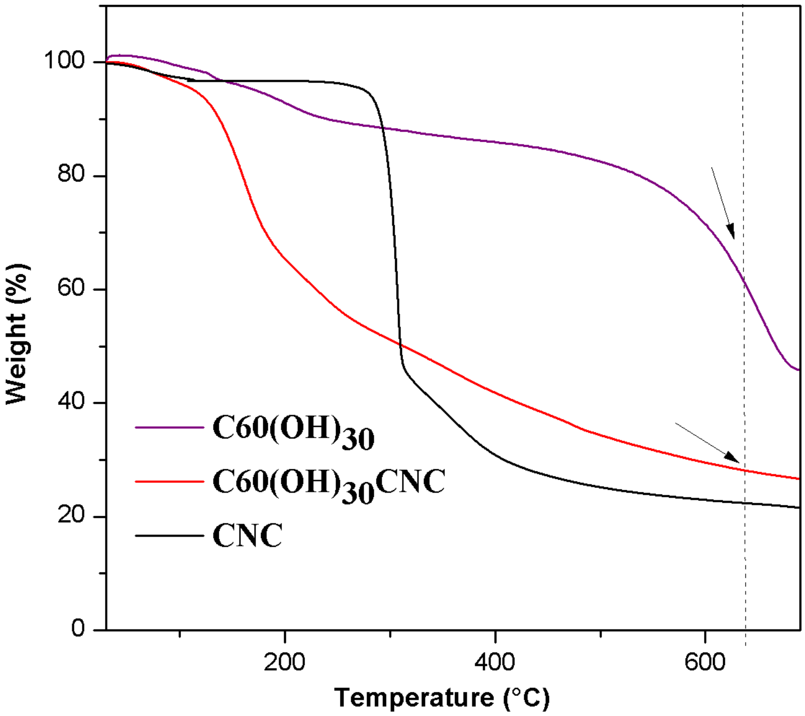

Figure 3.2: TGA thermograms of $C_{60}(OH)_{30}$, $C_{60}(OH)_{30}$-CNC and pristine CNC at a heating rate of 10 °C/min under N_2 atm.

3.3.2 Chemical verifications by fourier infrared spectroscopy

The FTIR spectra of $C_{60}(OH)_{30}$, $C_{60}(OH)_{30}$-CNC and pristine CNC is shown in Figure 3.3. The spectra of fullerol (Curve a) is dominated by a broad stretching O-H band around 3400 cm^{-1}, and three characteristic bands at 1626.41 cm^{-1} (vC=C), 1383.99 cm^{-1} (δC-O-H) and 1103.61cm^{-1} (vC-O); which has previously been reported as the diagnostic absorptions belonging to fullerols (Chiang et al. 1993; Kokubo et al. 2011; Li et al. 1993). A minor peak visible at 1723.93 cm^{-1} indicates a carbonyl group formed by the tautomerization of hemiacetals or known pinacol rearrangements of vicinal O-H groups, or through the formation of a carboxylic group formed by further oxidation of the O-H group associated with C-C cleavage of fullerene (Chiang et al. 1993). The shoulder peak at 1462 cm^{-1} and 2875.59-2963.04 cm^{-1} is attributed to residual TBAH as reported by Kokubo *et al*.(Kokubo et al. 2011). The IR spectrum of $C_{60}(OH)_{30}$-CNC (Curve b) is similar to that of pristine CNC (Curve c), with an absorption in the finger print region at 1034.91 cm^{-1} and 1060.31cm^{-1} due to C-O stretching at the C3 position of CNC (Akhlaghi et al. 2013; Kumar et al. 2014). A shift in the band observed in the $C_{60}(OH)_{30}$-CNC curve at 1112.33 cm^{-1} compared to that of CNC at 1111.47 cm^{-1}, and 1162.50 cm^{-1} in comparison to 1160.97 cm^{-1} indicates a C-O-C ester stretching motion which could be attributed to the formation of a covalent bond between CNC and $C_{60}(OH)_{30}$. Furthermore, the presence of a characteristic $C_{60}(OH)_{30}$ C-O-H peak at 1384.87 cm^{-1} and a strong band at 1637.90 cm^{-1} related to C=C of the fullerol nucleus in the $C_{60}(OH)_{30}$-CNC spectrum (Curve b), validates the interaction of $C_{60}(OH)_{30}$ with CNC.

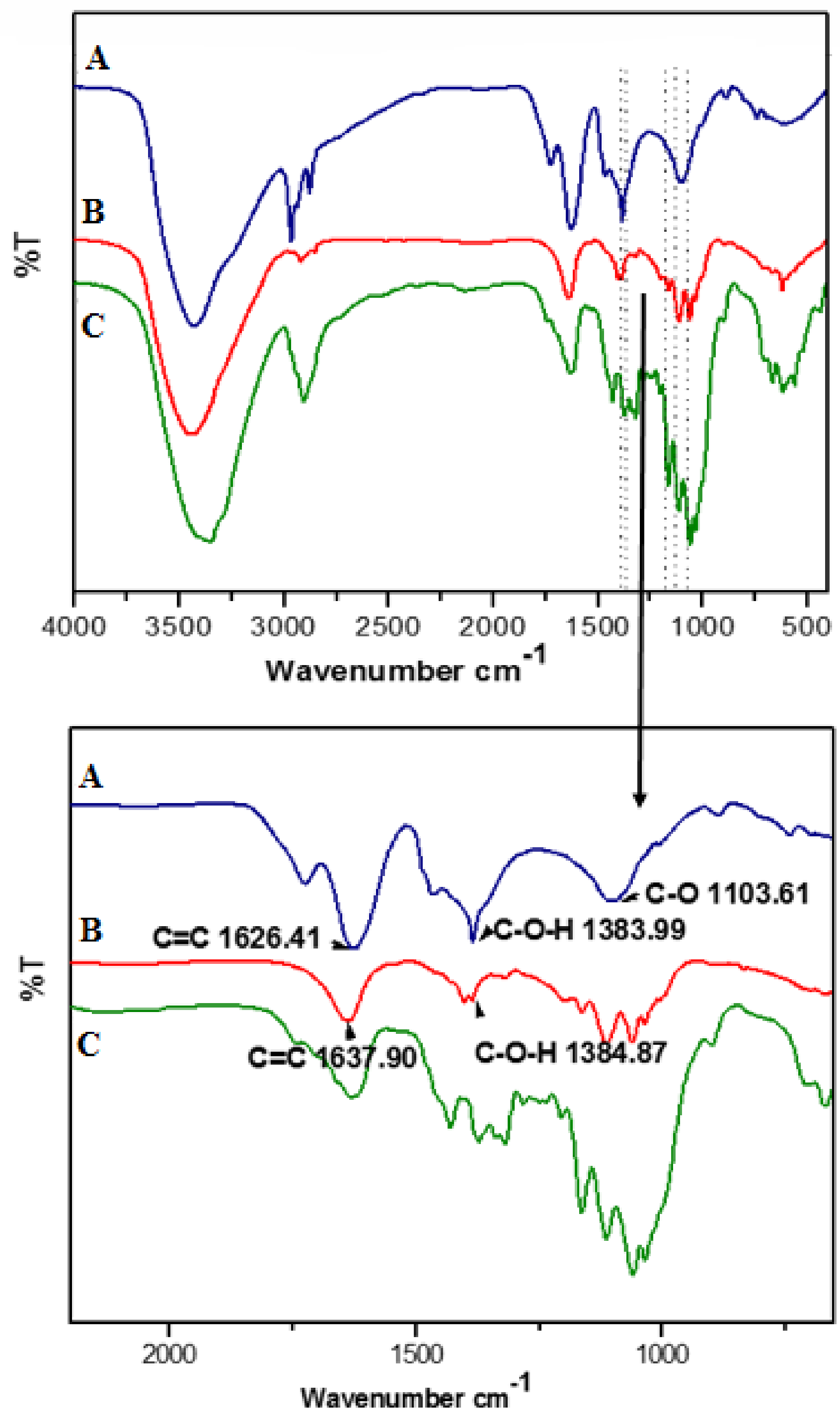

Figure 3.3: FTIR spectra of (a) $C_{60}(OH)_{30}$, (b) $C_{60}(OH)_{30}$-CNC, and (c) pristine CNC.

3.3.3 TEM micrographs of the CNC supported antioxidant hybrid structure

Measurements by TEM elucidated the shape and morphology of the $C_{60}(OH)_{30}$ clusters, and $C_{60}(OH)_{30}$-CNC. The images of $C_{60}(OH)_{30}$ revealed relatively large spherical nanoparticles packed into clusters of size ranging from 20-400 nm, as illustrated in Figures 3C and 3D. This is due to the characteristics of polyhydroxylated fullerol nanoparticles in water, where they tend to form loosely associated aggregated clusters (Brant et al. 2007). The large aggregates were almost eliminated once the fullerols were grafted onto the surface of CNC rods, as shown in Figure 3.4B (tiny black dots). This phenomenon is caused by the increased probability of nucleation on the high specific surface of CNC where single fullerol nanoparticles can be conjugated to the excited CNC surface. Figure 3.4A shows the TEM image of pristine CNC rods with no $C_{60}(OH)_{30}$ growth in comparison to the hybrid system.

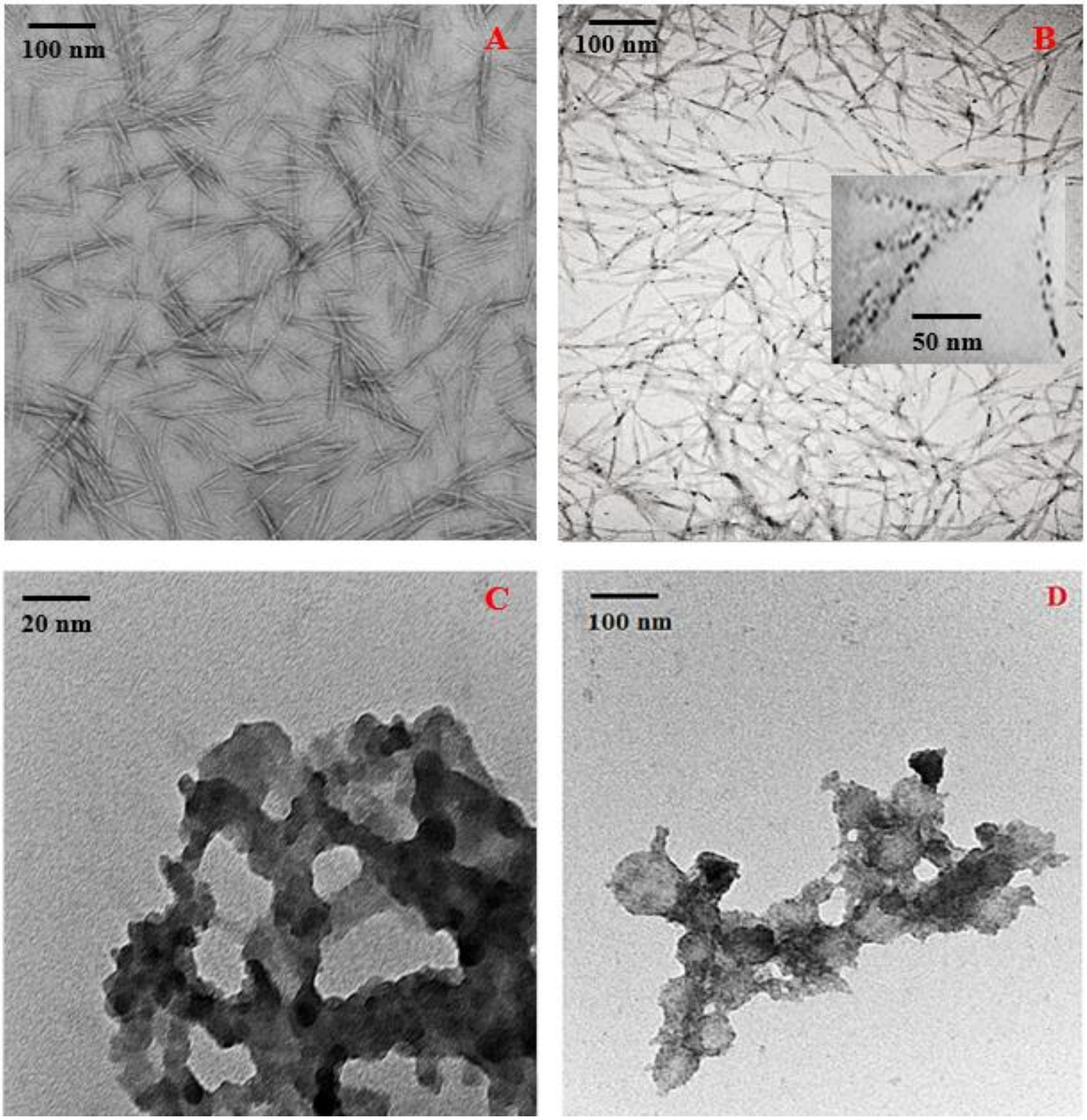

Figure 3.4: TEM images of a) pristine CNC b) $C_{60}(OH)_{30}$-CNC, c) and d) are both pure $C_{60}(OH)_{30}$ clusters of different sizes. The inset in figure 3b details the structure of the nanohybrid with fine sized $C_{60}(OH)_{30}$ nanoparticles on the surface of cellulose nanocrystals.

3.3.4 Zeta potential measurements of colloidal stability

The zeta potential (ZP) indicated the colloidal stability of the suspension by measuring the surface charge of the nanoparticles. All zeta potentials were measured as a function of pH ranging from 4.0 - 8.0. The results are summarized in Table 3.1. The ZP for the pristine CNC remained stable with a value of -31mV, which corresponds to the highly charged character of the nanocrystals. Strong pH dependency was observed for the fullerol nanoparticles due to the high degree of hydroxylation of the molecules, as reported in the literature (Brant et al. 2007; Assemi et al. 2010). The fullerols displayed weak negative charge (-12.2 mV to -23.9 mV), and were found to be unstable in acidic medium at pH < 6, and became more stable in alkaline pH due to deprotonation of -OH groups and the presence of partially ionized COO^- groups (Assemi et al. 2010). In comparison, the $C_{60}(OH)_{30}$-CNC aqueous dispersion yielded an overall high negative surface charge ranging from -39.9 mV to -42.3 mV indicating enhanced colloidal stability and reduced tendency to flocculate at all pH values especially in the acidic conditions. This is a prime factor in determining the suitability of this antioxidant system in a given practical application for cosmetics, where the natural skin surface pH is acidic (Lambers et al. 2006).

Table 3.1: Zeta Potentials measurements and reported standard error (S.E) of $C_{60}(OH)_{30}$-CNC, $C_{60}(OH)_{30}$ and CNC at different pH values.

Sample	pH				
	4.0	5.0	6.0	7.0	8.0
$C60(OH)_{30}$-CNC	-42.3 ±1.47	-42.4 ±2.06	-35.0 ±2.01	-41.0 ±0.30	-39.8 ±3.50
$C60(OH)_{30}$	-12.2 ±0.92	-18.4 ±1.02	-23.9 ±3.27	-31.2 ±1.25	-48.3 ±1.71
CNC	-32.2 ±2.27	-36.3 ±1.95	-31.5 ±1.35	-40.5 ±3.82	-46.8 ±1.96

3.3.5 UV-Vis spectroscopy

The free radical scavenging properties by $C_{60}(OH)_{30}$-CNC were assessed by UV-Vis spectroscopy. The stoichiometry between free radical consumption and colour change (purple to orange) was monitored over time at 517 nm, as illustrated in Figure 3.5. There was an appreciable reduction in the absorbance in the UV spectrum through the reaction of DPPH with $C_{60}(OH)_{30}$-CNC; the absorbance decreased from 0.9 (at 1 min), to an absorbance of 0.56 after 4 hours. At infinite time (after 6 days), the characteristic peak for DPPH at 517 nm in the presence of $C_{60}(OH)_{30}$-CNC disappeared, due to complete quenching of the radical by $C_{60}(OH)_{30}$-CNC.

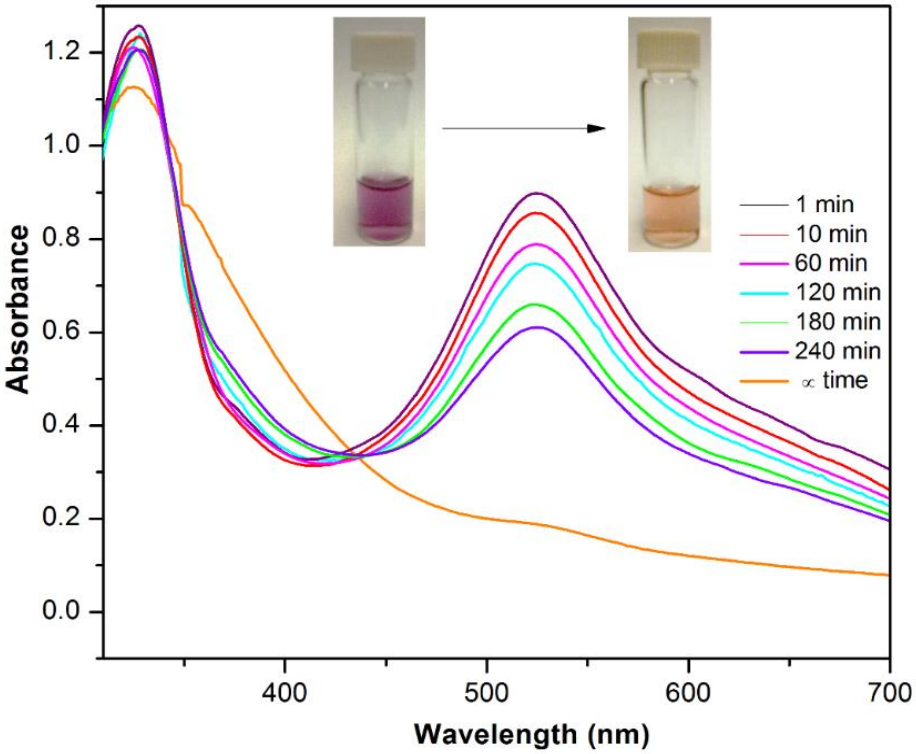

Figure 3.5: The change in UV-Vis spectra over time caused by the radical scavenging of the stable free radical DPPH with $C_{60}(OH)_{30}$-CNC, monitored at 517 nm. The images at the top of the figure shows the bleaching of the coloured radical from purple to orange.

3.4 Results and discussion

3.4.1 Kinetic analysis and pseudo first-order modelling of the antioxidant activity

To further understand and quantify the rate of antioxidant activity, the kinetics of the reaction between DPPH and $C_{60}(OH)_{30}$-CNC and DPPH and $C_{60}(OH)_{30}$ was modelled by 2-stage pseudo-first order kinetics using Equation (3.4).

$$ln\frac{(A_\infty - A_t)}{(A_\infty - A_0)} = -kt \tag{3.4}$$

where t is time and A_∞,A_t, A_0 are absorbance at infinite time (6 days after the experiment), at time t, and zero, respectively. Here, the reaction follows pseudo-first order kinetics. In the initial stages of the reaction, there are several active sites available on $C_{60}(OH)_{30}$ grafted onto CNC. Each C_{60} molecule is capable of reacting with multiple DPPH radicals, hence in terms of molar equivalents, the concentration of C_{60} is higher than DPPH (Geckeler & Samal 2001). The concentration of DPPH decreased steadily over time, while the concentration of $C_{60}(OH)_{30}$-CNC remained constant. The plot of the term $\ln[(A_\infty - A_t)/(A_\infty - A_0)]$ vs time is shown in Figure 3.6. The rate of the radical scavenging and analysis of the standard curve displayed two stage kinetics (Figure 3.6a) consisting of a very rapid initial step from 0-10 minutes defined by the rate constant $k_1 = 6.7 \times 10^{-3}$ min^{-1}, followed by a slower reaction with the rate constant $k_2 = 2.0 \times 10^{-3}$ min^{-1}; both stages display satisfactory R^2 values of 0.9707 and 0.9868, respectively. Modelling of the kinetic behaviour of $C_{60}(OH)_{30}$ alone displayed a similar two-stage trend but with lower rate constants (see Figure 3.6b). The results are in agreement with the hypothesis, where the nanohybrid structure demonstrates a higher antioxidant activity because there is an exact nucleation of single $C_{60}(OH)_{30}$ nanoparticles due to the high specific area and excited surface of cellulose nanocrystals (CNC) substrate. Whereas, the fullerol $C_{60}(OH)_{30}$ particles on their own tend to form loosely bound clusters of spherical particles in aqueous solution, as shown in the TEM micrographs in Figure 3c and d. From a geometric standpoint these relatively large clusters make it difficult for the radical to react fast enough in comparison to the single nucleated particles on the surface of CNC. As a result, the hybrid structure not only demonstrates antioxidant capabilities, but this performance is also enhanced in the CNC-$C_{60}(OH)_{30}$ structure.

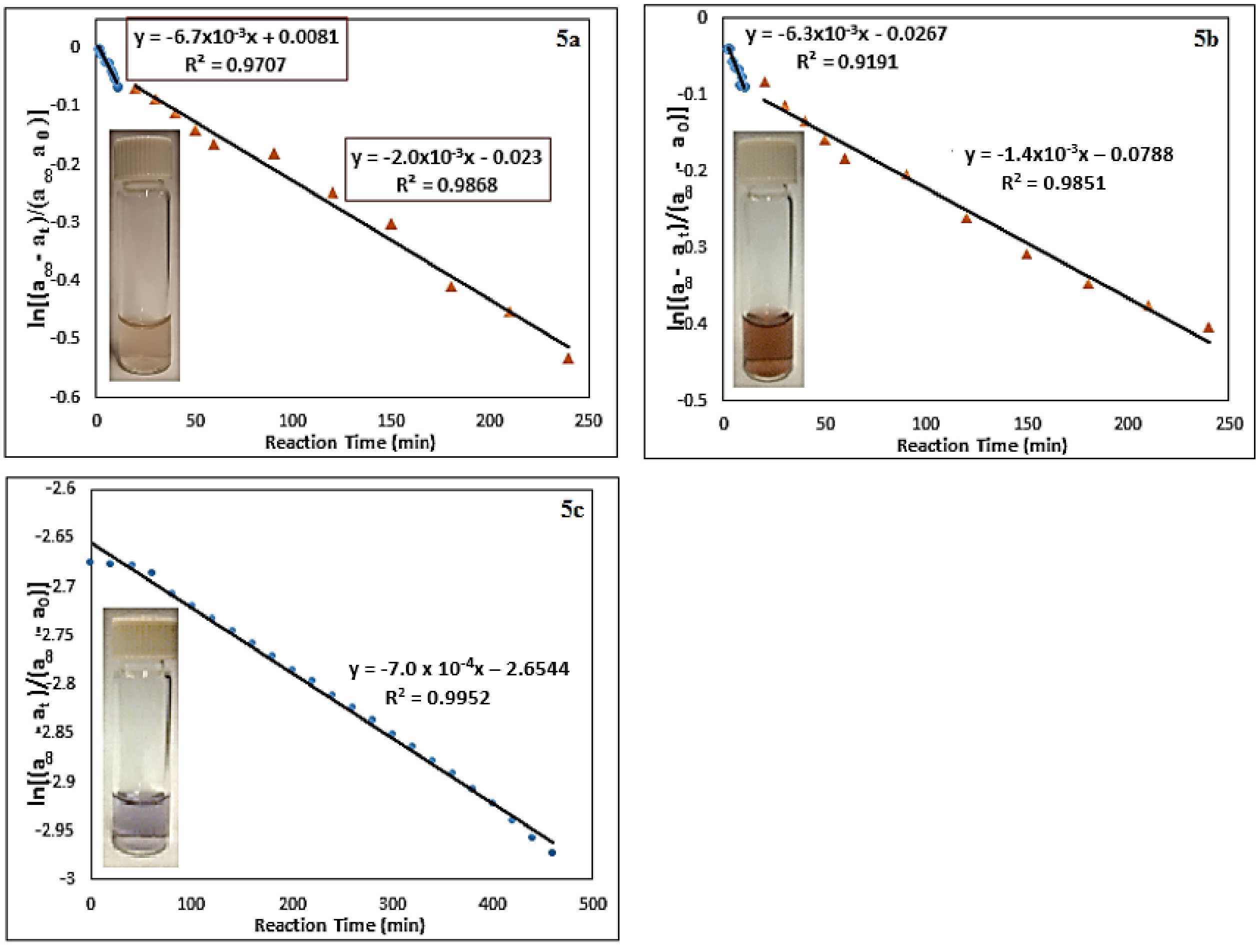

Figure 3.6: The changes in the kinetics of the DPPH scavenging reaction with a) $C_{60}(OH)_{30}$-CNC b) $C_{60}(OH)_{30}$ and c) pristine fullerene C_{60}.The insets in each figure represent visual images of the dispersions a) $C_{60}(OH)_{30}$-CNC in aqueous solution b) $C_{60}(OH)_{30}$ in aqueous solution and c) C_{60} in toluene solution.

3.4.2 Proposed Reaction mechanism of DPPH scavenging of $C_{60}(OH)_{30}$-CNC

An understanding of the interaction mechanism, and the experimentally derived pseudo-first order reaction kinetics of the two systems was developed based on the molecular structure of fullerol $C_{60}(OH)_{30}$. A proposed mechanism to explain the two stages is shown in

Figure 3.7. It is proposed that the first-stage of the kinetics can be attributed to rapid hydrogen atom abstraction from the -OH groups of the highly hydroxylated fullerol, resulting in the formation of the epoxy bonds (Figure 3.7, stage 1) which are energetically more favourable to reduce the strain on the hydroxylated fullerol cage through the conversion of sp^3 carbons to sp^2 hybridization. It is suggested that hydroxylation of fullerene renders a large stress on the C60 cage due to the sp^3 carbons inability to exist in an energetically favorable tetrahedral orientation (Ueno et al. 2014). As such, in order to relieve this strain from the cage the radical has to react with the -OH group first (defined by rate constant 1, Figure 3.6a), followed by the second stage (rate constant 2, Figure 3.6a) where it reacts with the π-conjugated double bond with subsequent electron transfer from the C=C bond to the DPPH radical (Figure 3.7, stage 2). In addition, unlike C_{60} with its intact π-conjugated system, it is difficult for the radical to freely interact with the C=C bond due to steric hindrance from -OH groups on the surface of the cage, and the less accessible reaction sites (Ueno et al. 2014). Therefore, the DPPH radical is likely to first react with the labile H atom of -OH, followed by radical addition to the remaining C=C bond of the fullerol nucleus in order to release the constrained energy (Brand-Willliams et al. 1995; Ueno et al. 2014). In further support of the proposed mechanism for the two stages, a control experiment between pristine fullerene and DPPH was conducted. The reaction kinetics of the fullerene in the absence of hydroxyl modification yielded only a one single-stage kinetic process defined by the equation $y = -7.0x10^{-4}x - 2.6544$ with a linear correlation of 0.9952, as illustrated in Figure 3.6c. The results confirmed that the DPPH free radicals only react with electrons on the π- conjugated C=C surface of the unmodified fullerene molecule, leading to the observed one-stage kinetic trend.

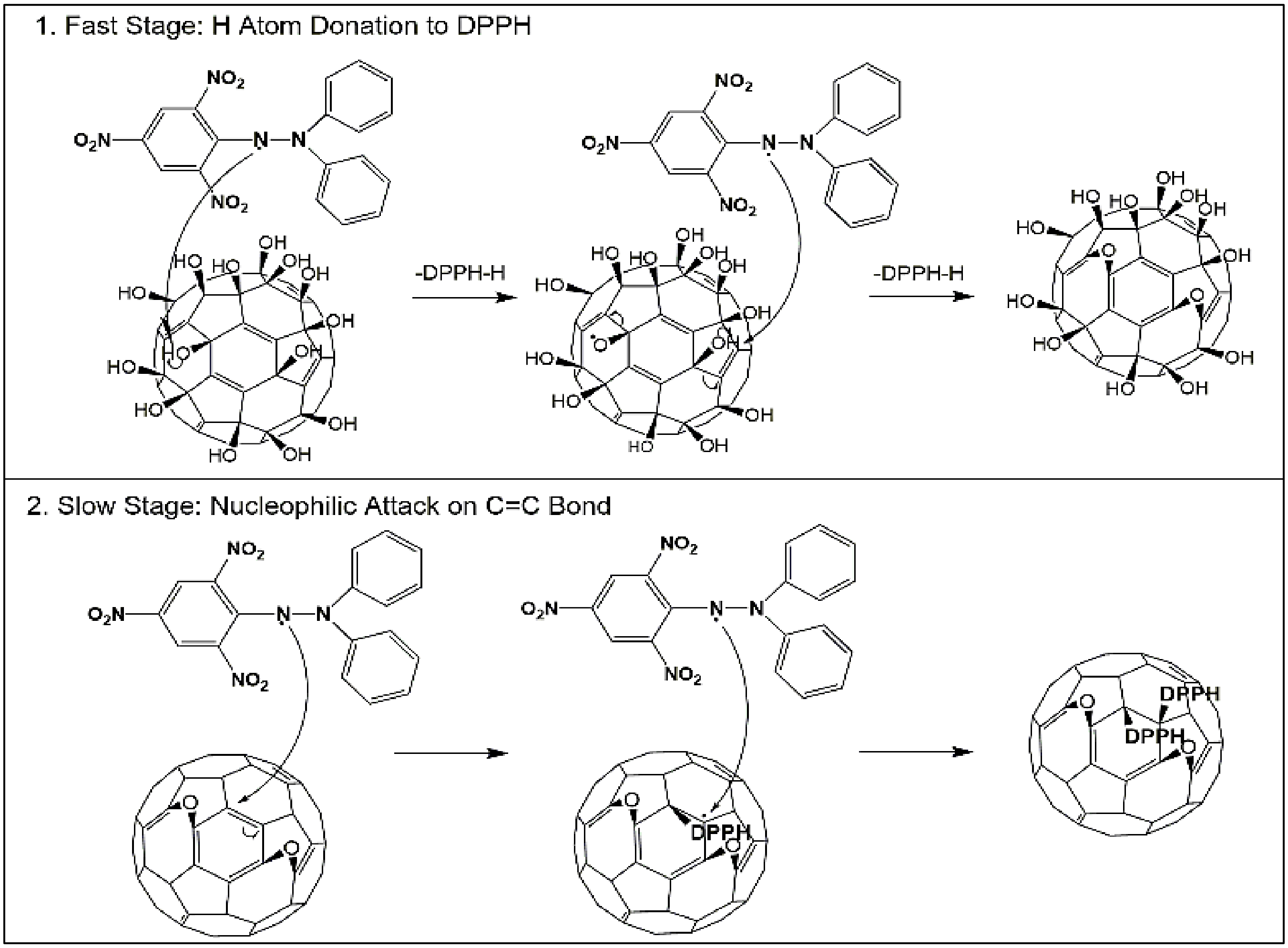

Figure 3.7: Proposed reaction mechanism for the scavenging of the DPPH radical by $C_{60}(OH)_{30}$ through the very fast first stage of H-atom donation followed by a slower second stage via addition to C=C.

3.4.3 Active comparison of the antioxidant capacity of $C_{60}(OH)_{30}$-CNC and $C_{60}(OH)_{30}$

To demonstrate the efficacy of the system, a concentration dependent antioxidant study was conducted for $C_{60}(OH)_{30}$-CNC and $C_{60}(OH)_{30}$ at different concentrations (0.1mg ml^{-1}, 0.05 mg ml^{-1} and 0.025mg ml^{-1}). To ensure a realistic comparison, each of the concentrations corresponds to the active ($C_{60}(OH)_{30}$) compound present in each system. Figure 3.8 shows that the rate constants decrease with decreasing concentrations for the two systems. Rate constants for reaction of DPPH with $C_{60}(OH)_{30}$-CNC displayed much higher and faster k_1 and k_2 values compared to $C_{60}(OH)_{30}$ alone. Improved antioxidant performance of the $C_{60}(OH)_{30}$-CNC system is a result of the templating effect of CNC. Grafting $C_{60}(OH)_{30}$ on the high surface area of CNC minimizes the tendency for unwanted growth and cluster formation of fullerol, thereby making the active material ($C_{60}(OH)_{30}$) more accessible to the DPPH radicals.

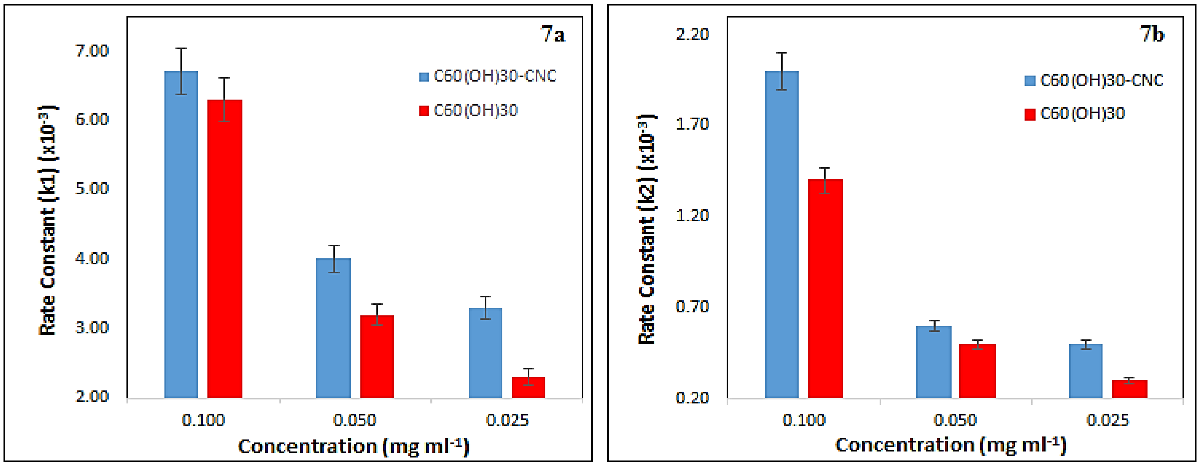

Figure 3.8: Concentration dependent comparison of the two rate constants (Figure 7a, k_1) & (Figure 7b, k_2) observed for $C_{60}(OH)_{30}$-CNC and $C_{60}(OH)_{30}$, respectively. Concentrations on the x-axis are representative of the active material ($C_{60}(OH)_{30}$) in each system.

Chapter 4

Surface modified cellulose nanocrystal/semiconductor hybrids for systematic control of photocatalytic activity and ultraviolet protection

4.1 Introduction

Recent advances in the epitaxy of semiconductor materials have made it possible to fabricate metal oxide structures in which confined electrons(e^-) and holes(h^+) have the potential to fine-tune the redox functionalities (Cao et al. 2009; Dietl 2010). For solid-state systems, ZnO semiconductors with a wide band gap energy of 3.37 eV, and with inherent UV absorbing properties have been considered a promising candidate over other inorganic nanomaterials. This is attributed to the high quantum efficiency, that finds applications in optical devices, sensors, transparent electrodes, solar cells, photocatalysis, antibacterial activity and cosmetics (Kołodziejczak-Radzimska & Jesionowski 2014; Cheng et al. 2014; Fu et al. 2015). For these applications, the structural defects, morphology, size, surface area, and crystallinity are prime factors that determine the efficacy of the metal oxide. The majority of the research in this field has focused on strategies to address these ensuing properties mainly through the introduction of oxygen vacancies, structural defects on the surface of the crystal and widening the band gap of the metal oxide to limit the fast recombination of photogenerated charge carriers (Cheng et al. 2014). Doping with a variety of materials including, both, metal ions (Dao et al. 2016; Sun et al. 2011; Jimenez-Gonzaez, A.E, Urueta, J, A. and Suarez-Parra 1998) and metal oxides (Etacheri et al. 2012; Cheng et al. 2014; Liao et al. 2008; Sun et al. 2014) have shown that such bandgap tailoring is possible and the scope is promising for functional optoelectronic devices. But in an area where the formulation is in the solution phase, colloidal ZnO nanocrystals still pose a challenge because of their tendency to aggregate due to Ostwald ripening resulting from the high surface energy (Kołodziejczak-Radzimska & Jesionowski 2014). As a result, these nanoparticles (NPs) are unstable during storage and compromise their surface reactivity in applications, such as waste water treatment, photocatalysis, personal care or biological systems. The possibility of using hybrid nanocomposites to fabricate functional cosmetic systems in aqueous system suggests the feasibility of transferring this technique to large scale application, an achievement that would offer many attractive advantages including, product efficacy, solution stability, sustainability, and aesthetic appeal. A novel synthetic strategy that has the flexibility to meet these demands is a cellulose based nanorod derived from wood pulp known as cellulose nanocrystals (CNCs). The biocompatible 100 x 20 nm dimensional crystalline domains extracted from wood fiber, are excellent substrates for the growth of semiconductor ZnO NPs. The well-controlled nanocrystal derived from nature offers high specific surface area, long term stability in water, confined dimensions and mechanical strength over other biomass derivatives (Habibi et al., 2014).

Here, the prospect of employing CNC in personal care and cosmetic applications is an uncharted and increasingly exciting field. With this objective, the scope of the present study is to investigate how an experimental edifice can be constructed to exploit the unique physical and chemical properties of cellulose nanocrystal, and render it an active semiconductor for multifunctional cosmetic application. By combining the semiconductor ZnO with biocompatible CNC template, we can synergize their properties for nanostructure fabrication that could lead to a breakthrough in cosmetic nanotechnology. The present study focuses on the design of an optimal ratio for the synthesis of a highly porous nanohybrid system for the application as a UV filter and photocatalytic agent for the degradation of organic pollutants. This structure was developed on a melamine formaldehyde (MF) coated CNC template that provides a mesoporous and nitrogen-rich substrate for the growth of ZnO nanoparticles in aqueous solution, without high temperature calcination. First, the UV-absorbing property of the nanohybrid was applied for the in-vitro evaluation of the sun protection factor (SPF) through spectrophotometric analysis, where the role of the template revealed the importance for the size control of ZnO NPs displaying enhanced SPF values. Second, the photocatalytic degradation of an organic dye methylene blue, under UV and solar radiation was evaluated by fitting the reaction to a pseudo-first order Langmuir-Hinshelwood model, and elucidated by solid band theory. There was a 4-fold increase in the photocatalytic performance of ZnO@MFCNC hybrid resulting from (1) an increased surface area of the MFCNC matrix, (2) confined surface energy and growth of the ZnO NPs, and (3) a fast promotion of interfacial charge-transfer to the surface of the catalyst. This is in part due to the mesoporous core-shell structure of the MFCNC that traps the photo-induced charge carriers and prevents e^-/h^+ recombination without the additional band gap tailoring or structural defects on the surface. A complete analysis and characterization of the system through, FTIR, TGA, XRD, zeta potential measurements, UV-Vis and TEM is presented to validate the scope of the material.

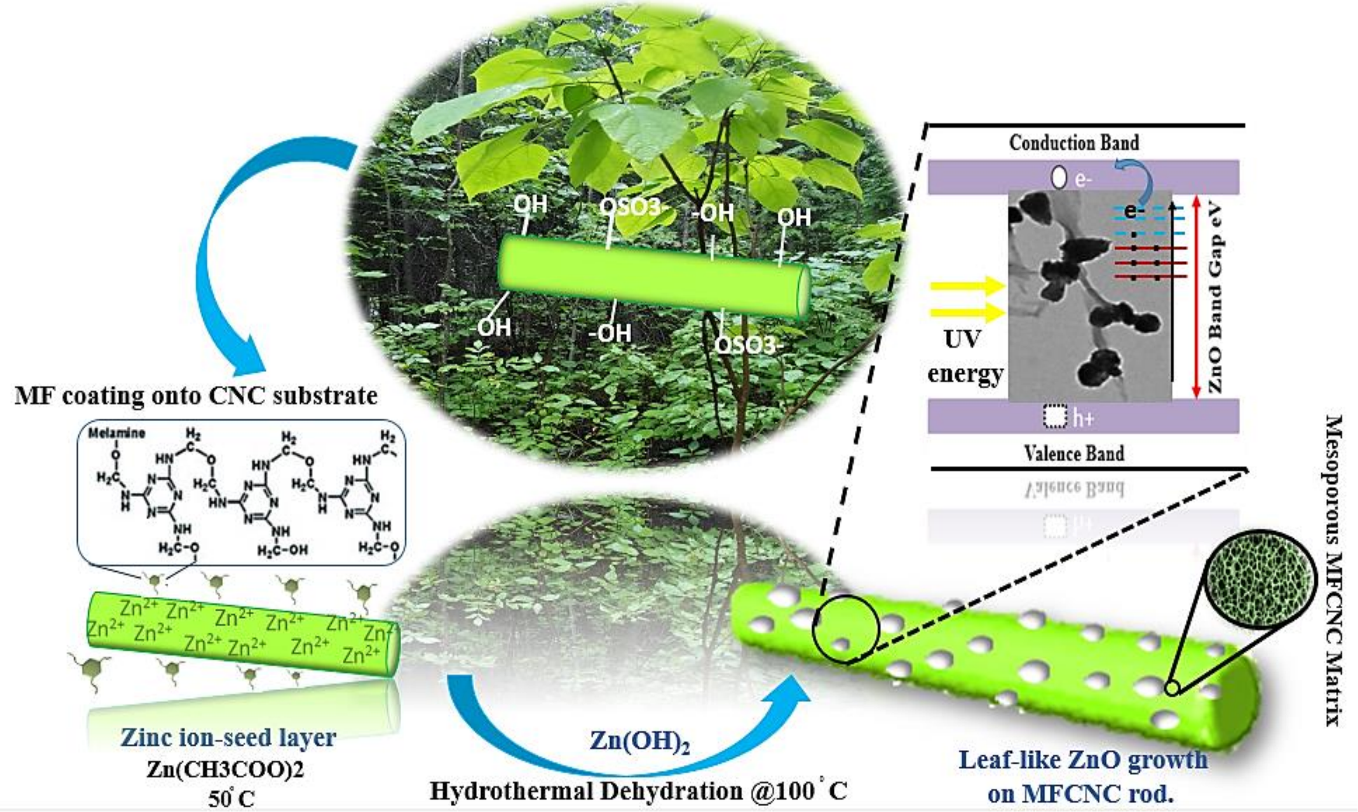

Figure 4.1: Schematic illustration of the synthesis of semiconductor ZnO on the surface of Melamine-formaldehyde (MF) coated CNC rods.

4.2 Experimental Section

4.2.1 Materials

Cellulose nanocrystals with dimensions 100-200 nm in length and 5-20 nm wide were supplied by Celluforce Inc. Quebec, Canada. All of the analytical grade chemicals were purchased from Sigma-Aldrich, and used as received.

4.2.2 Method Preparations

4.2.2.1 Synthesis of semiconductor ZnO on the surface of CNC

Step 1. Melamine formaldehyde coated CNCs were prepared through the poly-condensation of MF precursor on the CNC rod as described previously (Wu et al. 2015).

Step 2. The reaction of the optimal hybrid ratio involved dispersing 142.9 mg of MFCNC in 15 ml of water. After which 164.6 mg of zinc acetate dehydrate was dissolved in another 15 ml of water and added dropwise to the MFCNC solution and stirred at 50 °C for 1 hour. This allowed for seed layer deposition of positively charged zinc ions that chelated through the nitrogen base of the MFCNC rods.

Step 3. From here, 0.0225mol/30 ml solution of NaOH was introduced dropwise for the hydrolysis of the Zn^{2+}@MFCNC solution, and allowed to stir at room temperature for 2 hours.

Step 4. The samples were exposed to hydrothermal treatment at 100 °C for 1 hour, and subsequently purified through dialysis. Preparation of pure ZnO followed the same process but without the additional template of MFCNC. The procedure involved 164.6 mg of zinc acetate dihydrate (Zn^{2+}) pre-dissolved in 15 ml of water and reacted with 0.00225mol/30ml of NaOH at room temperature for 2 hours, followed by hydrothermal treatment and purification as described above. A schematic for the synthesis route is illustrated in Figure 4.1.

4.2.2.2 In-vitro measurements of the Sun Protection Factor (SPF)

The absorption characteristics of the sunscreen agents were determined based on spectrophotometric analysis of dilute aqueous solutions for ZNO@MFCNC and pure ZnO based on 5% active ingredient. Samples were diluted in water at a final concentration of 2 μl/ml and analyzed by UV spectrophotometry from 290 to 800 nm, at every 5 nm intervals using 1 cm quartz cell, according to Mansur's method (Mansur, Breder, Mansur, Azulay 1986) . Water was used as a blank sample for the baseline correction. All of the tested materials were synthesized and reproduced three times to obtain a good reproducibility and the standard error for the SPF measurements.

4.2.2.3 Photocatalytic evaluation

UV: 50 mg of ZnO@MFCNC powder was reacted with 50 ml of 0.02mg/ml methylene blue (MB) solution. The reaction was sonicated and vortexed to allow for a uniform dispersion of the hybrid powder and stirred in the dark for 1 hour to reach equilibrium absorption-desorption. Next, the solution was exposed to high intensity UV irradiation using a 100 Watts lamp where 3 ml aliquots were withdrawn at 20 min intervals, diluted to 1:10 ratio, and centrifuged for 10 min at 7000 rpm. The absorbance was recorded subsequently using an ultraviolet-visible (UV-Vis) spectrophotometer (Cary Bio 100) measured from 200-800 nm at every 1 nm intervals. The reaction was carried out to 240 min at which point the hybrid material degraded to completion. A parallel study for comparison of the photocatalytic performance of pure ZnO accompanied using the exact same process and carried out to 360 min at which point complete degradation of the unmodified ZnO was observed. All of the experiments were repeated three times to ensure accuracy of the analysis.

Sunlight: Identical reaction conditions were setup for the evaluation on the effect of sunlight on the photocatalytic performance of the hybrid and pure ZnO. 3 ml aliquots were withdrawn every 10 min for complete analysis of the reaction. The experiments were performed outdoor from 12:00 – 4:00 pm in late July and early August, with an average UV index of 8. The temperature of the reaction was monitored with a temperature probe, and the solutions were sealed to avoid evaporation.

4.3 Material Characterization

Optical, SPF and photocatalytic measurements were monitored using an ultraviolet-visible (UV-Vis) spectrophotometer (Cary Bio 100). Thermogravimetric analysis (TGA) was performed using TGA Q600 of TA Instruments (New Castle, Delaware). The experiments were conducted at a heating speed of 20 ^{o}C/min under air, from 25 to 800 ^{o}C. Morphology of the uranyl stained CNCs was obtained through JEM-2100 high resolution TEM (HRTEM). MFCNC, ZnO@MFCNC and unmodified ZnO particles were characterized using Philips CM10 Transmission electron (TEM). X-ray diffraction (XRD) patterns of the samples were performed with a Rigaku D/MAX-RB diffractometer using filtered Cu Kά radiation. Fourier Transform Infrared Spectra (FTIR) spectra were recorded using a PerkinElmer 1720 spectrophotometer of freeze dried samples mixed with KBr, at a resolution of 4 cm^{-1}, and analyzed using OPUS software. The zeta-potentials of the solutions were carried out as a function of pH from 3.0-5.0, every 0.5 unit. This range was tested to check the stability of the system by measuring the surface charge of the nanoparticles using a Zetasizer Malvern Nano ZS90. A Blak-Ray B-100AP-R High Intensity (100 Watts) 365 nm 2.5 Amps, 115V-60 Hz Lamp was used for UV irradiation of all samples.

4.4 Results and discussion

4.4.1 X-ray diffraction patterns of the growth of crystalline ZnO

Typical diffraction peaks in the MFCNC spectra observed at $2\theta = 18.5^{o}$, and the ones marked with (*) come from cellulose 1, of the CNC structure. XRD data confirmed that all of the samples produced (without any additional calcination) were crystalline and had phase transformations corresponding to bulk ZnO matching the reported literature values (Meulenkamp 1998; Mumalo-Djokic et al. 2008; P.B. Taunk, R. Das, D.P. Bisen 2015). The highest intensity peak of the (101) plane observed along with other smaller intensity peaks at 100, 002, 101, 102, 110,103 112 and 004 were indexed to the hexagonal wurtzite ZnO structure, as shown in Figure 4.2. These diffraction patterns were then analyzed using the Debye-Scherrer formula (Equation (4.1)) to determine the crystalline size of the ZnO-NP present on the nano-hybrid:

$$\mathrm{D}_{hkl} = \frac{k\lambda}{\beta\left(\frac{\pi}{180}\right)cos\theta} \tag{4.1}$$

where, D_{hkl} is the crystallite size in (nm) perpendicular to the crystal (*hkl*) plane, k is a constant equal to 0.94, λ is the wavelength of the incident X-ray radiation [CuKά (0.154 nm)], β is the full width at half maximum (FWHM) in radiations, (π/180) is the correction factor to convert β into radians, and θ is the scattering angle for the (*hkl*) plane. The size calculated for the pure ZnO crystal was found to be 39.903 ± (1 nm), whereas the crystalline size of the ZnO on the ZnO@MFCNC hybrid was 15.19 ± (1 nm). The estimated crystallite sizes of the two samples agreed with the X-ray diffraction patterns shown in Figure 4.2, since larger crystal size linked to pure ZnO were characteristically associated with more pronounced sharp intensity peaks, whereas the smaller and more broad peaks (belonging to ZnO@MFCNC spectra), were subjected to smaller crystal size. (Mumalo-Djokic et al. 2008; Taunk, Das, Bisen 2015). Additionally, the presence of these crystal planes and intensity peaks confirmed the successful formation of ZnO-NPs on the surface of MFCNC.

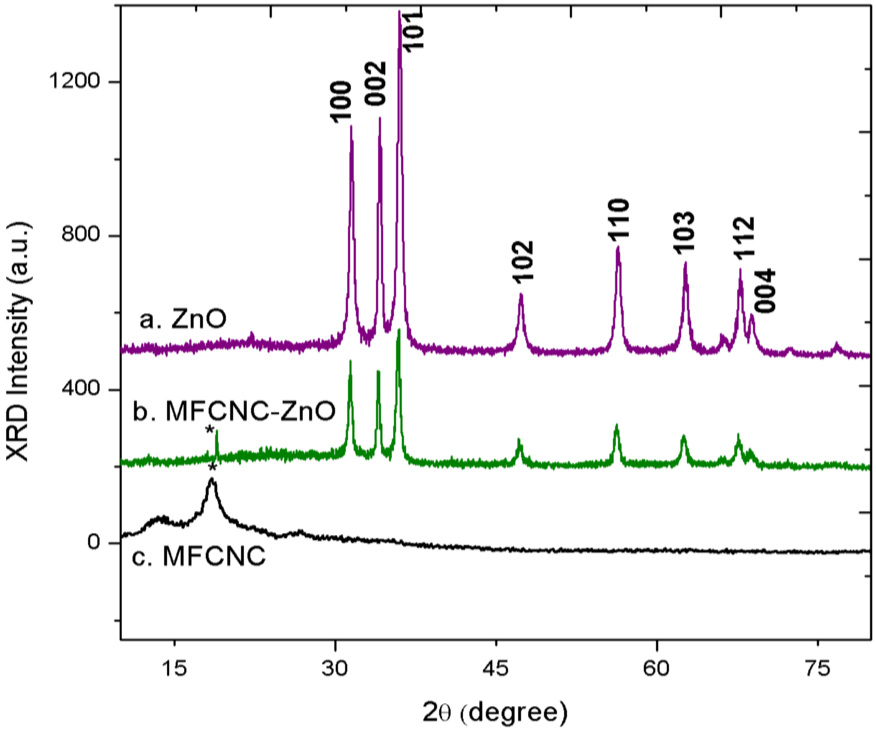

Figure 4.2: X-ray diffraction (XRD) patterns of MFCNC, as synthesized ZnO and ZnO@MFCNC nanocomposite.

4.4.2 FTIR spectroscopy

The FTIR spectra shown in Figure 4.3 confirmed the chemical characteristics of ZnO@MFCNC nanocomposite, as well as MFCNC and pure ZnO. The IR spectra of pure ZnO is normally recognized by the characteristic vibrational assignment at 430–500 cm^{-1} due to the Zn-O stretching vibration, and broad peaks in the range of 3800-3900 cm^{-1} attributed to adsorbed H_20 molecules present on the lattice as shown in Figure 4.3 (Jimenez-Gonzaez, Urueta, and Suarez-Parra 1998). For comparative analysis, the IR Spectra for the MFCNC-ZnO (Figure 4.3) hybrid were analyzed. The presence of the distinct absorption at 428 cm^{-1} (Figure 4.3, curve b) ascribed to the stretching vibration of Zn-O bond validated the formation of the crystal on the nanocomposite. Another noticeable peak at 813 cm^{-1} arises from the 1,3,5-triazine ring of melamine which confirmed the chemical constituents of both, MFCNC and ZnO in the hybrid (Wu, Li, Qin 2013). Comparing the FTIR spectra with those of MFCNC (Figure 4.3, curve c) that shows typical peaks at 814 cm^{-1} and 1565 cm^{-1} arising from the 1,3,5-triazine ring in the melamine structure, C-H bending vibration of the methylene group at 1330 cm^{-1}, and characteristic bands at 1020 cm^{-1} assigned to the $-CH_2-OH$ ether linkage of the melamine-formaldehyde resin (Wu, Li, Qin 2013). The absence of the ZnO stretching vibration at 430 cm^{-1} from the pure MFCNC curve indicated the formation of the ZnO crystal in curve b, Figure 4.3.

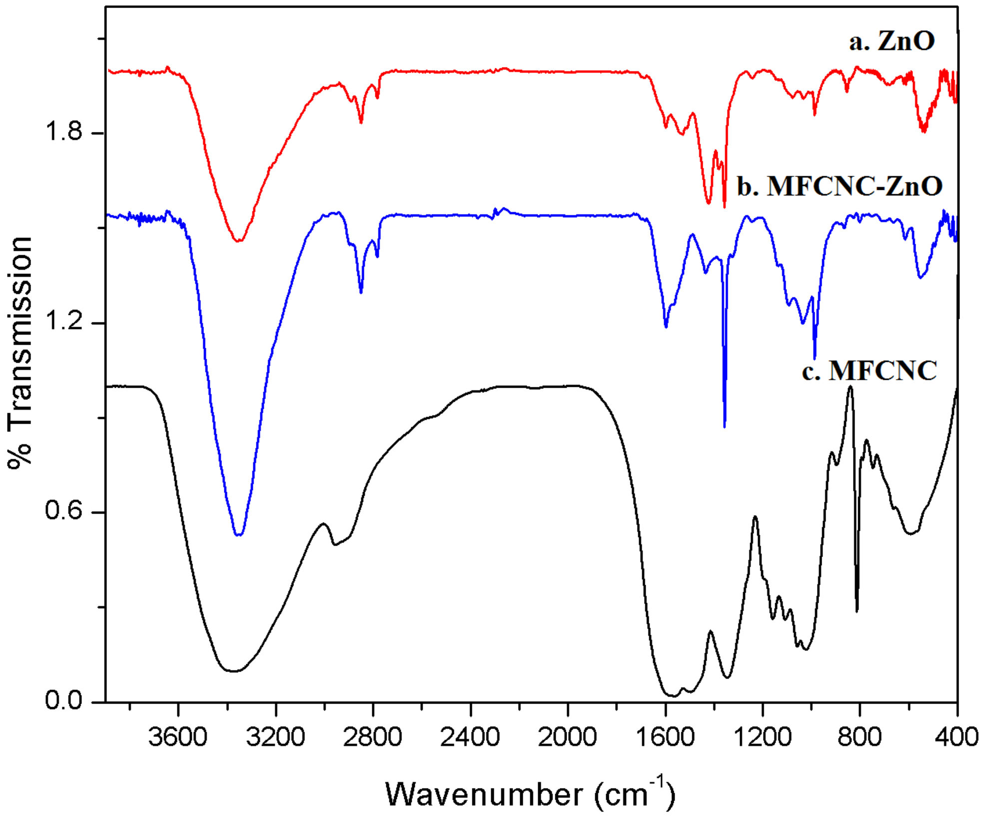

Figure 4.3: A. FTIR spectra of ZnO, ZNO@MFCNC and MFCNC measured between 4000-400 cm^{-1}.

4.4.3 Mass loading of ZnO determined from TGA analysis

Further support of the mass loading of active ZnO on the surface of MFCNC was determined from the thermogram. Based on the weight loss profiles of the three TGA curves (illustrated in Figure 4.4), the residual amounts of ZnO, ZnO@MFCNC and MFCNC determined at 700 ^{o}C were 96.42, 86.73 and 9.54%, respectively. From the analysis, the content of ZnO was calculated to be 88.85%, according to Equation (4.2).

$$\mathbf{C_{MFCNC} + C_{ZnO} = 1} \qquad \mathbf{(4.2)}$$

$$0.0954_{MFCNC} + 0.9642_{ZnO} = 0.8673$$

where C_{MFCNC} and C_{ZnO} mass ratio of MFCNC and ZnO, respectively. The degradation rate at 350 °C in the hybrid and MFCNC curve is mainly due to the size and surface area of the melamine-formaldehyde (MF) coated on CNCs (Wu et al. 2016) No net weight loss was observed in the TGA curve of pure ZnO, confirming the thermal stability of ZnO (Yu et al. 2015).

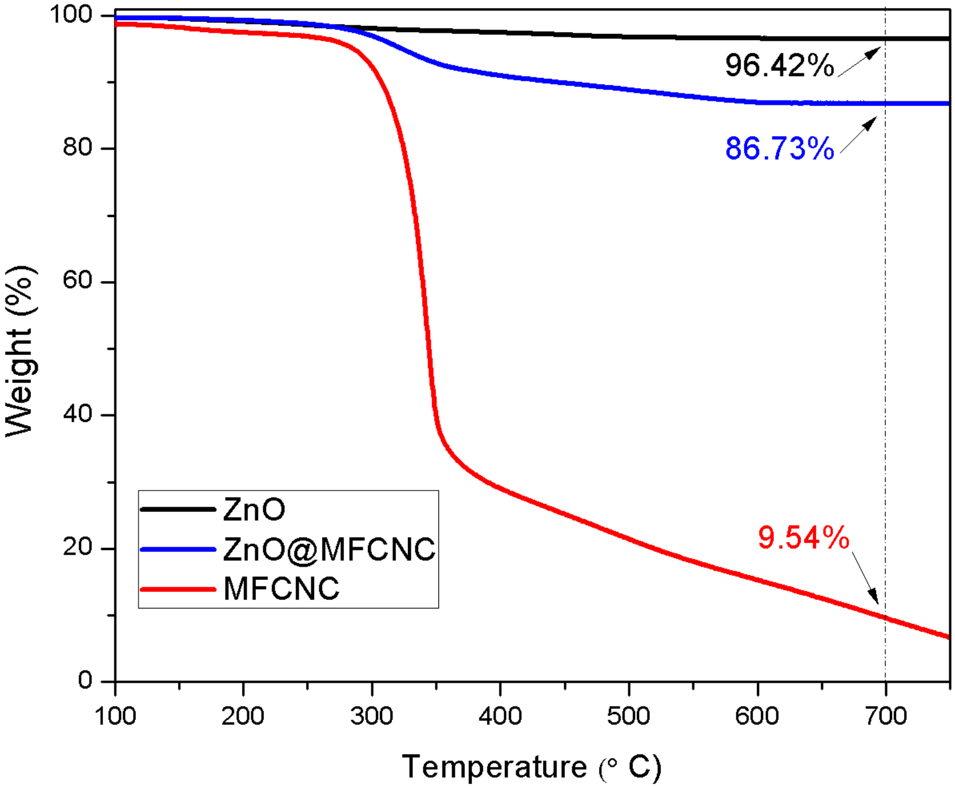

Figure 4.4: TGA measurements of ZnO, ZnO@MFCNC and MFCNC obtained at a heating rate of 20 °C/min under air.

4.4.4 Zeta potential measurements of hybrid ZnO@MFCNC

Furthermore, the stability of the nanoparticles was determined from the zeta potential measurements of ZnO@MFCNC complex and the metal oxide aqueous solution as a function of pH. This method is ideal to evaluate the colloidal stability of the suspension, measured through the surface charge of the nanoparticles. Especially for the targeted sunscreen application, it is important to have a solution that is demonstrably stable, and appropriate for the acidic surface of the skin (pH below 5) (Lambers et al. 2006). Research studies indicate that a pH of less than 5 is a desirable condition to maintain the biophysical parameters and resident skin microflora on the epidermal surface (Lambers et al. 2006). Upon evaluation of the curves, a strong pH dependency was observed for both systems. It is interesting to note that the ZnO@MFCNC hybrid yields a strong positive charge (+35mV) in acidic conditions due to protonation of the secondary amine group present on the melamine structure that exposes a positive charge detectable from the nitrogen atom, and identifies the stability of the colloids in solution. Similar positive surface charge was detected in the pure MFCNC solution, which further supports this explanation. The plot of the black line in Figure 4.5, is indicative of ZnO NPs displaying surface charge behavior typically attributed to the neutral hydroxyl groups attached to the surface of the metal oxide. At low pH, a weak positive charge (below +15mV) was detected due to transfer of some protons (H^+) from the environment to the surface of $Zn(OH)_2$ (Rasmussen et al. 2010).

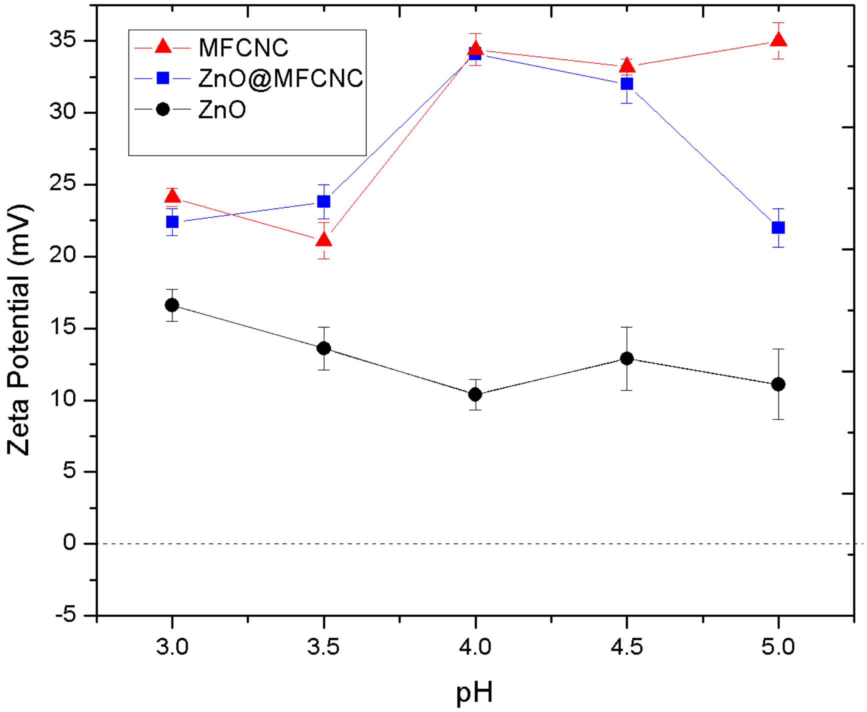

Figure 4.5: Zeta potential measurements of the three systems in aqueous solutions as a function of pH in acidic conditions.

4.4.5 Optical and UV absorbance

The formation of the ZnO crystal on the surface of MFCNC was validated through the presence of the characteristic UV absorption at 350nm from ZnO, in addition to the peak at 209 nm due to the triazine ring of melamine formaldehyde (Bône et al. 2011). The excited electronic states of semiconductor zinc oxide nanoparticles with a direct band gap energy of 3.31 eV differ to a great degree from the bulk ZnO, resulting in a quantum confinement effect of ZnO nanoparticles (Goh et al. 2014; Brus 1984). With the widening of the band gap energy, there is a decrease in the nanoparticle size which is evidenced by an overall blue shift in the spectrum (Brus 1984). From the optical measurements of the ZnO@MFCNC hybrid structure there was a visible blue shift detected in the wavelength from the bulk ZnO at 365 nm to ZnO@MFCNC at 350 nm, as illustrated in the inset of Figure 4.6. The blue shift is a good indication of the relative decrease in the particle size in comparison to pure ZnO, suggesting the importance of a chelating template provided by the porous MFCNC in controlling the nanoparticle formation in aqueous solution.

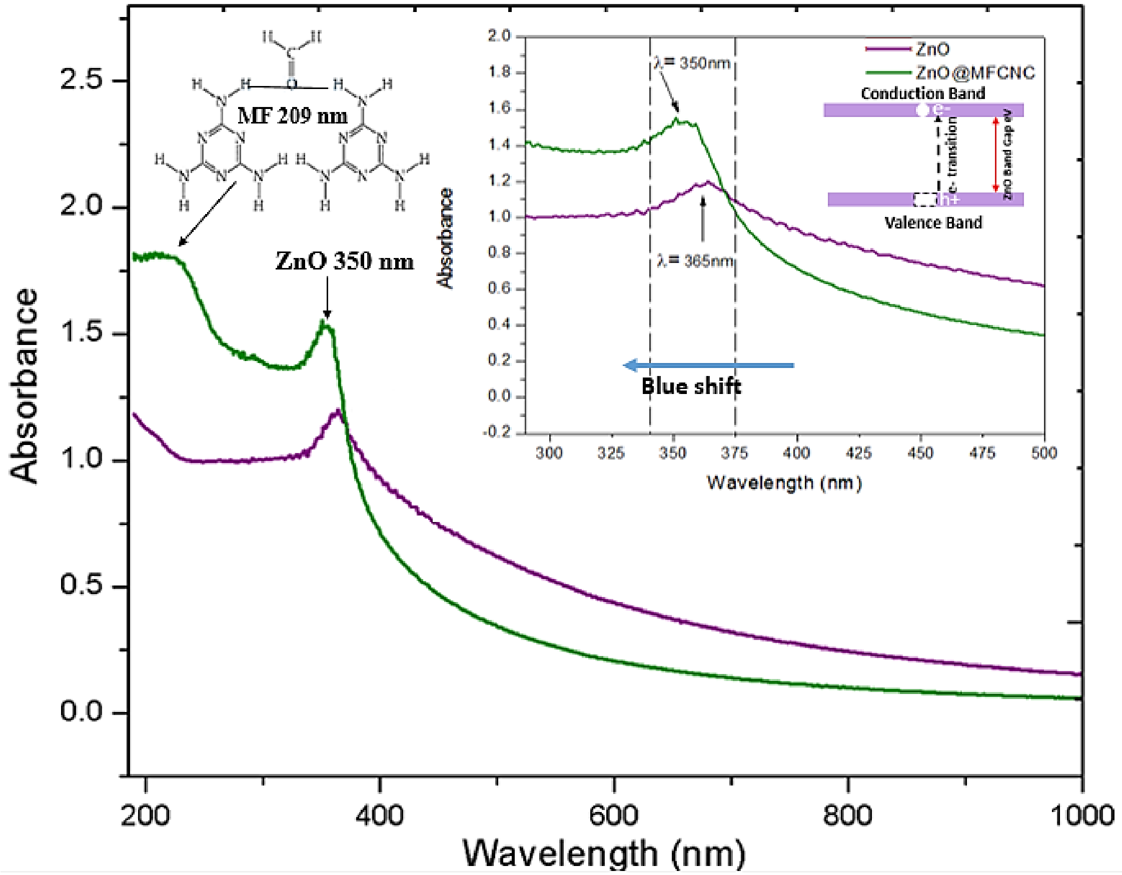

Figure 4.6: UV-Vis absorbance profile of ZnO@MFCNC nanocomposite and unmodified pure ZnO.

4.4.6 Transmission electron microscopy (TEM) analysis

The morphology of the hybrid system and formation of the ZnO nanoparticles was characterized through TEM. Figure 4.7A, and 4.7B show the contrast of an increase in the diameter and slight darkening of CNCs confirming the coating of melamine-formaldehyde on the rods, as observed previously (Wu et al. 2015; Wu et al. 2016). The morphology of the hybrid structure of ZnO@MFCNC displayed interesting structural arrangement, where the ZnO nanoparticles anchored on the surface of MFCNC showed a novel leaf-like growth on the rods in a branching fashion, as shown in the inset of Figure 4.7C. While the size of the MFCNCs remained intact, the average diameter of ZnO NPs on the surface ranged from 40-60 nm. In contrast, the ZnO particles synthesized without the additional template provided by MFCNC possessed micron sized clusters of particles > 200 nm, primarily due to the high interface energy of nanoparticles that lead to formation of aggregates in solution (Huang et al. 2013).

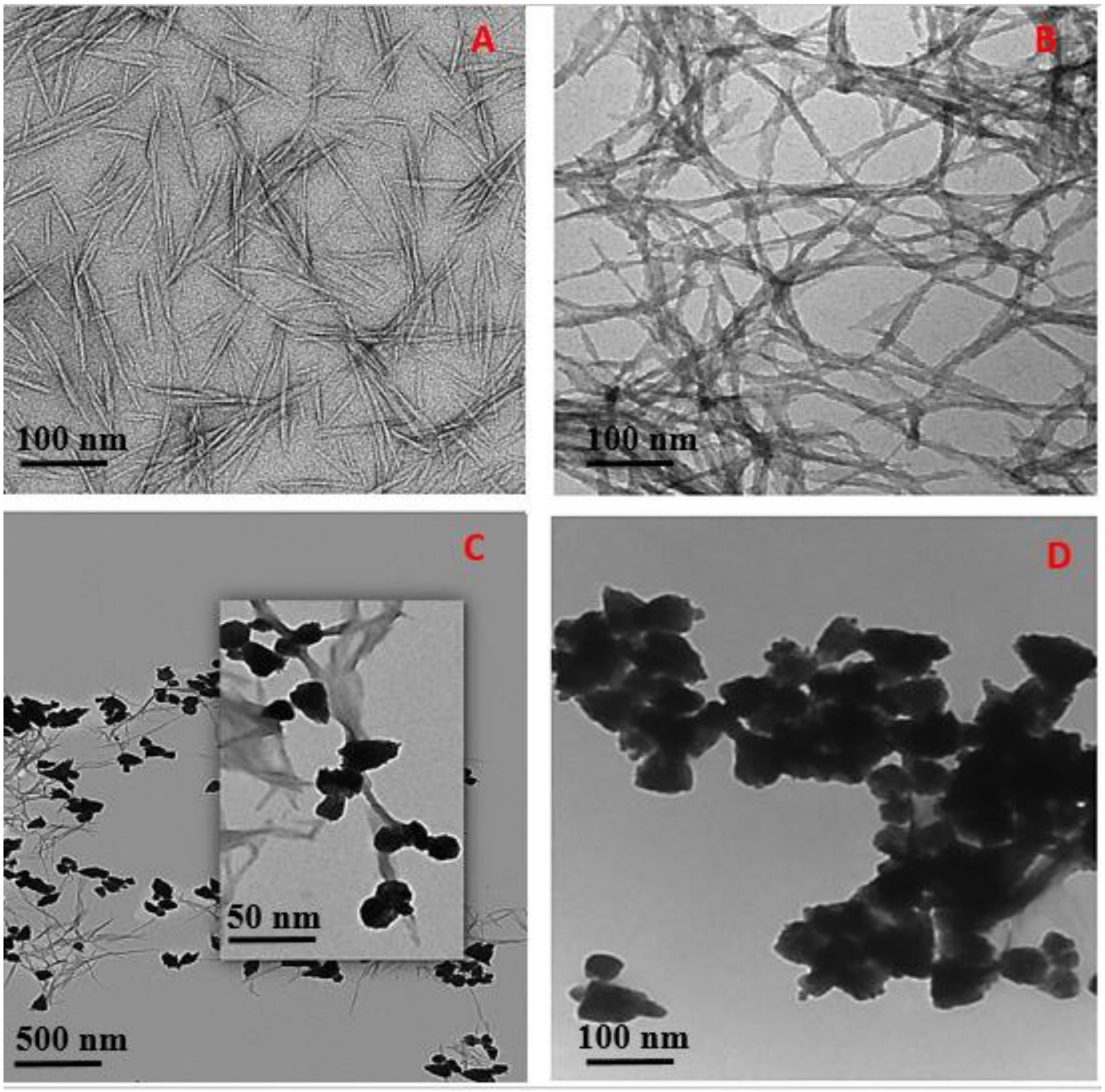

Figure 4.7: TEM micrographs of A. pristine CNCs; B. Melamine Formaldehyde (MF) coated CNCs; C. leaf-like growth of ZnO NPs on the surface of MFCNCs; and D. Pure ZnO particles > 100 nm.

4.4.7 SPF measurements

The efficacy of a sunscreen is a quantitative measurement of the Sun protection Factor (SPF) which is defined as a numerical rating system to indicate the degree of protection provided by a sunscreen product. This is based on the ratio of the least amount of UV energy (UVB) required to produce minimal erythema on sunscreen-protected skin over the amount of energy required to produce the same erythema on unprotected skin (Dutra et al. 2004; Dlugos 2011). At closer look, we know that the solar spectrum is composed of UVA (320-400nm) and UVB (290-320nm) radiation, where UVA is primarily involved in penetrating the epidermal and dermal layers of the skin that damage the keratinocytes, known to cause skin cancer. Although the effects of UVA sound dramatic, the risk of UVB exposure is approximately 1000x more erythemogenic compared to UVA, which could cause severe photo damage and sunburns due to the shorter UVB wavelength (Dutra et al. 2004). As such the SPF is primarily a measure of protection against UVB. Here the photo-protection of the hybrid structure and pure ZnO aqueous solutions was determined based on an in-vitro spectroscopic method for calculating the Sun Protection Factor values based on the well-developed Mansur mathematical Equation (4.3) (Mansur, Breder, Mansur, Azulay 1986):

$$SPF = CFx \sum_{290\,nm}^{320\,nm} EE(\Lambda)xI(\Lambda)xAbs(\Lambda) \tag{4.3}$$

where CF is the correction factor (10), EE (λ) is erythemogenic effect and solar radiation intensity at wavelength (Λ) I, and Abs (λ) is UV spectrophotometric absorbance values at wavelength λ determined at every 5 nm increments. The values of EE x I are normalized constants determined by Sayre *et al*.(Sayre et al. 1979) as shown in Table 4.1.

Table 4.1: Normalized EExI values corresponding to wavelength (nm) for calculating the SPF factor (Sayre et al. 1979).

Wavelength (nm)	EE x I
290	0.0105
295	0.0817
300	0.2874
305	0.3278
310	0.1864
315	0.0839
320	0.0180

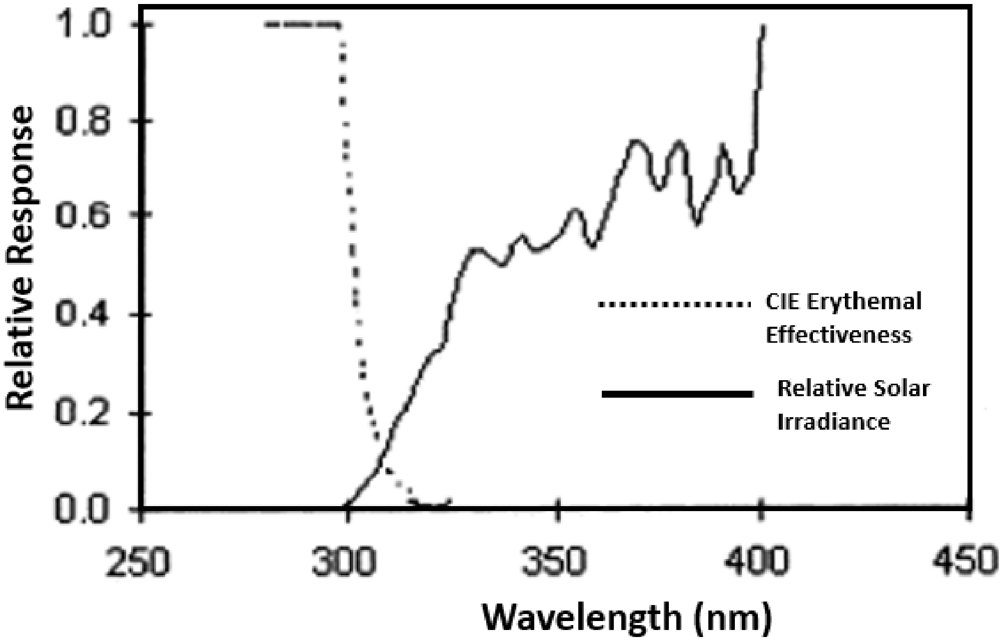

Figure 4.8: Solar and erythema spectra of the standardized function EE(ʎ) and I(ʎ) (Adopted from Springsteen et al. 1999).

4.4.8 Effect of hydroxide concentration on SPF

By systematically varying the ratio of MFCNC-Zn^{2+} to hydroxide, an optimal composition of 1[Zn^{2+}]:[OH^-]3 was achieved. It is suggested that this optimal ratio for the measurement of SPF is directly related to the particle size and morphology, where the reduction in particle size, from micro to nano, directly affects the sun protection factor. From our observations, it clear that with increasing hydroxide ratio from 3 to 10, the reaction between the zinc ion and hydroxide proceeded very fast resulting in fast growth of the ZnO particles. This affects the solution stability due to increased particle size (micrometers) and a loss in the specific active surface area, in contrast to the optimal ratio of 1:3. By further increasing the hydroxide ratio greater than 10, it was found that there was no ZnO crystal formed as confirmed by an absence of the characteristic exciton energy peak of ZnO at 350 nm wavelength, in addition to a loss of cloudy precipitate due to a decrease in the zinc concentration (Conde et al. 2011). The result shows that significant changes in the alkaline ratio controlled the ZnO particle formation after the initial nucleation on the MFCNC substrate.

4.4.8.1 Comparison profile of ZnO@MFCNC and micro ZnO

Figure 4.9 shows the comparative SPF values of the as synthesized ZnO@MFCNC hybrid solutions and pure ZnO solutions of varying hydroxide ratios. The results from the experimental studies showed the deposition of ZnO on the surface of MFCNC susbtrate that outperfromed the pure ZnO solutions in almost all of the [OH] ratios tested, with the maximum SPF value of 14 (std. 0.35) obtained at a ratio of (MFCNC): 1[Zn^{2+}]: 3[OH]. The role of the porous MFCNC matrix becomes obvious from these results as it provides; (i) increased surface area due to the sponge-like porous matrix, (ii) offers chelation of the zinc ion (Zn^{2+}) with enhanced affinity through the rich nitrogen groups of the MF resin (Baraka, A.; Hall, P. J.; Heslop 2007; Filik 1997), (iii) from here the confined growth of the metal oxide in the mesopores of the MF resin leads to controlled nanoparticle size which offers better UV absorption in comparison to pure micro ZnO.

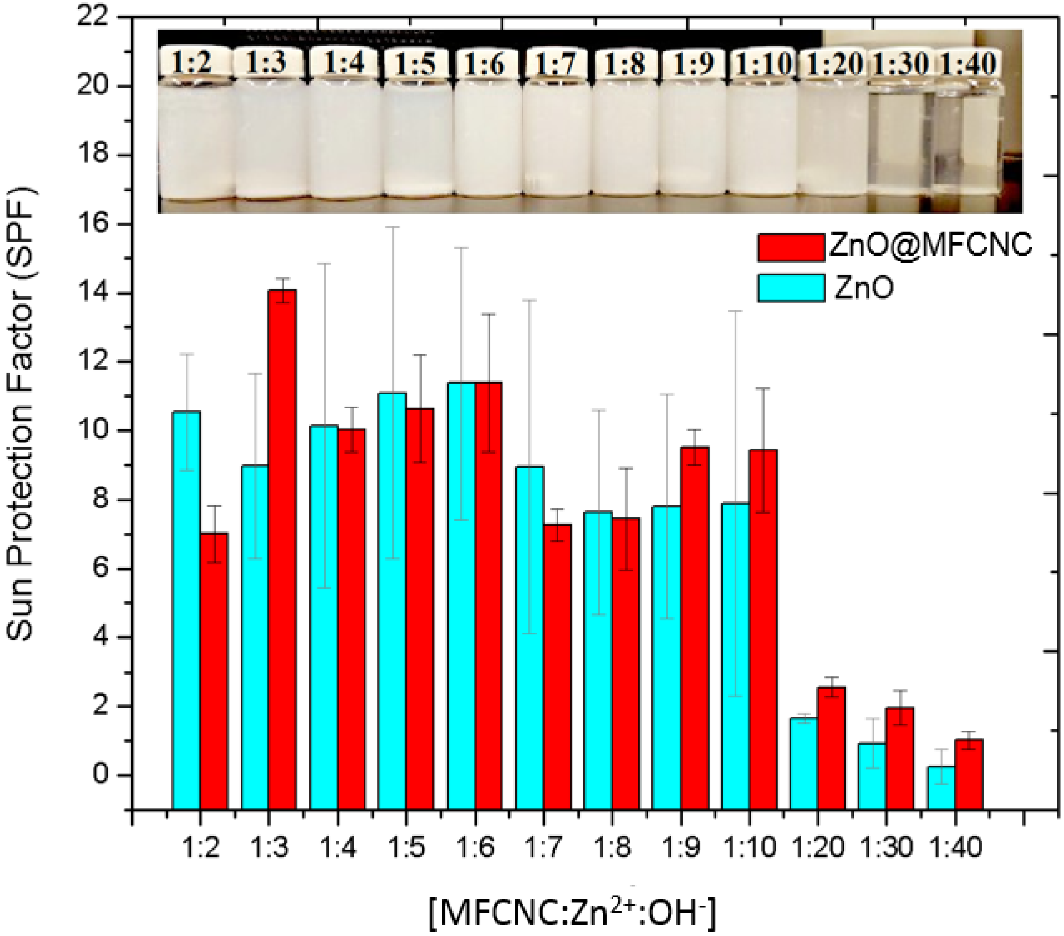

Figure 4.9: Bar graph illustrating the comparative SPF values of aqueous ZnO@MFCNC and pure ZnO solutions, with increasing [OH] ratios.

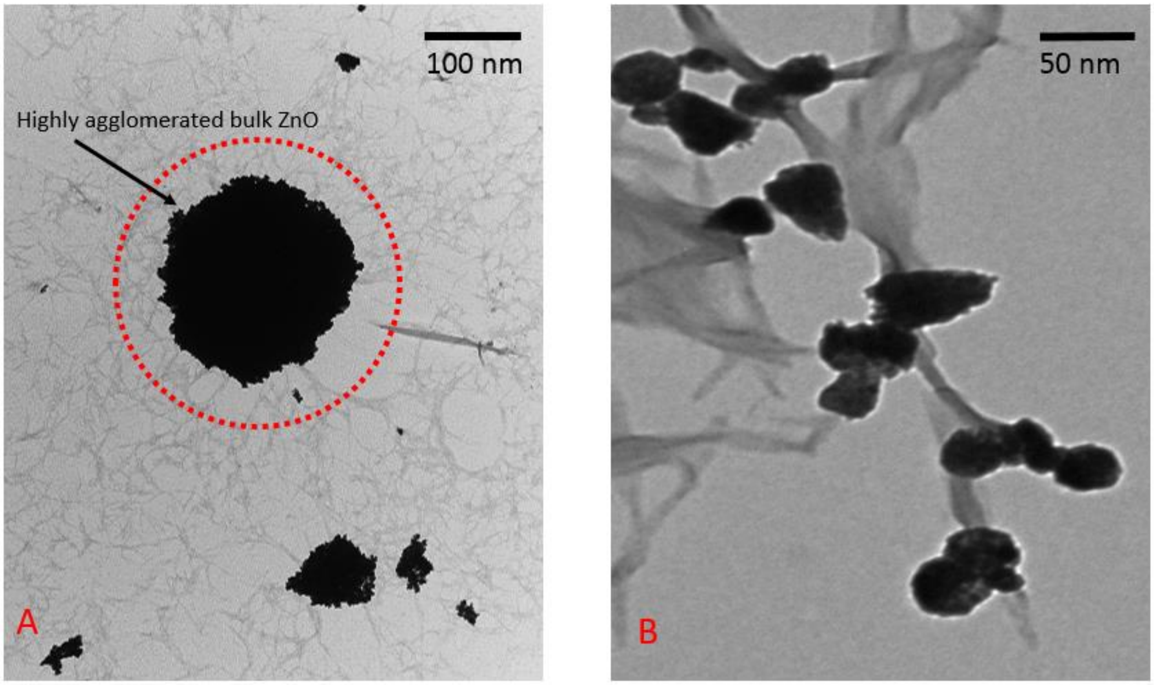

Figure 4.10: A. ZnO bulk formation on pristine CNC. B. MF coated CNC with controlled leaf-life growth of ZnO NPs on the surface of the rods.

The effect of the nitrogen functionality provided by the MF coating on CNC for the controlled growth of ZnO NPs is shown in Figure 4.10. Without the additional mesoporous N-rich surface of MF, the ZnO formed large agglomerates, which inevitably affects the cosmetic performance.

4.4.9 Evaluation of photocatalysis of surface-active CNC

4.4.9.1 Langmuir-Hinshelwood model

The rate of degradation of methylene blue (MB) can be easily computed through colorimetric measurements (Figure 4.11A and 4.11B) that provides a means to assess the photocatalytic performance of the CNC based system, both qualitatively and quantitatively. Our study revealed profound results and differentiation of the ZnO@MFCNC system, in contrast to bulk ZnO. The pseudo-first order linear kinetic rate plot shown in Figure 4.11C was derived from the Langmuir-Hinshelwood model (4.4)

$$-\ln\left(\frac{C_t}{C_o}\right) = kt \tag{4.4}$$

where C_t is the concentration at irradiation time (t), C_o is the initial concentration at irradiation time 0, and k is the first order rate constant. Liner regressions of the data presented in Figure 4.11C revealed a 4-fold increase in the kinetic rate of the ZnO@MFCNC system (0.0117 min^{-1}) in comparison to ZnO (0.00314 min^{-1}), and an even faster rate of 0.0387 min^{-1} was observed for the study under sunlight of the CNC supported hybrid. The hybrid structure showed complete degradation after 60 mins under solar stimulation, and 96.49% degradation after 200 mins under artificial UV light, as illustrated in Figure 4.11D, whereas, bulk ZnO showed only half the degradation (51.14%) at 200 mins, with complete degradation observed after 6 hours.

The kinetics under sunlight for the CNC supported hybrid system indicated a 2-stage reaction, with a slow first stage of 0.0248 min^{-1} followed by a faster rate of 0.0593 min^{-1}, and complete degradation observed after 60 mins, as shown in Figure 4.12. The faster kinetics and the two stages can be primarily attributed to the source of sunlight, with both the UV and visible incorporated activation of the CNC supported catalyst. The different speed of the kinetics of the two stages can be defined by the UV+Visible (sunlight intensity) over the 60 min interval, where in the first stage the light hits and slowly activates the surface of the catalyst, followed by deeper and faster penetration of the porous CNC network and ZnO catalyst. The results point to evidence for the hybrid system to actively utilize both the UV, as well as the visible region for photocatalytic degradation, making it advantageous for practical outdoor applications. These results can be further described through the molecular activity at the atomic level, followed by series of photocatalytic redox reactions at the surface of the semiconductor ZnO@MFCNC, as discussed in the following section.

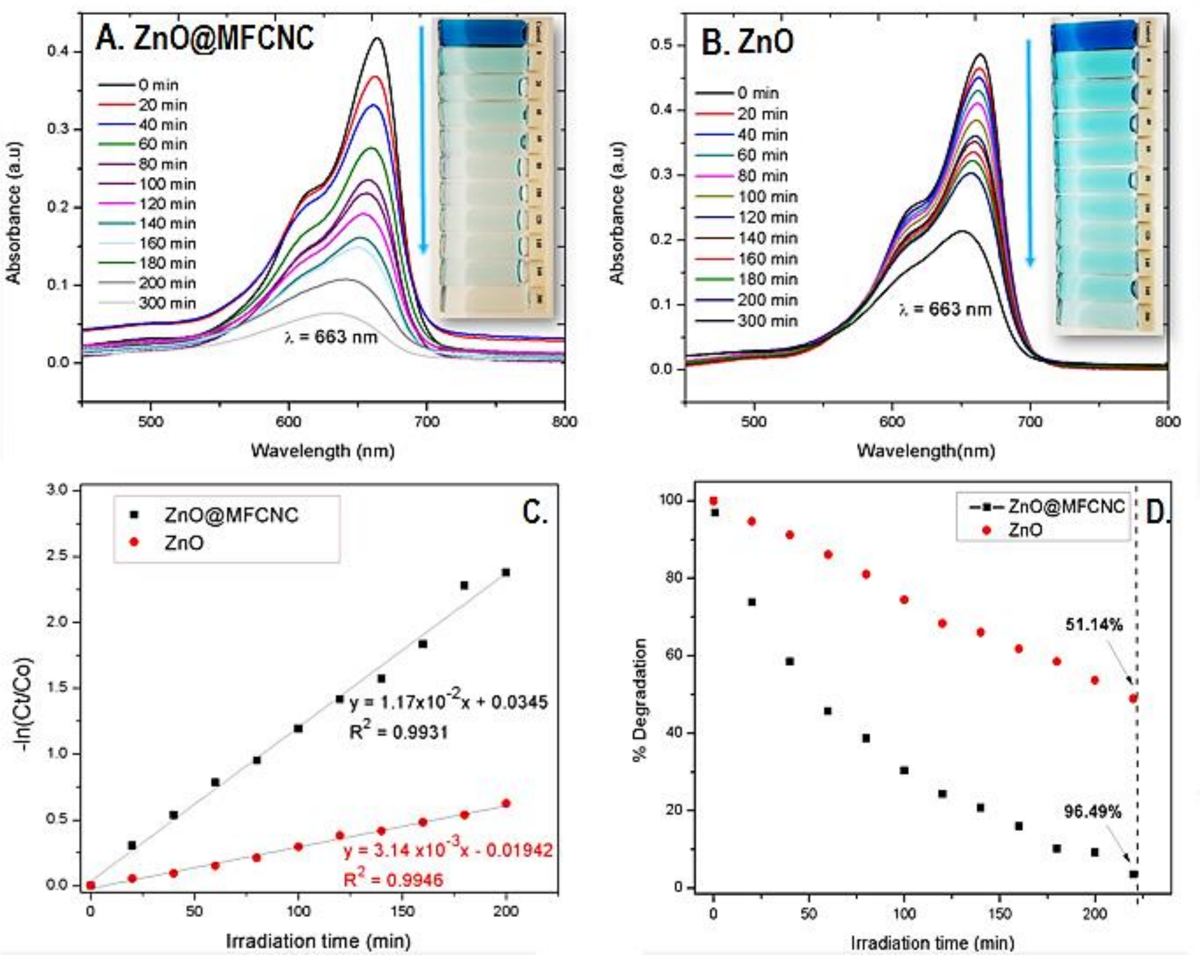

Figure 4.11: A. UV-vis attenuation profile and absorption spectra of methylene blue (MB) photocatalytic degradation by ZnO@MFCNC; B. Absorption spectra of the photocatalytic degradation of MB by pristine ZnO; C. Pseudo-first order kinetic rate plot of ZnO and ZnO@MFCNC under UV; D. Photocatalytic % degradation of ZnO and ZnO@MFCNC under UV as a function of the irradiation time (min).

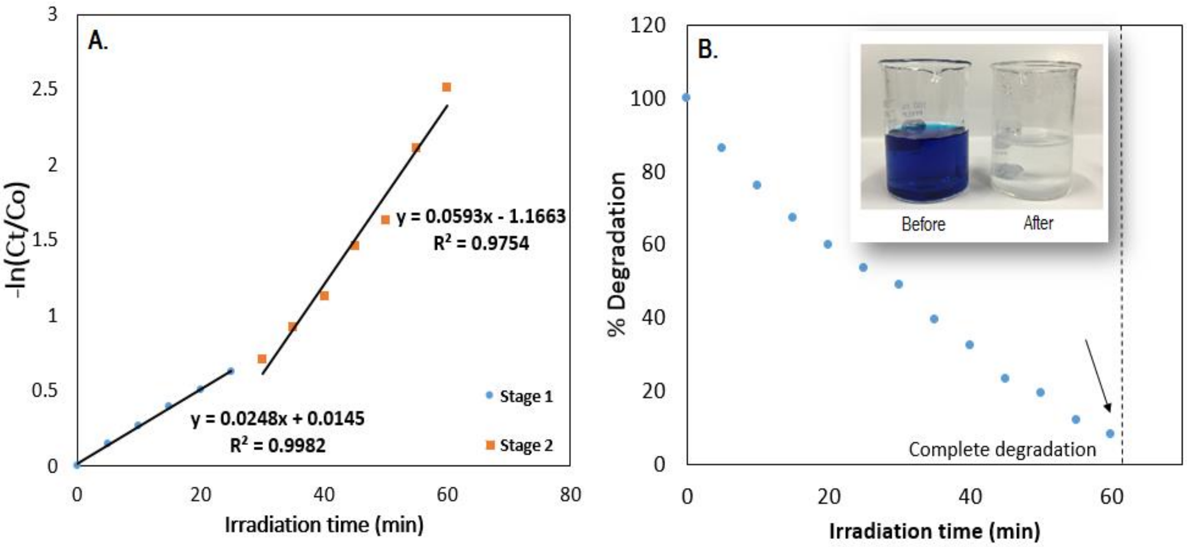

Figure 4.12: Sunlight induced photocatalytic degradation of hybrid ZnO@MFCNC. A. 2-stage linear regressions of ZnO@MFCNC under sunlight. B. Degradation profile of ZnO@MFCNC hybrid under sunlight as function of time (min).

4.4.9.2 Solid band-gap theory of semiconductor metal oxides

The emphasis of the optical absorption in colloidal semiconductors is interestingly dissimilar from bulk materials (Nogueira & Jardim 1993; Sun et al. 2014). The electronic conduction in a solid can be explained through the Molecular Orbital (MO) theory where the molecular orbitals are treated as energy bands instead of discrete levels due to the small difference in energy (Nogueira & Jardim 1993; Brus 1984). As in the case of the solid semiconductor ZnO@MFCNC, electrons occupy the energy bands according to their energy. Upon UV excitation, the electrons in the highest occupied orbital of the valence band (VB) are promoted to the unoccupied orbital of the conduction band (CB) above it; leaving behind hole (positive charge) in the valence band (Nogueira & Jardim 1993). The space between these energy bands is the band gap which acts as a barrier to electronic mobility. The systematic e^-/h^+ formation dictates the photocatalytic mechanism when e^-/h^+ pairs migrate to the semiconductor surface and participate in a redox reaction with the adsorbed organic compounds (i.e. methylene blue) (Dao et al. 2016; Guo et al. 2011; Sun et al. 2011; Etacheri et al. 2012). This migration rate increases when there is a widening of the band gap with a reduction in the particle size, which allows e^- or h^+ to react with surface-adsorbed species before recombination, thus, improving the catalytic efficiency (Huang et al. 2013; Sanna et al. 2016). Here, the role of the templated effect of the mesoporous MFCNC becomes important, as it confines the growth of the ZnO NPs which (1) controls the NP growth, (2) increases the specific surface area of the semiconductor ZnO, (3) effectively prevents e^-/h^+ recombination and promotes photo-induced charge carriers to the surface of the catalyst which has major implications for the photocatalytic performance of the structure. A schematic illustration of the mechanism, with explanation of the redox reactions is described in Figure 4.13.

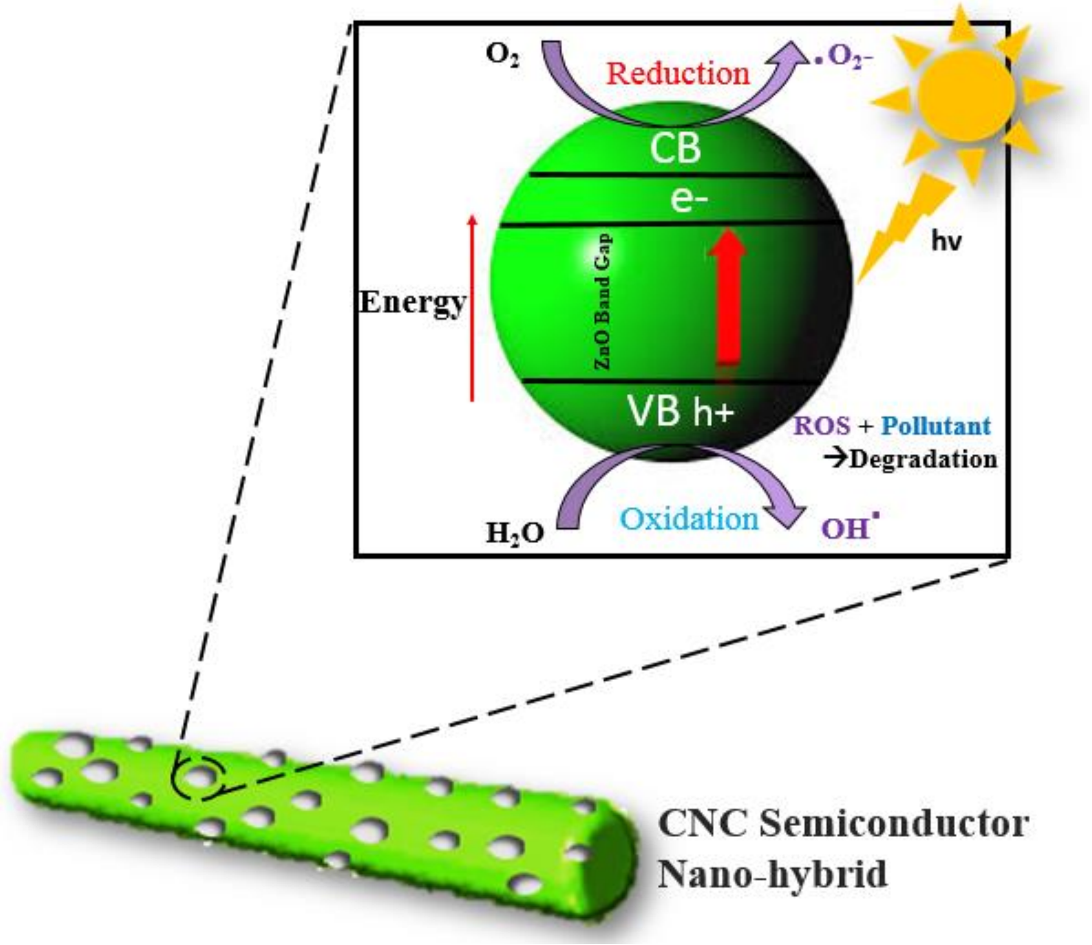

Figure 4.13: Schematic representation of semiconductor ZnO grown on the surface of MFCNC.

Upon UV excitation with energy exceeding the band gap, electrons (e^-) are promoted from ground state to the conduction band, resulting in vacancy (h^+) in the valence band. The systematic e^-/h^+ formation dictates the photocatalytic activity of the semiconductor hybrid. The photogenerated h^+ oxidize H_2O molecules adsorbed on the surface of ZnO to OH· radicals. In the upper band, the excited e^- of CB react with pre-adsorbed O_2 molecules to form reactive oxygen species (ROS) (i.e. superoxide anion radical $\cdot O_2^-$ (Huang et al. 2015). Given the high quantum yield of photogenerated holes, the actual degradation of the dye can arise from direct transfer of photogenerated carriers or through the formation of ROS (Guo et al. 2011), which complete the reaction by degrading any organic pollutants in primary contact.

To briefly conclude this chapter, an optimized nitrogen-enriched polymer coated CNC network provided for leaf-like growth of semiconductor ZnO. The hybrid structure showed high in-vitro SPF values and a large increase in the photocatalytic performance as result of reduced crystallite size of the ZnO catalyst, and confined surface energy in aqueous system. Much of the significance and detailed conclusions from this research will be discussed in the subsequent chapter.

Chapter 5

Engineering significance and arterial contributions

5.1 Significance and conclusions for the work presented in chapter 3

A comparison of the antioxidant performance defined by stage 1 (k_1) rate constant and stage 2 (k_2) rate constant for other C60 derivatives described in literature, suggests the comparable results and scope of the CNC-based antioxidant system. Our work on the $C_{60}(OH)_{30}$-CNC system utilizing the high surface area of cellulose nanocrystals for the nucleation of $C_{60}(OH)_{30}$ displayed superior antioxidant performance with $k_1 = 6.7x10^{-3}$ min^{-1}, $k_2 = 2.0x10^{-3}$ min^{-1}, which is much higher than the stages of other previously reported studies. The high activity of $C_{60}(OH)_{30}$-CNC is largely attributed to the monodispersed fine-sized $C_{60}(OH)_{30}$ nanoparticles that are uniformly deposited on the surface of cellulose nanocrystals. The synthesis of $C_{60}(OH)_{30}$ NPs on CNCs is advantageous in the following ways; (i) the high surface area and hydrophilicity of the cellulose nanocrystals leads to the development of an aqueous based, biocompatible nanohybrid, (ii) it is advantageous over unmodified fullerenes that are hydrophobic and rigid, thus hindering their usage in an aqueous biological system, (iii) the excited surface of CNC substrate captures the electron on the C=C of $C_{60}(OH)_{30}$ that enhances the immobilization of $C_{60}(OH)_{30}$ NPs and controls the particle growth, (iv) the presence of high negative surface charge of the sulfate ester groups on CNCs imparts additional colloidal stability to the conjugated fullerol nanoparticles.

Table 5.1: Comparison of the antioxidant performance of various C_{60} solubilized systems with DPPH as the model radical.

C60 Solibilization/Derivatives	**Model Radical**	**Rate Constant k_1 (min^{-1})**	**Rate Constant k_2 (min^{-1})**	**Reference**
PDMA-C60	DPPH	$5.2x10^{-3}$	$1.1x10^{-3}$	(Tam et al. 2013)
NCC-BCD-C60	DPPH	$1.7x10^{-3}$	Not determined	(Yao & Tam 2014)
PEO-b-PAA-C60	DPPH	$0.9x10^{-3}$	$0.5x10^{-3}$	(Yao & Tam 2014)
Lactose-C60 complex	DPPH	$1.0x10^{-3}$	Not determined	(Bhoi et al. 2012)
Surface modified CNC-$C_{60}(OH)_{30}$	**DPPH**	**$6.7x10^{-3}$**	**$2.0x10^{-3}$**	**Present Work**

Decorating polyhydroxylated C_{60} on the surface of CNC yields well-distributed and colloidally stable $C_{60}(OH)_{30}$ nanoparticles with excellent anti-oxidant characteristics. TGA and FTIR analysis showed characteristic $C_{60}(OH)_{30}$ peaks in the fullerol-CNC spectra, which provided evidence for the successful conjugation of fullerols on CNC. The large negative charge on the surface of CNC enables a stable dispersion of fullerol nanoparticles in aqueous solution. As a result of the reduced tendency to form clusters and the greater accessibility to the free radicals DPPH, $C_{60}(OH)_{30}$-CNC demonstrated faster and improved antioxidant performance. The observed 2-stage pseudo-first order kinetics suggested that at the molecular level, the radical scavenging behaviour involves the interaction of DPPH with the H-atom from the surface –OH groups on C_{60}, followed by the reaction with the π-conjugated nucleus. The findings from this study summarize the development of biocompatible scavenging system for the therapeutic suppression of free radicals, paving way for the design of an optimal system for antioxidant personal care applications.

5.2 Significance of the work presented in chapter 4

An effective demonstration of a sustainable novel strategy for the growth of semiconductor ZnO on surface modified porous cellulose nanocrystals in aqueous solution was developed. The study encompassed the evaluation and characterization of the surface active ZnO@MFCNC nanohybrid as an ultraviolet filter and photocatalytic agent. The material demonstrated a high UV absorption profile with an SPF value of 14 based on 5% active ingredient, and a 4-fold increase in photocatalysis under UV and solar radiation, suggesting the possibility for scale up.

Table 5.2 shows a comparison of the kinetics for the photocatalytic performance of other ZnO based systems for the degradation of organic pollutants. Our synthesized hybrid material demonstrates comparable rate constants for irradiation under UV and ameliorated values for the solar radiated samples. This suggests the viability and capacity of the system to efficiently degrade organic pollutants, due to a chelating porous template such as MFCNC for semiconductor fabrication.

Table 5.2: Comparison of the Photocatalytic Performance of ZnO based system for degradation of organic pollutants.

ZnO based Photocatalytic Systems	Model Pollutant	Rate Constant (min^{-1}) UV	Rate Constant (min^{-1}) Sunlight	Reference
Fe_3^+ doped ZnO calcined @400 °C	2-CP	not studied	0.0263	(Ba-Abbad et al. 2013)
Mn_3O_4- doped ZnO	4-CP	not studied	0.0133	(Qamar et al. 2016)
TiO_2/ZnOchitosan complex	MO	not studied	0.0256	(Zhu et al. 2012)
Au-ZnO hetrostructures	MB	0.021	0.0350	(Adhikari et al. 2016)
ZnO chelated on mesoporous MFCNC matrix	**MB**	**0.0117**	**0.0593K_2/0.0248K_1**	**present work**

Investigation of the ZnO@MFCNC hybrid system shows that structural defects and band gap tailoring are not the only means to enhance the photocatalytic activity of ZnO, but can also be engineered through the control of size, geometry and orientation of the semiconductor by means of a porous template that; (1) confines the surface energy and growth of ZnO NPs, (2) promotes interfacial e^- charge transfer to the surface of the catalyst through entrapment of the photo-induced charge carriers in the pores of the MFCNC rod and preventing e^-/h^+ recombination. By synergizing the functionality of the N-rich mesoporous MFCNC with semiconductor ZnO, a platform for nanostructure fabrication has been developed, which may find large scale application as multifunctional cosmetics.

5.3 Contributions to the development of functionalized CNC in cosmetic systems

The enclosed work presented in this thesis, describes the development of nature derived, functional cosmetic systems. The work generated from a preparatory building block, such as cellulose nanocrystals (CNC) has been shown to lay the foundation for the development and enhancement of cosmetic systems. A schematic summary of the work is summarized in Figure 5.1.

- In the first application, a new approach to solubilize the rigid and hydrophobic C_{60} fullerene molecules was established using CNC as a template, and stabilizer. The functional system rendered advanced antioxidant properties that offer an advantage over currently commercialized C_{60} fullerene developed by Bio Research Corporation, in Japan, which has is shown to form aggregates in aqueous solution (Benn et al., 2013). By rendering completely water soluble $C_{60}(OH)_{30}$ molecules conjugated to the surface of CNC, we eliminate the formation of aggregates; an imperative factor for water dispersibility, anti-oxidant activity and the understanding of radical scavenging mechanism at the molecular level. Geometrically speaking, these well-distributed $C_{60}(OH)_{30}$ on CNC offer optimized functionality for antioxidant performance, in addition to making the hybrid structure safe, biocompatible and a nontoxic candidate for practical application.

- Next, a systematic method for preparing surface-active ZnO deposited on CNC was established, and evaluated for its UV protection, and photocatalytic performance under natural and UV light. This work offers an aqueous based multifunctional cosmetic system that can eliminate the need for toxic chemical coatings and additional processing steps to create emulsions for commercial ZnO nanoparticles. The system operates in a unique two-dimensional capacity, where it can effectively block UV rays, and simultaneously convert the solar energy to break down environmental pollution coming in contact with the skin. From a more fundamental approach, this study satisfies a significant criteria to achieve highly active semiconductor ZnO with good photocatalytic properties, but without the atypical band gap tailoring mediated by dopants on the surface of the crystal.

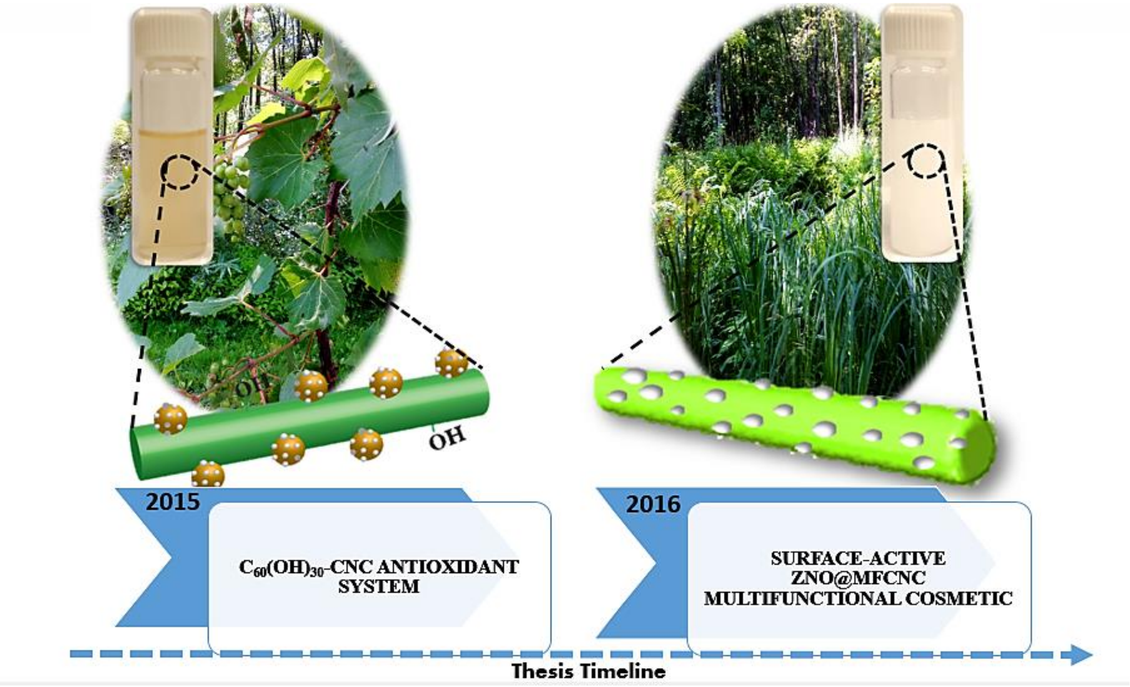

Figure 5.1: Summary of the development of surface modified CNCs for optimized personal care systems.

Chapter 6

Recommendations

The work reported in this thesis describes the development, characterization and application of CNC based cosmetic systems, which can be translated into innovative commercial enterprises. To provide for a path towards such an avenue, the following recommendations for future possibilities are disclosed herein.

6.1 Recommendations for the work presented in chapter 3

The fundamental system consisting of polyhydroxylated C_{60} fullerene nucleated on the surface of CNC, presented in chapter 3, can be formulated as a light-weight cream or spray for anti-aging products with active antioxidant capacity. Further in-vitro studies for dermal penetration on skin models is recommended to demonstrate the systems practical usage in skin care products. The nanohybrid $C_{60}(OH)_{30}$-CNC can also be extended to applications in biomedical fields, where, fullerols $C_{60}(OH)_x$ have been shown to be applicable particularly for cancer chemotherapy (Chaudhuri et al. 2009). With the advantage of a fully functional, and controlled fullerol nanoparticle on CNC, the size-tuning properties can be central to higher drug-loading transfer to tumor sites. Such a hybrid system can also be applied in an anti-HIV system by penetrating the hydrophobic cavity of HIV proteases, inhibiting the access of substrates to the catalytic site of the enzyme. In addition, electron transfer from excited state of fullerene and DNA bases, can be used for DNA cleavage and other genome engineering disciplines.

6.2 Recommendations for the work presented in chapter 4

The strategy for synthesizing ZnO@MFCNC hybrid structure can be implemented in a range of commercial avenues that ascribe to a sustainable process that reduces the carbon footprint of toxic chemicals. The highly porous CNC hybrid can be added to a cosmetic or therapeutic composition for external use to reduce and prevent the onset of premature aging of skin, and fatigued skin caused by oxidative stress from environmental pollutants and UV rays. These surface-active cellulose nanocrystals offer an easy synthetic and scalable process that meets the demand of homogeneous production on a large scale for commercial application.

The platform created in chapter 4 can be strategically extended to deposit and grow other metal oxides, such as TiO_2, CeO_2 on the mesoporous substrate. Since CNCs offer consistent physiochemical and mechanical properties, they can be directed as a model to study and compare various metal oxide systems and its effect on band-gap and semiconductor properties. The function of the photocatalytic capacitance, and sun protection efficacy comes from surface reactivity of the semiconductor crystals, and the morphology of the nanoparticles, respectively. It will be necessary to study the impact of such theoretical oxide systems operating on the CNC supported carrier, for applications in waste water treatment, optoelectronics or biomedical capacities.

References

Adhikari, S., Gupta, R., Surin, A., Kumar, T.S., Chakraborty, S., Sarkar, D. & Madras, G. 2016. Visible light assisted improved photocatalytic activity of combustion synthesized spongy-ZnO towards dye degradation and bacterial inactivation. *RSC Adv.*, 6(83), pp.80086–80098.

Akhlaghi, S.P., Berry, R.C. & Tam, K.C. 2013. Surface modification of cellulose nanocrystal with chitosan oligosaccharide for drug delivery applications. *Cellulose*, 20(4), pp.1747–1764.

Andersson, T., Nilsson, K., Sundahl, M., Westman, G. & Wennerstrom, O. 1992. C_{60} embedded in γ-cyclodextrin: a water-soluble fullerene. *J. Chem. Soc., Chem. Commun.*, 8, pp.604–606.

Assemi, S., Tadjiki, S., Donose, B.C., Nguyen, A.V. & Miller, J.D. 2010. Aggregation of fullerol C60(OH)24 nanoparticles as revealed using flow field-flow fractionation and atomic force microscopy. *Langmuir*, 26(20), pp.16063–16070.

Atwood, J.L., Koutsantonis, G. a. & Raston, C.L. 1994. Purification of C60 and C70 by selective complexation with calixarenes. *Nature*, 368, pp.229–231.

Ba-Abbad, M.M., Kadhum, A.A., Mohamad, A.B., Takriff, M.S. & Sopian, K. 2013. Visible light photocatalytic activity of Fe3+-doped ZnO nanoparticle prepared via sol-gel technique. *Chemosphere*, 91(11), pp.1604–1611.

Baraka, A., Hall, P. J. & Heslop, M.J. 2007. Melamine-formaldehyde-NTA chelating gel resin: Synthesis, characterization and application for copper(II) ion removal from synthetic wastewater.. *React. Funct. Polym*, 67(7), pp.585–600.

Becheri, A., Durr, M., Nostro, P.L. & Baglioni, P. 2008. Synthesis and characterization of zinc oxide nanoparticles: Application to textiles as UV-absorbers. *Journal of Nanoparticle Research*, 10(4), pp.679–689.

Benn, Troy., Westerhoff, P. & Herckes, P. 2013. Detection of fullerenes (C60 and C70) in commercial cosmetics. *Evironmental Pollution*, 159(5), pp.1334–1342.

Bhoi, V.I., Kumar, S. & Murthy, C.N. 2012. The self-assembly and aqueous solubilization of [60]fullerene with disaccharides. *Carbohydrate Research*, 359, pp.120–127.

Bica, C.D., Borsali, R., Geissler, E. & Rochas, C. 2001. Dynamics of cellulose whiskers in agarose gels. 1. Polarized dynamic lightscattering. *Macromolecules*, 35(15), pp.5275–5279.

Bône, S., Vautrin, C., Barbesant, V., Truchon, S., Harrison, I. & Geffroy, C. 2011. Microencapsulated fragrances in melamine formaldehyde resins. *Chimia*, 65(3), pp.177–181.

Bosi, S., Da Ros, T., Spalluto, G., & Prato, M. 2003. Fullerene derivatives: An attractive tool for biological applications. *European Journal of Medicinal Chemistry*, 38(11-12), pp.913–923.

Bourlinos, A.B., Georgakilasc, V., Bakandritsosd, A., Kouloumpise, A., Gournise, D. & Zboril, R. 2012. Aqueous-dispersible fullerol-carbon nanotube hybrids. *Materials Letters*, 82, pp.48–50.

Bowman, D.M. & Calster, G. Van. 2008. Flawless or Fallible? A Review of the Applicability of the European Union's Cosmetics Directive in Relation to Nano-Cosmetics. *Studies in Ethics Law and Technology*, 2(3), pp. 1-35.

Brand-Willliams, Cuvelier, M.E. & Berset, C. 1995. Use of a Free Radical Method to Evaluate Antioxidant Activity. *Lebensm.-Wiss. u.-Technol.*, 28, pp. 25–30.

Brant, J., Labille,J., Robichaud, C.O. & Wiesner, M. 2007. Fullerol cluster formation in aqueous solutions: Implications for environmental release. *Journal of Colloid and Interface Science*, 314(1), pp.281–288.

Brus, L.E., 1984. Electron–electron and electron-hole interactions in small semiconductor crystallites: The size dependence of the lowest excited electronic state. *The Journal of Chemical Physics*, 80(9), p.4403.

Cao, L., White, J.S., Park, J.S., Schuller, J.A., Clemens, B.M. & Brongersma, M.L. 2009. Engineering light absorption in semiconductor nanowire devices. *Nature Materials*, 8(8), pp.643–647.

Chaudhuri, P., Paraskar, A., Soni, S., Mashelkar, R.A., Sengupta, S. 2009. Fullerenol-cytotoxic conjugates for cancer chemotherapy. *ACS Nano*, 3(9), pp.2505–2514.

Chen, K.L. & Elimelech, M. 2009. Relating colloidal stability of fullerene (C60) nanoparticles to nanoparticle charge and electrokinetic properties. *Environmental Science and Technology*, 43(19), pp.7270–7276.

Chen, L., Lai, C., Marchewka, R., Berry, R.M. Tam, K.C. 2016. CdS quantum dot-functionalized cellulose nanocrystal films for anti-counterfeiting applications. *Nanoscale*, pp.13288–13296.

Cheng, C., Amini, A., Zhu, C., Xu, Z., Song, H. Wang, N. 2014. Enhanced photocatalytic performance of TiO2-ZnO hybrid nanostructures. *Scientific reports*, 4, p.4181-4186.

Chiang, L.Y., Upasani, R.V., Swirczewski, J.W. & Soled, S. 1993. Evidence of hemiketals incorporated in the structure of fullerols derived from aqueous acid chemistry. *Journal of the American Chemical Society*, 115(13), pp.5453–5457.

Chiang, L.Y., Lu, F.J. & Lin, J.T. 1995. Free radical scavenging activity of water-soluble fullerenols. *Journal of the Chemical Society, Chemical Communications*, (12), p.1283-1284.

Conde, M.N., Dakshi, K., Zouihri, H. & Jaber, B. 2011. Preparation of ZnO Nanoparticles without Any Annealing and Ripening Treatment. *Journal of Materials Science and Engineering*, 1, pp.985–990.

Dao, D.V., Bremt, M., Koeller, Z. & Le, T.K. 2016. Effect of metal ion doping on the optical properties and the deactivation of photocatalytic activity of ZnO nanopowder for application in sunscreens. *Powder Technology*, 288, pp.366–370.

Deguchi, S., Alargova, R.G. & Tsujii, K. 2001. Stable Dispersions of Fullerenes, C 60 and C 70 , in Water. Preparation and Characterization. *Langmuir*, 17(19), pp.6013–6017.

Dietl, T., 2010. A ten-year perspective on dilute magnetic semiconductors and oxides. *Nature Materials*, 9(12), pp.965–974.

Djordjevic, A. & Bogdanovic, G. 2008. Fullerenol: A new nanopharmaceutic? *Archive of oncology*, 16(3-4), pp.42–45.

Dlugos, J.F., 2011. In Vitro Method for the Calculation of Sunscreen SPF Values. *Case study 009963B_01, PerkinElmer, Inc*, p.4.

Dutra, E.A., Oliveira, D.A., KedorHackmann, E.R. & Santoro, M.R. 2004. Determination of sun protection factor (SPF) of sunscreens by ultraviolet spectrophotometry. *Revista Brasileira de Ciências Farmacêuticas,* 40(3), pp.381–385.

Friends of the Earth. 2006. Nanomaterials, sunscreens and cosmetics: Small ingredients, big risks. *Melbourne: Friends of the Earth Australian and US*. http://emergingtech.foe.org.au/nanomaterials-sunscreens-and-cosmetics-small-ingredients-big-risks/

Etacheri, V., Roshan, R. & Kumar, V. 2012. Mg-doped ZnO nanoparticles for efficient sunlight-driven photocatalysis. *ACS Applied Materials and Interfaces*, 4(5), pp.2717–2725.

Filik, H., Oztürk, B.D.,Doğutan, M., Gümüş, G. & Apak, R. 1997. Separation and preconcentration of iron(II) and iron(III) from natural water on a melamine-formaldehyde resin. *Talanta*, 44(5), pp.877–884.

Fu, F., Li, L., Liu, L., Cai, J., Zhang ,Y., Zhou, J. & Zhang, L. 2015. Construction of cellulose based ZnO nanocomposite films with antibacterial properties through one-step coagulation. *ACS Applied Materials and Interfaces,* 7(4), pp.2597–2606.

Geckeler, K.E. & Samal, S. 2001. Rapid Assessment of the Free Radical Scavenging Property of Fullerenes. *Fullerene Science and Technology*, 9(1), pp.17–23.

Giacalone, F. & Martin, N. 2006. Fullerene polymers: Synthesis and properties. *Chemical Reviews*, 106(12), pp.5136–5190.

Goh, E.G., Xu, X. & McCormick, P.G. 2014. Effect of particle size on the UV absorbance of zinc oxide nanoparticles. *Scripta Materialia*, 78-79, pp.49–52.

Goswami, T.H., Singh, R., Alam, S., & Mathur, G. N. 2004. Thermal analysis: A unique method to estimate the number of substituents in fullerene derivatives. *Thermochimica Acta*, 419(1-2), pp.97–104.

Guo, M.Y., Ng, A., Liu, F., Djurisic, A.B., Chan, W.K., Su, H. & Wong, K.M. 2011. Effect of native defects on photocatalytic properties of ZnO. *Journal of Physical Chemistry C*, 115(22), pp.11095–11101.

Habibi, Y., A. L. Goffin, N. Schiltz, E. Duquesne, P. Dubois, and A.D. Dufresne. 2008. Bionanocomposites based on poly (ε-caprolactone)-grafted cellulose nanocrystals by ring-opening polymerization. *Journal of Materials Chemistry*, pp.5002–5010.

Habibi, Y., 2014. Key advances in the chemical modification of nanocelluloses. *Chem. Soc. Rev.*, 43(5), pp.1519–1542.

Habibi, Y., Chanzy, H. & Vignon, M.R. 2006. TEMPO-mediated surface oxidation of cellulose whiskers. *Cellulose*, 13(6), pp.679–687.

Habibi, Y., Lucia, L. a & Rojas, O.J. 2010. Cellulose Nanocrystals : Chemistry , Self-Assembly , and Applications. *Chemical reviews*, 110, pp.3479–3500.

Hewa-Kasakarage, N.N., El-Khoury, P.Z., Tarnovsky, A.N., Kirsanova, M., Nemitz, I., Nemchinov, A., Zamkov, M. 2010. Ultrafast carrier dynamics in type II ZnSe/CdS/ZnSe nanobarbells. *ACS Nano*, 4(4), pp.1837–1844.

Hildebrandt, N., Spillmann, C.M., Algar, W.R., Pons, T., Stewart, M.H., Oh, E., Susumu, K., Diaz, S.A.,Delehanty, J.B. & Medintz, I.L. 2016. Energy Transfer with Semiconductor Quantum Dot Bioconjugates: A Versatile Platform for Biosensing, Energy Harvesting, and Other Developing Applications. *Chemical reviews*, DOI: 10.1021/acs.chemrev.6b00030

Huang, C., Wang, Y. & Luo, G. 2013. Preparation of highly dispersed and small-sized ZnO nanoparticles in a membrane dispersion microreactor and their photocatalytic degradation. *Industrial and Engineering Chemistry Research*, 52(16), pp.5683–5690.

Huang, N., Shu, J., Wang, Z., Chen, M., Ren, C. & Zhang, W. 2015. One-step pyrolytic synthesis of ZnO nanorods with enhanced photocatalytic activity and high photostability under visible light and UV light irradiation. *Journal of Alloys and Compounds*, 648, pp.919–929.

Jackson, J.K., Letchford, K., Wasserman, B.Z., Ye, L., Hamad, W.Y. & Burt, H.M. 2011. The use of nanocrystalline cellulose for the binding and controlled release of drugs. *International journal of nanomedicine,* 6, pp.321–330.

Jimenez-Gonzaez, A.E, Urueta, J, A. and Suarez-Parra, R. 1998. Optical and electrical characteristics of aluminum-doped ZnO thin films prepared by sol gel technique. *Journal of Crystal Growth,* 192, pp.430–438.

Joo, J., Chow, B.Y., Prakash, M., Boyden, E.S., Jacobson, J.M .2011. Face-selective electrostatic control of hydrothermal zinc oxide nanowire synthesis. *Nature materials,* 10(8), pp.596–601.

Kalia, S., Dufresne, A., Cherian, B.M., Kaith, B.S., Averous, L., Njuguna, J. & Nassiopoulos, E. 2011. Cellulose-based bio- and nanocomposites: A review. *International Journal of Polymer Science*, 2011, pp. 1-35.

Kato, S., Aoshima, H., Saitoh, Y. & Miwa, N. 2009. Highly hydroxylated or γ-cyclodextrin-bicapped water-soluble derivative of fullerene: The antioxidant ability assessed by electron spin resonance method and β-carotene bleaching assay. *Bioorganic and Medicinal Chemistry Letters*, 19(18), pp.5293–5296.

Kelly, J.A., Giese, M., Shopsowitz, K.E., Hamad, W.Y., MacLachlan, M.J. 2014. The development of chiral nematic mesoporous materials. *Accounts of Chemical Research*, 47(4), pp.1088–1096.

Khan, A., Khan, R.A,. Salmieri, S., Le Tien, C., Riedl, B., Bouchard, J., Chauve, G., Tan, V., Kamal, M.R & Lacroix, M. 2012. Mechanical and barrier properties of nanocrystalline cellulose reinforced chitosan based nanocomposite films. *Carbohydrate Polymers*, 90(4), pp.1601–1608.

Kokubo, K., Shirakawa, S., Kobayashi, N., Aoshima, H. & Oshima, T. 2011. Facile and scalable synthesis of a highly hydroxylated water-soluble fullerenol as a single nanoparticle. *Nano Research*, 4(2), pp.204–215.

Kołodziejczak-Radzimska, A. & Jesionowski, T. 2014. Zinc Oxide—From Synthesis to Application: A Review. *Materials*, 7(4), pp.2833–2881.

Kumar, A., Negi. Y.S., Choudhary, V. & Bhardwaj, N.K. 2014. Characterization of Cellulose Nanocrystals Produced by Acid-Hydrolysis from Sugarcane Bagasse as Agro-Waste. *Journal of Material Physics and chemistry*, 2, pp.1–8.

Kumar, S., Massie, C. & Dumonceaux, M.D. 2006. Comparative innovative business strategies of major players in cosmetic industry. *Industrial Management & Data Systems*, 106(3), pp.285–306.

Lambers, H., Piessens, S., Bloem, A., Pronk, H. & Finkel, P. 2006. Natural skin surface pH is on average below 5, which is beneficial for its resident flora. *International Journal of Cosmetic Science*, 28(5), pp.359–370.

Li, J., Takeuchi, A., Ozawa, M., Li, X., Saigo, K. & Kitazawa, K. 1993. C60 fullerol formation catalysed by quaternary ammonium hydroxides. *Journal of the Chemical Society, Chemical Communications*, (23), p.1784.

Li, Y., Wang, H., Xie, L., Liang, Y., Hong, G. & Dai, H. 2011. MoS2 nanoparticles grown on graphene: An advanced catalyst for the hydrogen evolution reaction. *Journal of the American Chemical Society*, 133(19), pp.7296–7299.

Liao, D.L., Badour, C. a. & Liao, B.Q. 2008. Preparation of nanosized TiO2/ZnO composite catalyst and its photocatalytic activity for degradation of methyl orange. *Journal of Photochemistry and Photobiology A: Chemistry*, 194, pp.11–19.

Lin, N., Bruzzese, C. & Dufresne, A. 2012. TEMPO-oxidized nanocellulose participating as crosslinking aid for alginate-based sponges. *ACS Applied Materials and Interfaces*, 4(9), pp.4948–4959.

Lin, N., Huang, J. & Dufresne, A. 2012. Preparation, properties and applications of polysaccharide nanocrystals in advanced functional nanomaterials: a review. *Nanoscale*, 4(11), p.3274.

Liu, K., Nasrallah, J, Chen, L., Huang, L. & Ni, Y. 2015. Preparation of CNC-dispersed Fe3O4 nanoparticles and their application in conductive paper. *Carbohydrate Polymers*, 126, pp.175–178.

Mansur, J. S., Breder, M. N., Mansur, M. C. A. & Azulay, R.D. 1986. Determination of Sun Protection Factor by Spectrophotometry. *An. Bras. Dermatol., Rio de Janeiro*, 61, pp.121–124.

Matsubayashi, K., Goto, T., Togaya, K., Kokubo, K. & Oshima, T. 2008. Effects of pin-up oxygen on [60]fullerene for enhanced antioxidant activity. *Nanoscale Research Letters*, 3(7), pp.237–241.

Meulenkamp, E. 1998. Synthesis and Growth of ZnO Nanoparticles. *Journal of Physical Chemistry B*, 5647(98), pp.5566–5572.

Moon, R.J., Martini, A., Nairn, J., Simonsen, J. & Youngblood, J. 2011. Cellulose nanomaterials review: structure, properties and nanocomposites, Chem. Soc. Rev.40, pp. 3941-3994.

Mumalo-Djokic, D., Stern, W.B. & Taubert, A. 2008. Zinc oxide/carbohydrate hybrid materials via mineralization of starch and cellulose in the strongly hydrated ionic liquid tetrabutylammonium hydroxide. *Crystal Growth and Design*, 8(1), pp.330–335.

Nishiyama, Y., Johnson, G.P., French, A.D., Forsyth, V.T. & Langan P. 2008. Neutron crystallography, molecular dynamics, and quantum mechanics studies of the nature of hydrogen bonding in cellulose Ibeta. *Biomacromolecules*, 9, pp.3133–3140.

Nogueira, R.F.P. & Jardim, W.F. 1993. Photodegradation of Methylene-Blue - Using Solar Light and Semiconductor (Tio2). *Journal of Chemical Education*, 70(10), pp.861–862.

P.B. Taunk, R. Das, D.P. Bisen, R.K.T. 2015. Structural characterization and photoluminescence properties of zinc oxide nano particles synthesized by chemical route method. *Journal of Radiation Research and Applied Sciences*, 8, pp.433–438.

Payen, A. 1883. M´emoire sur la composition du tissu propre des plantes et du ligneux. *Comptes Rendus*, 7, pp.1052–1056.

Peng, B.L., Dhar, N., Liu, H.L., Tam, K.C. 2011. Chemistry and applications of nanocrystalline cellulose and its derivatives: A nanotechnology perspective. *Canadian Journal of Chemical Engineering*, 89(5), pp.1191–1206.

Qamar, M.T., Aslam, M., Rehan, Z.A., Soomro, M.T., Basahi, J.M., Ismali, I.M., Almeelbi, T. & Hameed, A. 2016. The influence of p-type Mn3O4 nanostructures on the photocatalytic activity of ZnO for the removal of bromo and chlorophenol in natural sunlight exposure. *Applied Catalysis B: Environmental*.201, pp. 105-118.

Rasmussen, J.W., Martinez, E., Louka, P. & Wingett, D.G. 2010. Zinc oxide nanoparticles for selective destruction of tumor cells and potential for drug delivery applications. *Expert Opinion on Drug Delivery*, 7(9), pp.1063–1077.

Sam Adam-Day, 2016. Carbohydrate Polymers. Available at: https://alevelnotes.com/Carbohydrate-polymers/65.

Sanna, V., Pala, N., Alzari, V., Nuvoli, D. & Carcelli, M. 2016. ZnO nanoparticles with high degradation efficiency of organic dyes under sunlight irradiation. *Materials Letters*, 162, pp.257–260.

Sayre, R.M., Agin, P.P., LeVee, G.J. & Marlowe, E. 1979. A comparison of in vivo and in vitro testing of sunscreening formulas. *Photochemistry and photobiology*, 29(3), pp.559–566.

Shopsowitz, KE, Qi, H., Hamad, W.Y. & MacLachlan, M.J. 2010. Free-standing mesoporous silica films with tunable chiral nematic structures. *Nature*, 468, pp.422–425.

Singla, M.L., Shafeeq M, M. & Kumar, M. 2009. Optical characterization of ZnO nanoparticles capped with various surfactants. *Journal of Luminescence*, 129(5), pp.434–438.

Siqueira, G., Bras, J. & Dufresne, A. 2010. Cellulosic bionanocomposites: A review of preparation, properties and applications. *Polymers*, 2(4), pp.728–765.

Springsteen, A., Yurek, R., Frazier, M., & Carr, K.F. 1999. In vitro measurement of sun protection factor of sunscreens by diffuse transmittance. *Analytica Chimica Acta*, 380(2-3), pp.155–164.

Sun, J.H. Dong, S,Y., Feng, J.L., Yin, X.J., & Zhao, X.C. 2011. Enhanced sunlight photocatalytic performance of Sn-doped ZnO for Methylene Blue degradation. *Journal of Molecular Catalysis A: Chemical*, 335(1-2), pp.145–150.

Sun, Z., Liao, T., Dou ,Y., Hwang, S.M., Park, M.S., Jiang, L., Kim, J.H., & Dou, S.X. 2014. Generalized self-assembly of scalable two-dimensional transition metal oxide nanosheets.

Nature communications, 5(3813), pp. 1-9.

Tam, J., Liu, J. & Yao, Z. 2013. Effect of microstructure on the antioxidant properties of fullerene polymer solutions. *RSC Advances*, 3, pp.4622–4627.

Tingaut, P., Zimmermann, T., & Sèbe, G. 2012. Cellulose nanocrystals and microfibrillated cellulose as building blocks for the design of hierarchical functional materials. *Journal of Materials Chemistry*, 22**,** pp. 20105-20111.

Ueno, H., Yamakuru, S., Arastoo, A.S., Oshima,T., & Kokubo, K. 2014. Systematic Evaluation and Mechanistic Investigation of Antioxidant Activity of Fullerenols Using β-Carotene Bleaching Assay. *Journal of Nanomaterials*. 2014, pp. 1-7.

Wang, H. & Roman, M. 2011. Formation and properties of chitosan− cellulose nanocrystal polyelectrolyte− macroion complexes for drug delivery applications. *Biomacromolecules*, 12(5), pp.1585–1593.

Wang, I.C., Tai, L.A., Lee, D.D., Kanakamma, P.P., Shen, C.K., Luh, T.Y., Cheng, C.H., & Hwang, K.C. 1999. C60 and water-soluble fullerene derivatives as antioxidants against radical-initiated lipid peroxidation. *Journal of Medicinal Chemistry*, 42(22), pp.4614–4620.

Williams. & Verhoeven, J.W. 1994. Interactions of Fullerenes and Calixarenes in the Solid State. *J. Am. Chem. Soc*. 16 (15), pp. 6965–6966.

Wu, X., Shi, Z., Tjandra, R., Cousins, A.J., Sy, S., Yu, A., Berry, R.M., & Tam, K.C. 2015. Nitrogen-enriched porous carbon nanorods templated by cellulose nanocrystals as high performance supercapacitor electrodes. *J. Mater. Chem. A*, 3, pp.23768-23777.

Wu, X., Shi, Z., Fu, S., Chen, J., Berry, R.M., & Tam, K.C. 2016. Strategy for Synthesizing Porous Cellulose Nanocrystal Supported Metal Nanocatalysts. 4(11), pp 5929–5935.

Xiang, Q., Yu, J. & Jaroniec, M. 2012. Synergetic Effect of MoS $_2$ and Graphene as Cocatalysts for Enhanced Photocatalytic H $_2$ Production Activity of TiO $_2$ Nanoparticles. *Journal of the American Chemical Society*, 134(15), pp.6575–6578.

Y. Wu, Y. Li, L. Qin, F.Y. and D.W. 2013. Freestanding flexible graphene foams @ Polypyrrole @MnO2 Electrodes for high-performance supercapacitors. *Journal of Materials Chemistry A*, 1, pp.204–212.

Yao, Z. & Tam, J. 2014. Fullerene-derived cellulose nanocrystal, their preparation and uses thereof.

United States. Publication No. 0256832 A1

Yin, M., Gu, Y., Kuskovsky, I.L., Andelman, T., Zhu, Y., Neumark, G.F., O'Brien, S. 2004. Zinc oxide quantum rods. *Journal of the American Chemical Society*, 126(20), pp.6206–6207.

Yu, W., Xu, D. & Peng, T. 2015. Enhanced photocatalytic activity of g-C3N4 for selective CO2 reduction to CH3OH via facile coupling of ZnO: A direct Z-scheme mechanism. *J. Mater. Chem. A*, 3, pp.19936–19947.

Zhou, C., Wu, Q., Yue, Y. & Zhang, Q. 2011. Application of rod-shaped cellulose nanocrystals in polyacrylamide hydrogels. *J Colloid Interface Sci.*, 353, pp.116–123.

Zhu, H., Jiang, R., Fu, Y., Guan, Y., Yao, J., Xiao, L. & Zeng, G. 2012. Effective photocatalytic decolorization of methyl orange utilizing TiO 2/ZnO/chitosan nanocomposite films under simulated solar irradiation. *Desalination*, 286, pp.41–48.

Zoppe, J.O., Peresin, M.S., Habibi, Y., Venditti, R. & Rojas, O.J. 2009. Reinforcing poly(ε-caprolactone) nanofibers with cellulose nanocrystals. *ACS Applied Materials and Interfaces*, 1(9), pp.1996–2004.